Experimental Study of a High Efficiency Gyrotron Oscillator

by

Eunmi Choi

M.S. (Physics), POSTECH (2002)
B.S. (Physics), Ewha Womans University (2000)

Submitted to the Department of Physics
in partial fulfillment of the requirements for the degree of

Doctor of Philosophy

at the

MASSACHUSETTS INSTITUTE OF TECHNOLOGY

September 2007

Author .....
Department of Physics
August 14, 2007

Certified by .....
Richard J. Temkin
Senior Research Scientist, Department of Physics
Thesis Supervisor

Accepted by .....
Thomas J. Greytak
Professor and Associate Department Head for Education

Experimental Study of a High Efficiency Gyrotron Oscillator

by

Eunmi Choi

Submitted to the Department of Physics
on August 14, 2007, in partial fulfillment of the
requirements for the degree of
Doctor of Philosophy

Abstract

High power, high frequency gyrotrons used in plasma heating must achieve the highest possible efficiency in order to reduce system size and cost and to minimize thermal and mechanical problems. This thesis presents an experimental study of efficiency enhancement in a 1.5 MW, 110 GHz gyrotron oscillator, which operated at 50 % efficiency with a single-stage depressed collector. We present the design and detailed experimental results of a new low ohmic loss cavity, a four-mirror internal mode converter and a single-stage depressed collector. The low ohmic loss $TE_{22,6}$ cavity, designated "V-2005", was designed using the code MAGY to have a Q factor of 830, which would be suitable for CW operation in an industrial gyrotron. The cavity was first tested in the axial configuration, in which the output waveguide also serves as the electron beam collector. In 3 microsecond pulsed operation at 97 kV and 40 A, an output power of 1.67 MW at an efficiency of 42 % was obtained without a depressed collector. The V-2005 cavity efficiency exceeds that of the older "V-2003" cavity by 5 percentage points. The enhanced efficiency of the V-2005 cavity may be understood by analyzing the start-up scenario of the cavities. During start-up, the V-2003 cavity suffers from strong mode competition with the $TE_{19,7}$ mode, resulting in a relatively low efficiency, while the V-2005 cavity has an absence of such mode competition. The experimental mode maps (regions of oscillation vs. magnetic field) obtained for the two cavities are in excellent agreement with the start-up simulations. Following the axial configuration experiments, the experiment was rebuilt with an internal mode converter consisting of a launcher and 4 mirrors, and with a single-stage depressed collector. An output power of 1.5 MW was measured. The internal mode converter operated at 90 % efficiency. When the depressed collector was run at 25 kV, an overall efficiency of 50 % was achieved. An aftercavity interaction (ACI) was investigated as a possible cause of efficiency reduction in the gyrotron. The ACI occurs when the spent electron beam interacts at cyclotron resonance with the traveling output microwave beam in a region of lower magnetic field just after the cavity. The presence of the ACI was identified from the comparison between simulation results and the measurement of the depression voltage as a function of beam current. Future research should consider ways of eliminating the ACI, ways of improving the internal mode converter,

and the use of a two-stage depressed collector.

Thesis Supervisor: Richard J. Temkin
Title: Senior Research Scientist, Department of Physics

Acknowledgments

This thesis would not be possible without helps and insights from various people. I deeply would like to thank my advisor, Dr. Richard Temkin for his continuous support and guidance throughout last five years. His insight in physics gave me an inspiration which enabled me to break-through experimental huddles. I also thank Prof. John Belcher and Prof. Miklos Porkolab for reading my thesis. Prof. Porkolab also served as my academic advisor and oral committee member. Dr. Michael Shapiro helped me with numerous ways. His door was always open whenever I had questions and needed discussions. I learned a lot of parts of quasi-optical mode converters from him. Many thanks are also due to Dr. Jagadishwar Sirigiri who helped me greatly with experiments. I could start my experiments initially with great help from him. He also helped me with various simulations which were vital in my research. I am very thankful to Ivan Mastovsky for his help with setting up the experiments and building the devices. I also would like to thank Bill Mulligan for his great help with solving the high voltage modulator problems during my experiments and building the depressed collector circuit. I also thank him for his training about high voltage safety issues in the lab.

I wish to thank Dr. Alexander Vlasov at SAIC for his help with MAGY simulations. I also thank Monica Blank, Sam Chu, and Kevin Felch at CPI for their help with machining and testing the launcher. I am also thankful to Dr. John Petillo at SAIC for MICHELL simulations. I thank Dr. Jeffrey Neilson at Calabazas Creek Research for his Surf3D code.

I would like to thank all members from the Waves and Beams Division. Especially, I wish to thank my officemate, Colin Joye. We shared our office from the beginning. I had a wonderful time with him during my days at MIT by sharing our routine lives. He also helped me a lot with Matlab programming and electronics. I thank Dr. Yoshi Hidaka and Antoine Cerfon for helping me in the lab. Ksusha Samokhvalova has been my good company with great encouragement to each other. I also thank the rest of the group including Roark Marsh, Antonio Torrezan, Dr. Seong-tae Han, David Tax,

Nick Confoltey, and Paul Woskov.

I had a great time with many friends of mine in Boston. Miye Park, Jeehee Kim, and Jaewon Lee from my church provided me with good memories filled with pleasure and fun. I also thank Pastor David Cho and his wife for their continuous prayer for me. I thank Wonshik Choi and his wife, Soonhee Kim for their encouragements.

I could not have finished this thesis without continuous support from my family in Korea. My parents have always made me feel like I am not alone while I am away from my family. My sisters and brother also made me smile whenever I called them for a break. I thank my parents-in-law for their heartwarming supports.

Finally I would like to thank HyungJoon Cho, my beloved husband, for making our lives worthy and meaningful. He lights up my life. My treasure, who is breathing inside me right now, has made the duration of writing-up this thesis be the happiest moment. You are the most valuable fruit of all in my Ph. D period. S. D. G.

To my beloved parents,

Choon-ho Choi and Sun-ran Lee

Contents

List of Figures

List of Tables

Chapter 1

Introduction

1.1 Comparison of the Gyrotron with Conventional Microwave Sources

The first microwave sources were based on slow wave devices in which the following condition is satisfied,

$$v_{ph} \leq v_e \leq c$$

where v_{ph} is the phase velocity of the wave, v_e is the electron thermal velocity, and c is the velocity of light. As an example of a slow wave device, we may consider the magnetron, which is a crossed-field device, employing a periodic vane-shape RF structure built in a coaxial configuration. A schematic of a magnetron is shown in Fig. 1-1. The microwave field is slowed in the azimuthal direction by the vanes. For traveling wave tubes as shown in Fig. 1-2, the synchronism condition is maintained by reducing the phase velocity of the electromagnetic wave by means of periodic structures on the cavity walls. On the other hand, in klystrons, as shown in Fig. 1-3, the RF electric field can be made to concentrate around a narrow gap within the cavity. The field in the first cavity perturbs the electrons so that they arrive as a bunched beam in the second cavity where energy is extracted. Conventional microwave devices impose limitations on the cavity physical size and output power as the operating frequency increases. The microwave circuit or the cavity structure

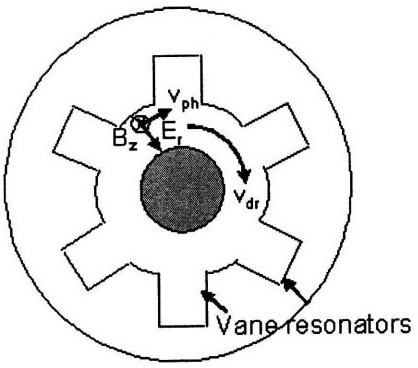

Figure 1-1: Schematic of a six-vane magnetron.

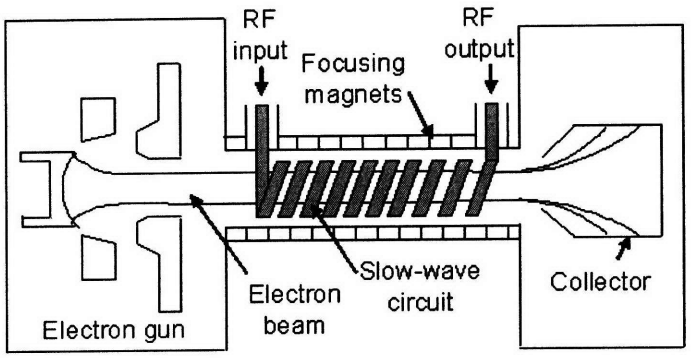

Figure 1-2: Schematic of a TWT.

gets smaller with increasing frequency which consequently puts a limitation on the output power.

The electron cyclotron maser (ECM) is a new type of microwave sources, which is based on relativistic effects for the generation of coherent radiation from free electrons. It allows operation at high frequencies with high output power. The ECM is a fast wave device in which the phase velocity v_{ph} of the electromagnetic wave is greater than the speed of light c ($v_{ph}>c$), therefore, the operating frequencies are not limited by the interaction cavity size. R. Twiss, J. Schneider, and A. Gaponov developed the theory of the electron cyclotron maser (ECM) [1] in the late 1950s. Hirshfield and Wachtel reported the first experiment on the electron cyclotron maser instability

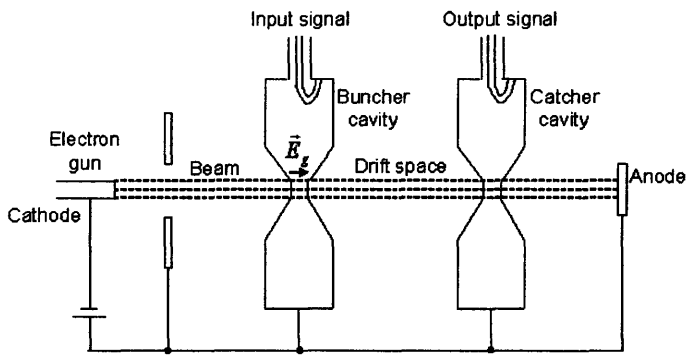

Figure 1-3: Schematic of a two-cavity klystron.

in 1964 [2]. These authors were the first to propose the name "electron cyclotron maser" for these devices. They further analyzed the interaction in [3]. In the mid-1960s, Russian scientists invented a high power version of the ECM, a "gyrotron" device that utilized the adiabatic compression of electrons generated by the high power magnetron injection gun (MIG) as the electron source in an applied external magnetic field. The gyrotron also used a novel cavity consisting of an open resonator with a TE mode near cutoff.

The resonance condition between the electrons and the electromagnetic waves must be satisfied in the interaction region,

$$\omega - k_z v_z \simeq n\Omega_c \tag{1.1}$$

where ω is the electromagnetic wave frequency, k_z is the longitudinal wave number of the wave, v_z is the longitudinal velocity of the electrons, n is the harmonic number, and $\Omega_c = \frac{eB}{\gamma m_e}$ is the cyclotron frequency of the electrons where $\gamma = (1 - v^2/c^2)^{-1/2}$. Here v is the electron velocity, m_e is the electron rest mass and B is the magnetic field. The waveguide mode dispersion is given as,

$$\omega^2 = k_z^2 c^2 + k_\perp^2 c^2. \tag{1.2}$$

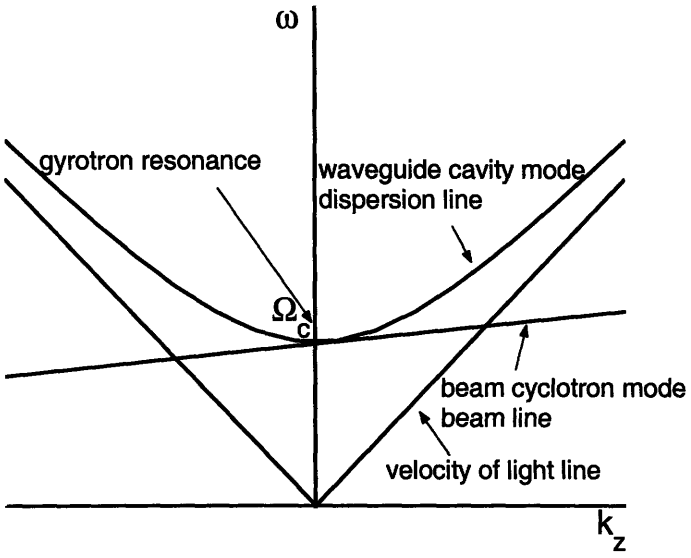

Figure 1-4: Dispersion diagram of a gyrotron oscillator.

From Eq. 1.1 and Eq. 1.2, the uncoupled dispersion diagram of a gyrotron oscillator for the fundamental harmonic is illustrated in Fig. 1-4. As shown in Fig. 1-4, the resonance condition is satisfied where the two curves intersect. For gyrotrons, the most efficient resonance point occurs where k_z is very small.

A chart of obtained average power capabilities as a function of frequency is shown in Fig. 1-5. Gyrotrons fill a gap between lasers and conventional microwave tubes. In the 1980s, plasma physicists recognized that gyrotrons could be used for auxiliary electron cyclotron heating in parallel with ohmic heating of plasmas since the power level and frequency level that were available at that time were very suitable for heating in tokamak plasmas [4]. Thereafter development of high power gyrotrons for plasma heating in tokamaks progressed rapidly.

1.2 Gyrotrons and Fusion

Gyrotrons have emerged as the most promising high power, high efficiency millimeter wave sources suitable for Electron Cyclotron Heating (ECH) and Electron Cyclotron

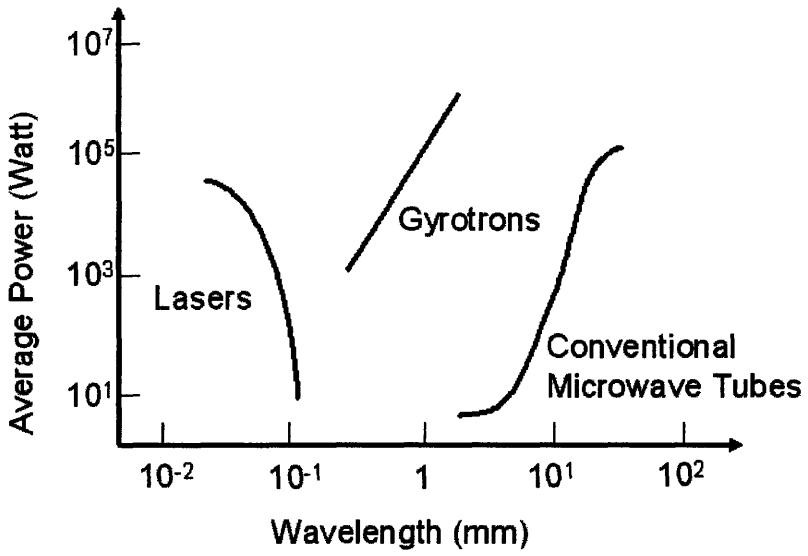

Figure 1-5: Summary of obtained average power capabilities of lasers, conventional tubes, and gyrotrons recreated from [5].

Current Drive (ECCD) in magnetically confined burning plasma experiments [6]. Neoclassical Tearing Modes (NTMs), which are driven by a lack of bootstrap current inside a magnetic island where the pressure profile is flattened, should be avoided for high beta and high confinement tokamaks. Recent studies on NTMs show that NTMs can be suppressed by ECCD [7, 8]. It was reported that 2.3 MW of ECCD was used successfully for suppressing $n/m = \frac{2}{1}$ NTM by off-axis current drive [8, 9].

Research and development is underway on gyrotrons capable of producing over 1 MW of continuous wave power at 110 GHz, 140 GHz, and 170 GHz [10, 11]. Table 1.1 summarizes the operating magnetized plasma devices that use gyrotrons as heating and current drive sources. As shown in Table 1.1, most gyrotrons used for magnetized plasma devices provide between 500 kW and 1 MW power at a frequency range of 80-140 GHz. Recently, a Communication and Power Industries (CPI), Inc. 140 GHz gyrotron operated continuously at an output power of 900 kW for more than 30 minutes [12].

The successful operation of those high power high frequency gyrotrons is promising

Table 1.1: Operating ECH systems with power more than 2 MW.

Plasma device	Institution	ECRH power (MW)	Frequency (GHz)	Pulse duration (s)	Gyrotron company	Coupled energy (MW ×s)
DIII-D tokamak	GA	6.0 (6×1.0)	110	10.0	CPI	2.4×5.0
TCV tokamak	CRPP Lausanne	3.0 (6×0.5) 1.5 (3×0.5)	82.7 110	2.0 2.0	GYCOM TED[a]	2.75×2.0 1.35×2.0
JT 60-U tokamak	JAEA Naka	4.0 (4×1.0)	110	5.0	JAEA/ TOSHIBA (SDC[b])	3.0×2.7 2.8×3.6
T-10 tokamak	NRI Kurchatov Moscow	1.5 (2×0.75) 1.5 (3×0.75) [0.5 (1×0.5)]	129 140 158.5	0.5 0.5 [0.5]	GYCOM	1.25×0.4 1.25×0.4 [0.4×0.4]
ASDEX-U tokamak	IPP Garching	2.8 (4×0.7)	140	2.0	GYCOM	2.3×2.0
LHD stellarator	NIFS Toki	1.0 (2×0.5) 1.6 (2×0.8) 1.6 (4×0.4)	82.7 84 168	2.0 3.0 1.0	GYCOM GYCOM (SDC) TOSHIBA (SDC)	0.6×0.6 0.8×0.8 0.8×0.6
W7-AS stellarator	IPP Garching	0.5 (1×0.5) 0.8 (1×0.8) 1.5 (3×0.5)	70 140 140	2.0 1.0 3.0	CPI (SDC) GYCOM (SDC) GYCOM	0.45×2.0 0.65×1.0 1.2×3.0

[a]Thales Electron Devices
[b]Single-stage Depressed Collector

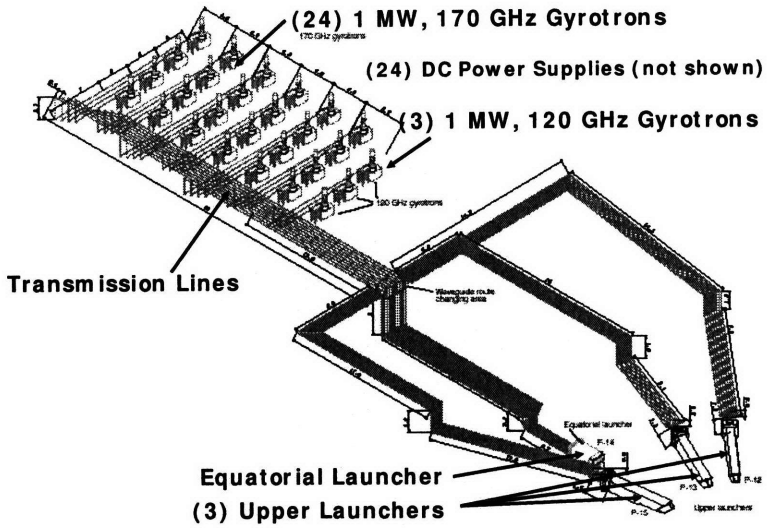

Figure 1-6: ITER ECH / ECCD setup with transmission lines

for future International Thermonuclear Experimental Reactor (ITER) ECH/ECCD systems. On November 21, 2006, the seven participants formally agreed on the funding of the ITER project and Cadarache, France was chosen as the construction site. A 20 MW ECH/ECCD system will be installed in ITER for plasma heating and off-axis current drive for NTM stabilization. Fig. 1-6 shows the ITER ECH/ECCD system including gyrotrons operating for at least 500 sec pulses, transmission lines and launchers. 24 gyrotron units at 170 GHz for ECH/ECCD and 3 gyrotron units at 120 GHz operating in 10 sec pulses for start-up will be installed. To meet these goals, a 170 GHz, 1 MW CW gyrotron is under development in Japan and the Russian Federation (RF) with a cylindrical resonator, and a 2 MW gyrotron at 170 GHz is under development at Forschungszentrum Karlsruhe (FZK) and CRPP in the European Union (EU) using a coaxial resonator. The 1 MW, 120 GHz start-up gyrotrons will be supplied by India. The requirement for delivered power to the plasma is 20 MW and 2 MW, respectively. The ITER ECH/ECCD system requirements are summarized in Table 1.2.

As indicated in Table 1.2, the overall efficiency of the gyrotrons should exceed 50 % in order to operate using the specified power supply. The determination of funding

Table 1.2: ITER ECH/ECCD system requirements

Gyrotron	Power = 1 MW each unit (24 units at 170 GHz) Power = 1 MW each unit (3 units at 120 GHz) Efficiency > 50 %
ECH/ECCD	20 MW delivered to plasma at 170 GHz 2 MW delivered to plasma at 120 GHz Transmission line loss $\sim$ 20 %
Gyrotron power supply	Voltage = 50 kV Current = 45 A

Table 1.3: State-of-the-art megawatt-class long pulse gyrotrons for fusion with frequency greater than 140 GHz (reported in June 2007) [13].

Institution (Country)	Frequency	Cavity Mode	Power	Pulse Duration	Single-Stage Depressed Collector	Efficiency
CPI (US)	140 GHz	$TE_{28,7}$	0.9 MW	30 min	Yes	35 %
TED (EU)	140 GHz	$TE_{28,8}$	0.92 MW	30 min	Yes	44 %
FZK (EU)	170 GHz	$TE_{34,19}$	Not tested yet			
GYCOM (RF)	170 GHz	$TE_{25,10}$	1 MW 0.64 MW	30 sec 300 sec	Yes Yes	50 % 44 %
JAEA (Japan)	170 GHz	$TE_{31,8}$	1 MW 0.6 MW	800 sec 1 hour	Yes Yes	55 % 46 %

for the construction of ITER has led to rapid development of the ITER gyrotrons. Table 1.3 summarizes the most recent results from megawatt-power level gyrotrons for fusion applications from various institutions including the three mentioned institutions for ITER gyrotrons. As reported in Table 1.3, the Japanese JAEA gyrotron has shown remarkable progress at the power level of 1 MW with an efficiency of 55 %, which meets the ITER specification. GYCOM in the Russian Federation also has tested successfully a 170 GHz ITER gyrotron with a power level of 1 MW. The coaxial 2 MW gyrotron developed by FZK in EU has been designed and testing in long pulses is planned soon at CRPP, Lausanne. The results from these institutions brighten the prospects for achieving the CW gyrotrons required for ITER.

1.3 Thesis Outline

The remainder of the thesis consists of 6 chapters. The theory of gyrotrons will be reviewed in Chapter 2 starting with the physics of CRM instabilities. Nonlinear gyrotron theory, a self-consistent description of gyrotrons, gyrotron mode interaction theory, and start-up scenarios in gyrotrons will be discussed in the theory section. A computer code for gyrotron cavity design will be presented. Subsequently, gyrotron efficiency constraints will also be introduced. The experimental setup and diagnostics for the experiments, which are discussed in Chapters 4-6, are described in Chapter 3. Experimental results of a 1.5 MW, 110 GHz gyrotron in an axial configuration are discussed in Chapter 4 and the results are analyzed. The newly obtained analytical description of radiation from a helical cut of a circular waveguide will be treated using geometrical optics and quasi-optical approximations in Chapter 5. A new design of the internal mode converter will follow. Results from the internal mode converter configuration, which was reconfigured from the axial configuration, are presented and analyzed in the remainder of Chapter 5. Results from a single-stage depressed collector experiment and a design study for a two-stage depressed collector will be described in Chapter 6. Finally, the conclusions are given Chapter 7.

Chapter 2

Theory

2.1 Physics of CRM instability

The gyrotron oscillator utilizes electrons that are gyrating in a strong magnetic field that interact with the transverse electric field component of an electromagnetic field in an interaction region. The result of the interaction is a transfer of energy, either increasing or decreasing the wave energy through stimulated emission and absorption. The first theoretical descriptions of the CRM instability were by Twiss, Schneider, and Gaponov [14, 15, 16]. The idea is based on the relativistic dependence of the cyclotron frequency which leads to an azimuthal bunching effect of the gyrating electrons.

The devices based on the induced cyclotron radiation of transiting electron beams are called cyclotron resonance masers (CRM) [2]. A typical arrangement of the CRM interaction consists of helical electron beams gyrating along a static main magnetic field and interacting with electromagnetic waves. The CRM device in which the interaction of helical electron beams with electromagnetic waves takes place in a nearly uniform waveguide near its cutoff frequency is called a "gyrotron" [17].

Imagine that gyrating electrons along the magnetic field are distributed along the azimuth as shown in Fig. 2-1. Initially electrons form a random distribution in phases before they interact with the wave electric field. In this initial stage, the net energy extracted from electrons is 0. There is no energy extraction in the random phase distribution. Electron 1 in Fig. 2-1(a) begins to decelerate while the electric field

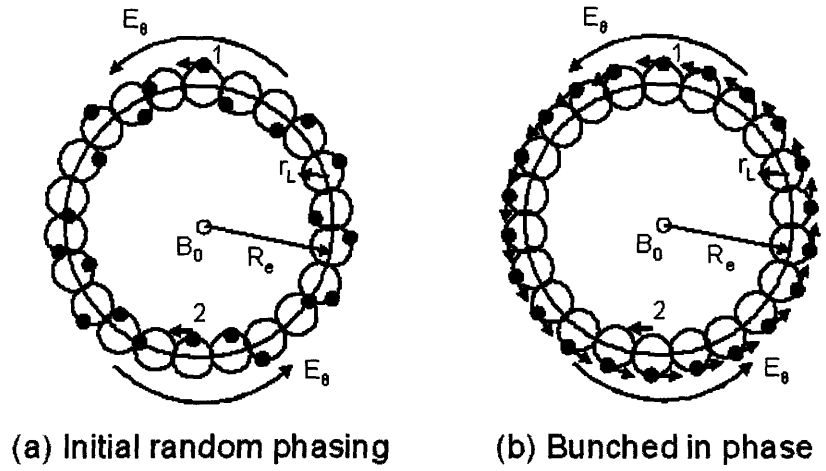

Figure 2-1: The gyrating electron beam along the magnetic field.

E_θ is present. From the synchronism condition equation between the wave and the beam, $\omega - k_z v_z \simeq \Omega_c$, and the cyclotron frequency dependence on the relativistic factor, $\Omega_c = \frac{eB}{\gamma m_e}$, the energy of decelerated electron 1 will have a decreasing value of γ, therefore the cyclotron frequency Ω_c will be increasing. On the other hand, electron 2 will gain energy from the wave thereby the Ω_c will be decreasing. The resultant instability is formed as shown in Fig. 2-1(b). Electrons are in phase with respect to the wave. In this stage, the net energy extracted from electrons is not 0 any more. The wave gains energy from the electrons.

A detail bunching process is simulated in Fig. 2-2 and Fig. 2-3. It is calculated using a nonlinear gyrotron theory which will be described later on. The code calculates energy transfer between the beam and the wave as a function of position, z. In the cyclotron maser instability, the interaction occurs in the transverse direction, and the axial velocity is nearly constant. Essentially z is linearly dependent on time, t, which enables us to track electrons as time proceeds. The position of z is normalized with respect to μ ($\equiv \pi \frac{\beta_{\perp 0}^2}{\beta_{z0}} \frac{L}{\lambda}$), which can be thought as an effective cavity length. The result of the simulation is plotted in a phase space of 32 electrons with a beam energy of 96 kV and an $\alpha (= v_\perp / v_\parallel)$ of 1.3. The magnetic field is 4.47 T which corresponds to a 110 GHz cyclotron frequency. The electric field of the wave is assumed to be

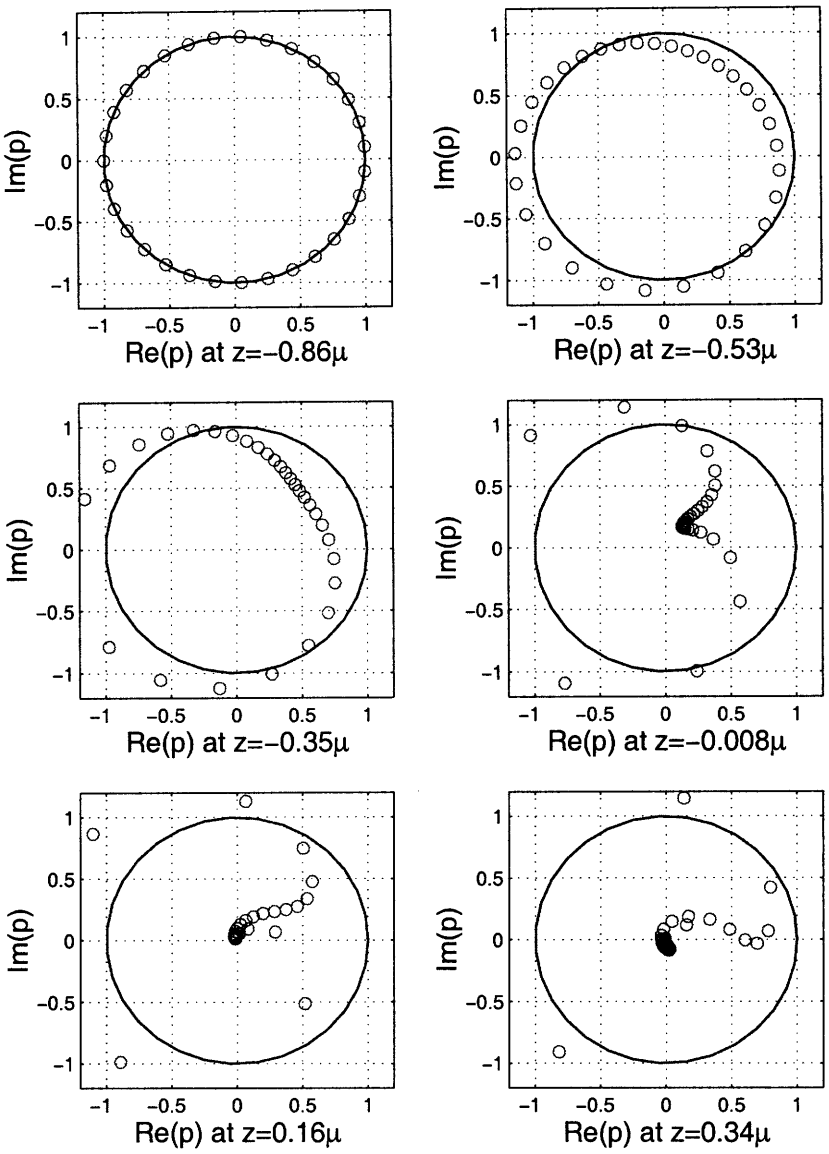

Figure 2-2: 6 snapshots of electron bunching. The electrons are rotating in the clockwise direction and the electric field is applied in $+x$ direction (axis of Re(p)).

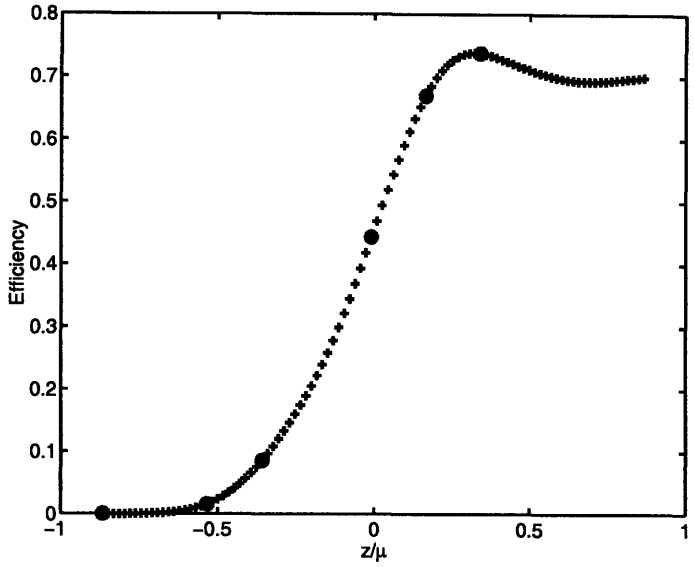

Figure 2-3: The corresponding efficiency plot of Fig. 2-2. Circles represent efficiency points of each snapshot of Fig. 2-2.

a Gaussian. Fig. 2-2 shows 6 snapshots of the electrons in a normalized momentum space. The initial position of $z = -0.86\mu$ is where the electrons enter the interaction region. Therefore the interaction has yet to occur so that the phase distribution of electrons is uniform. As the interaction proceeds, electrons start to form a bunch in phase space. Fig. 2-3 is the corresponding efficiency plot of each snapshot. The maximum efficiency is about 74 %.

2.2 Arrangement of a Gyrotron

A typical gyrotron setup is illustrated in Fig. 2-4. It consists of a MIG (Magnetron Injection Gun) as an electron beam source, a cavity as an interaction region, an internal mode converter for transforming the cavity mode into a Gaussian beam, and a collector as a region for dumping the energy-depleted "spent" beam. Electrons emitted from a cathode surface follow initially an adiabatic compression towards a static main magnetic field flattop. The adiabatic compression can be expressed in an

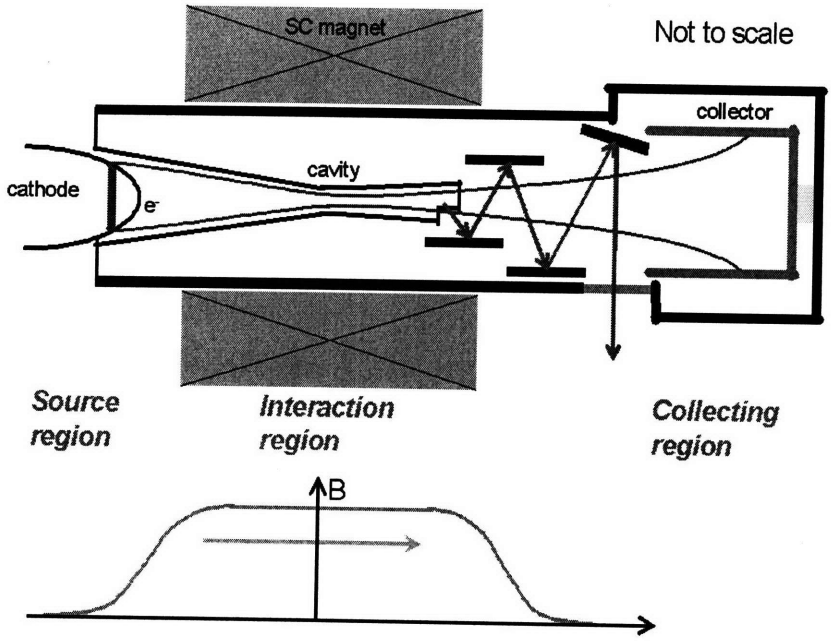

Figure 2-4: The arrangement of a gyrotron.

invariant form as follows,

$$\frac{p_\perp^2}{B} = const. \tag{2.1}$$

As electrons propagate to the higher magnetic field region, their perpendicular momentum is increasing accordingly. With sufficiently high perpendicular momentum, the electrons start to enter the interaction region in which the magnetic field is flat. The transverse electric field of the wave in the cavity is now amplified due to the loss of the rotational energy of the electrons. The output wave is converted to a fundamental Gaussian mode while it is traveling through the internal mode converter. The propagation direction is changed at the final mirror and the output microwave beam is transmitted through the window. The spent beam, which is the leftover electron beam after experiencing the interaction, lands on the collector.

2.3 Nonlinear Theory

This section follows a generalized nonlinear theory due to Nusinovich and Danly and Temkin [18]. The purpose of this section is to calculate the energy extracted from the electrons by solving the equations of motion of the electrons in the presence of electromagnetic fields. The calculated extracted energy after the interaction between the electrons and the wave can be simply formulated with several normalized parameters (F, μ, Δ), making the optimization of the gyrotron efficiency easier. Since the theory is generalized for gyrotrons operating at any harmonic and in any waveguide mode, we can find a zone of high efficiency by optimizing the normalized parameters.

The equations of motion of an electron in electric and magnetic fields are given by,

$$\frac{d\mathcal{E}}{dt} = -e\mathbf{v}\cdot\mathbf{E} \tag{2.2}$$

$$\frac{d\mathbf{p}}{dt} = -e\mathbf{E} - \frac{e}{c}\mathbf{v}\times\mathbf{B}, \tag{2.3}$$

where $\mathcal{E} = \gamma m_e c^2$ is the electron energy, γ is the relativistic factor, and $|\mathbf{p}| = \gamma\beta m_e c$ is the electron momentum. This theoretical treatment assumes a fixed axial field profile of the electromagnetic field. The self-consistent field profile is discussed in the next section. RF magnetic field terms can be dropped near cutoff, therefore $\mathbf{B} = B_0\hat{\mathbf{z}}$. Now the energy variable, $\mathcal{E}$ can be reexpressed as a normalized energy variable, $w = 1 - (\gamma/\gamma_0)$ and the time variable can also be converted to a normalized axial position, $Z = (\omega z)/(\beta_{z0}c)$ using $z = \beta_z ct$. Therefore Eq. 2.2 can be rewritten as,

$$\frac{dw}{dZ} = \frac{e}{(m_e c)^2\omega}\frac{\beta_{z0}}{\gamma_0\gamma\beta_z}\mathbf{p}\cdot\mathbf{E} \tag{2.4}$$

where β_{z0} and γ_0 are the initial values of β_z and γ at the cavity entrance. $\mathbf{p}$ and $\mathbf{E}$ are now expressed in complex notation using following equations,

$$\mathbf{p} = p_x + ip_y = |p_+|\cos\xi + i|p_+|\sin\xi = |p_+|e^{i\xi}$$

$$\mathbf{E} = E_x + iE_y = |E_+|\cos i(\omega t+\psi) + i|E_+|\sin i(\omega t+\psi) = |E_+|e^{i(\omega t+\psi)},$$

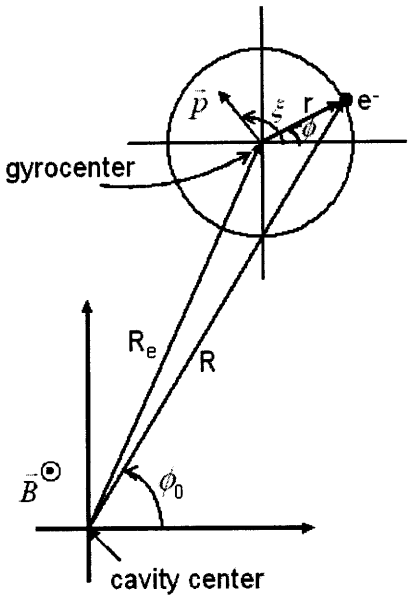

Figure 2-5: The arrangement of a coordinate.

where ξ is the angle of the electron momentum about the gyrocenter as shown in Fig. 2-5.

$$\begin{aligned}\mathbf{p}\cdot\mathbf{E} &= p_xE_x + p_yE_y = |p_+||E_+|(\cos\xi\cos(\omega t+\psi)+\sin\xi\sin(\omega t+\psi)) \\ &= |p_+||E_+|\cos(\xi-(\omega t+\psi)) = Re(p_+^*E_+)\end{aligned}$$

Therefore, Eq. 2.4 and Eq. 2.3 for the energy and momentum equations can be expressed as follows,

$$\frac{dw}{dZ} = \frac{e}{(m_ec)^2\omega}\frac{\beta_{z0}}{\gamma_0\gamma\beta_z}Re(p_+^*E_+) \tag{2.5}$$

$$\frac{d\xi}{dZ} = \frac{\beta_{z0}\omega_c}{\beta_z\omega} - \frac{e\beta_{z0}}{\omega\beta_z|p_+|}Im(p_+^*E_+) \tag{2.6}$$

Here, $\omega_c = eB_0/m_ec\gamma$.

Now, the electric field for a TE_{mp} mode near cutoff can be written in cylindrical coordinates, (R,ϕ_0), centered at the cavity center as shown in Fig. 2-5. Fig. 2-5

represents the coordinate of an electron gyrating along the cavity center at a beam radius R_e. The center of the Larmor radius r of the gyrating electron is marked as the gyrocenter.

$$\mathbf{E} = (E_R\hat{R} + E_{\phi_0}\hat{\phi}_0)e^{i(\omega t+\psi)} \tag{2.7}$$

$$E_R = i(m/k_\perp R)E_0 f(z)J_m(k_\perp R)e^{-im\phi_0} \tag{2.8}$$

$$E_{\phi_0} = E_0 f(z)J'_m(k_\perp R)e^{-im\phi_0} \tag{2.9}$$

where $k_\perp = \nu_{mp}/a$, and ν_{mp} is the pth root of $J'_m(x) = 0$ and a is the cavity radius. Now the electric field in the $(\hat{R}, \hat{\phi}_0)$ coordinate will be reexpressed in the coordinate $(\hat{r}, \hat{\phi})$ centered at the electron gyrocenter to obtain the synchronous field ($\omega \simeq n\Omega_c$) using Graf's formula for Bessel functions,

$$\mathbf{E} = (E_{rn}\hat{r} + E_{\phi n}\hat{\phi})e^{i(\omega t+\psi)} \tag{2.10}$$

$$E_{rn} = i\frac{n}{k_\perp r}E_0 f(z)J_{m\pm n}(k_\perp R_e)J_n(k_\perp r)e^{-im\phi_0}e^{-in(\phi-\phi_0)} \tag{2.11}$$

$$E_{\phi n} = E_0 f(z)J_{m\pm n}(k_\perp R_e)J'_n(k_\perp r)e^{-im\phi_0}e^{-in(\phi-\phi_0)}. \tag{2.12}$$

The electric field of a TE_{mp} cavity mode is then written as

$$E_+ = -E_r \sin\left[\theta + \psi - (m-n)\phi_0\right] e^{i\phi} + E_\phi \cos\left[\theta + \psi - (m-n)\phi_0\right] ie^{i\phi} \tag{2.13}$$

where $E_r = |E_{rn}|$ and $E_\phi = |E_{\phi n}|$ and $\theta = \omega t - n\phi$. The slowly varying gyrophase θ is now introduced and the equation of ξ of Eq. 2.6 is going to be transformed to the equation of θ. The angle of electron momentum, ξ has the relationship with the electron phase ϕ as $\xi = \phi + \pi/2$.

Using Eq. 2.13, the equations of Eq. 2.5 and Eq. 2.6 can be rewritten as,

$$\frac{dw}{dZ} = \frac{e}{\gamma_0 m_e c\omega}p'_\perp E_\phi \cos\left[\theta + \psi - (m-n)\phi_0\right] \tag{2.14}$$

$$\frac{d\theta}{dZ} = \delta_0 - w - \frac{ne}{\gamma_0 m_e c\omega}\frac{(1-w)}{p'_\perp}E_r \sin\left[\theta + \psi - (m-n)\phi_0\right] \tag{2.15}$$

where $p'_\perp = |p_+|/(\gamma_0 m_e c) = (\beta_{\perp 0}^2 - 2w + w^2)^{1/2}$, and $\delta_0 = 1 - n\Omega_{c0}/\omega$ is the magnetic field detuning parameter where $\Omega_{c0} = eB/m_e c\gamma_0$. Let $\psi - (m-n)\phi_0$ be $\pi/2$ and set $\omega \simeq n\Omega_{c0}$, then the above equations (Eq. 2.14 and Eq. 2.15) can be reexpressed to the reduced forms,

$$\frac{dw}{dZ} = \frac{E_\phi}{nB_0} p'_\perp \sin\theta \tag{2.16}$$

$$\frac{d\theta}{dZ} = \delta_0 - w + \frac{E_r}{B_0}\frac{(1-w)}{p'_\perp}\cos\theta. \tag{2.17}$$

From Eq. 2.16, the action of the azimuthal electric field on the electron leads to an inertial bunching, which results in the variation of the electron energy. The phase variation occurs due to the radial electric field and the inertial bunching and, in fact, in gyrotrons, the inertial bunching is the dominant form of phase bunching.

The argument of the Bessel function J_n of the electric field can be expressed in terms of the energy variable

$$k_\perp r \approx \frac{\omega}{c} r \approx n\frac{\gamma\beta_\perp}{\gamma_0} = n\beta_{\perp 0}\left(1 - \frac{1}{\beta_{\perp 0}}(2w - w^2)\right)^{1/2} = np'_\perp.$$

We now redefine the energy and the axial position variables as

$$u \equiv \frac{2}{\beta_{\perp 0}^2} w = \frac{2}{\beta_{\perp 0}^2}\left(1 - \frac{\gamma}{\gamma_0}\right) \tag{2.18}$$

$$\zeta \equiv \frac{\beta_{\perp 0}^2}{2} Z = \pi\frac{\beta_{\perp 0}^2}{\beta_{z0}}\frac{z}{\lambda}, \tag{2.19}$$

and introduce a normalized interaction length, μ as

$$\mu \equiv \pi\frac{\beta_{\perp 0}^2}{\beta_{z0}}\frac{\mathrm{L}}{\lambda}. \tag{2.20}$$

Eq. 2.14 and 2.15 are rewritten as follows,

$$\frac{du}{d\zeta} = 2\left(\frac{2^n n!}{n^n \beta_{\perp 0}^{n-1}}\right) Ff(\zeta)\frac{p'_\perp}{\beta_{\perp 0}} J'_n(np'_\perp)\sin\theta \tag{2.21}$$

$$\frac{d\theta}{d\zeta} = \Delta - u - n\left(\frac{2^n n!}{n^n \beta_{\perp 0}^{n-1}}\right) Ff(\zeta)\frac{\beta_{\perp 0}(1 - \beta_{\perp 0}^2 u)/2}{p'^2_\perp} J_n(np'_\perp)\cos\theta \tag{2.22}$$

where the normalized field amplitude F is defined as,

$$F \equiv \frac{E_0}{B_0}\beta_{\perp 0}^{(n-4)}\left(\frac{n^{n-1}}{n!2^{n-1}}\right)J_{m\pm n}(k_\perp R_e), \tag{2.23}$$

and the detuning parameter Δ is defined as,

$$\Delta \equiv \frac{2\delta_0}{\beta_{\perp 0}^2} = \frac{2}{\beta_{\perp 0}^2}\left(1 - \frac{n\Omega_{c0}}{\omega}\right). \tag{2.24}$$

We have now introduced three important parameters: F, μ, and Δ. The equations of motion (Eq. 2.21 and 2.22) will eventually be expressed using only these three parameters.

Under the condition of weakly relativistic beam,

$$n\beta_{\perp 0}^2/2 \ll 1, \tag{2.25}$$

$p'_\perp$ can be approximated by,

$$p'_\perp \approx (\beta_{\perp 0}^2 - 2w)^{1/2} = \beta_{\perp 0}(1-u)^{1/2}.$$

Furthermore using the condition of Eq. 2.25, the Bessel function $J_n(np'_\perp)$ can be approximated by polynomials using,

$$\begin{aligned} J_m(x) &= \frac{1}{m!}\left(\frac{x}{2}\right)^m, x \ll 1, m \neq 0 \\ &= 1 - \frac{1}{4}x^2, \quad x \ll 1, m = 0. \end{aligned}$$

As a result, Eq. 2.21 and 2.22 are finally expressed as three parameters, F, μ, and Δ,

$$\frac{du}{d\zeta} = 2Ff(\zeta)(1-u)^{n/2}\sin\theta \tag{2.26}$$

$$\frac{d\theta}{d\zeta} = \Delta - u - nFf(\zeta)(1-u)^{n/2-1}\cos\theta. \tag{2.27}$$

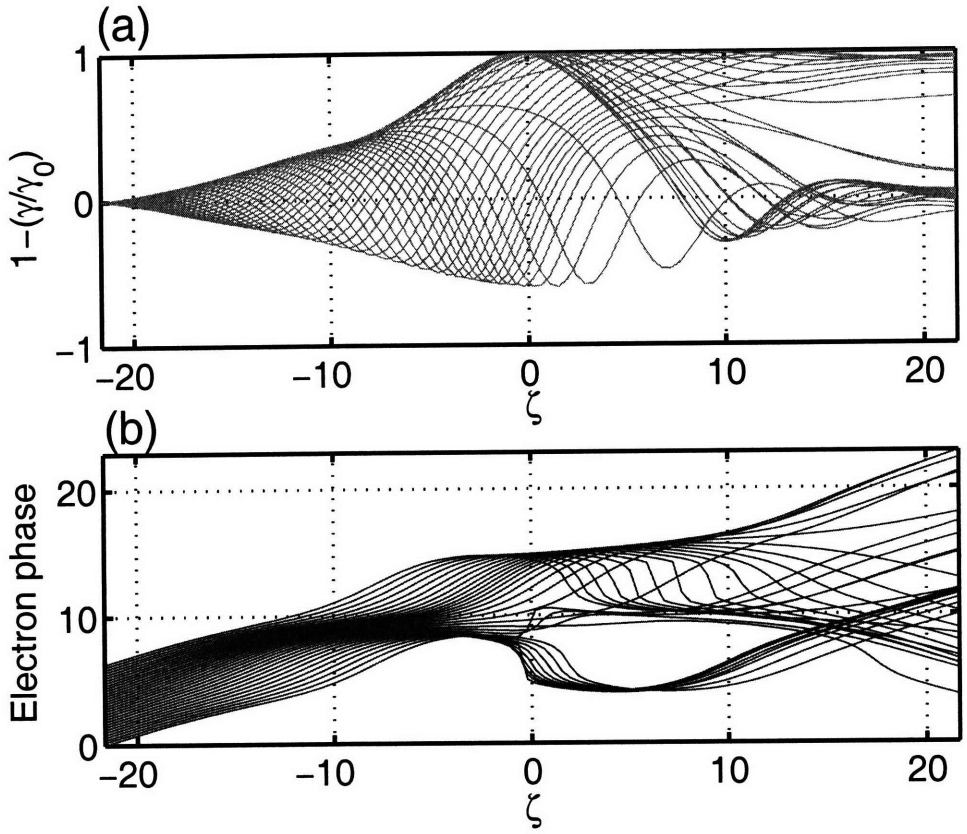

Figure 2-6: (a) The electron normalized energy $(1 - (\gamma/\gamma_0))$ plot, (b) the electron phase plot. The number of particle is 32.

The total interaction efficiency, η is formulated by,

$$\eta \equiv \frac{\gamma_0 - \gamma}{\gamma_0 - 1} = \frac{\beta_{\perp 0}^2}{2(1 - \gamma_0^{-1})}\eta_\perp, \tag{2.28}$$

and the transverse efficiency, $\eta_\perp$ is,

$$\eta_\perp = < u(\zeta_{out}) >_{\theta_0}, \tag{2.29}$$

where the initial conditions are $\theta = \theta_0 \in [0, 2\pi)$ and $u = 0$. Now, the transverse efficiency depends only on the three normalized parameters, F, μ, and Δ.

Fig. 2-6 and 2-7 are examples of the simulation of the nonlinear differential equa-

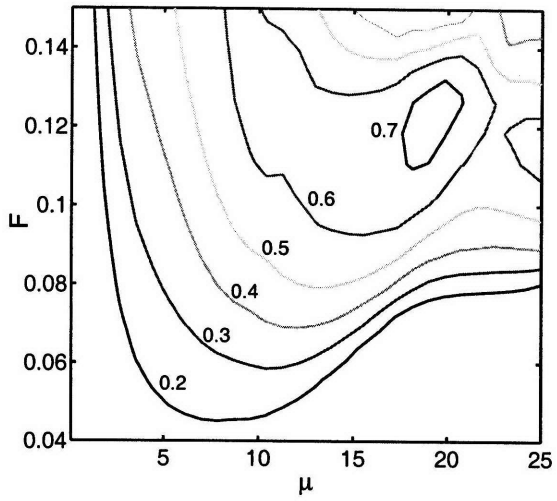

Figure 2-7: The transverse efficiency $\eta_\perp$ contour plot as a function of normalized field amplitude F and normalized interaction length μ. Each number near contour lines represents the transverse efficiency, $\eta_\perp$.

tions 2.26 and 2.27. In this simulation, the axial field profile, $f(z)$, is assumed to be a Gaussian,

$$f(z) = e^{-(2\zeta/\mu)^2}$$

and the limits for the integration for the axial field profile are chosen to be $-\sqrt{3}\mu/2 \leq \zeta \leq \sqrt{3}\mu/2$. α=1.3 and $\delta \simeq$0.48 were used in the simulation. The number of particles chosen was 32 and the number of mesh points in ζ was 100. Fig. 2-6 is the simulation result of the electron normalized energy u defined in Eq. 2.18 and the phase of 32 electrons. As seen in Fig. 2-6, all electrons have 0 initial normalized energy (Fig. 2-6(a)) at $\zeta = 0$ where the phases of the electrons (Fig. 2-6(b)) are distributed uniformly between 0 and 2π. As the electrons propagate in the axial direction, the normalized energy of the electrons changes and at the same time, the phase of the electrons starts to bunch (Fig. 2-6(b)). At the end of the interaction cavity, the net energy u becomes positive which indicates there is an energy loss from the electrons. Fig. 2-7 is the result of the transverse efficiency calculated from Eq. 2.29 following the simulation of u from the differential equation as a function of the normalized field amplitude F and

the normalized interaction length μ. The maximum transverse efficiency of over 70 % ($\eta_\perp$ ~0.7) is shown in the contour plot, corresponding to F and μ of approximately 0.12 and 18, respectively.

The field amplitude F is related to the beam current by the energy balance equation,

$$Q_T = \frac{\omega U}{P}$$

where Q_T is the cavity total quality factor, U is the total stored energy, and P is the power dissipated by Q_T. The power dissipated P is written as

$$P = \eta I_A V = \frac{mc^2}{e}\frac{\gamma_0\beta_0^2}{2}\eta_\perp I_A \tag{2.30}$$

where I_A is the beam current. We use the symbol I_A here for the actual current in Amperes, while I will be used for the normalized current defined below.

For the case of stationary oscillations, the energy balance equation can be written as

$$|F|^2 = \eta_\perp I. \tag{2.31}$$

The total stored energy U is expressed by

$$\begin{aligned} U &= \frac{1}{4\pi}\int_V |\mathbf{E}|^2 \\ &= |E_0|^2\frac{\lambda^2}{16\pi^2}(\nu_{mp}^2 - m^2)J_m^2(\nu_{mp})\int_0^L |f(z)|^2 dz \end{aligned} \tag{2.32}$$

Using Eqs. 2.23, 2.30, 2.31, 2.32, the normalized beam current I is obtained,

$$I = 8\frac{eI_A}{mc^3}Q\left(\frac{n^n}{2^n n!}\right)^2 \frac{\beta_{\perp 0}^{2(n-2)}}{\gamma_0\beta_{z0}} \frac{J_{m\pm n}^2(k_\perp R_e)}{(\nu_{mp}^2 - m^2)J_m^2(\nu_{mp})\int_0^\mu |f(z)|^2 d\zeta}. \tag{2.33}$$

When the axial field profile $f(z)$ is given by a Gaussian profile,

$$f(z) = e^{-(k_z z)^2} or f(\zeta) = e^{-(2\zeta/\mu)^2}.$$

Eq. 2.33 can then be written as,

$$I = 0.238 \times 10^{-3} \left(\frac{Q_T I_A}{\gamma_0}\right) \beta_{\perp 0}^{2(n-3)} \frac{\lambda}{L} \left(\frac{n^n}{2^n n!}\right)^2 \frac{J_{m\pm n}^2(k_\perp R_e)}{(\nu_{mp}^2 - m^2) J_m^2(\nu_{mp})}. \tag{2.34}$$

2.4 Self-Consistent Field Theory

In Section 2.3 we have dealt with the nonlinear theory assuming the RF field is not changed by electron beam modulation, in which it is simple enough to understand the relationships of the efficiency, field strength, and the interaction length. This section will describe the dynamics of gyrotrons formulated by a system of coupled, nonlinear, ordinary differential equations for the electron beam and RF fields by following the calculations in [19]. These equations are to be solved self-consistently by satisfying the RF field boundary conditions.

Adiabatic equations for electron motion

As described in Section 2.3, the starting point of describing electron motion is the Lorentz force equation,

$$\mathbf{a} = -\frac{e}{m_e}(\mathbf{E} + \mathbf{v} \times \mathbf{B}) \tag{2.35}$$

Let's introduce a normalized momentum variable for simplicity,

$$\hat{\mathbf{v}} = \gamma \mathbf{v}$$

where γ is the relativistic factor.

We are using the coordinate system in Fig. 2-5 described in Section 2.3. By transforming the electron transverse momentum from cartesian coordinates,

$$\hat{v}_x + i\hat{v}_y = i\hat{v}_\perp e^{i(\Omega\tau + \phi)}$$

where $\tau = t - t_0$ and t_0 is the time that the electron enters the interaction region,

Eq. 2.35 can be written as follows,

$$\dot{\hat{v_\perp}} = -a_x \sin(\Omega\tau + \phi) + a_y \cos(\Omega\tau + \phi) \tag{2.36}$$

$$\hat{v_\perp}(\dot{\phi} + \Omega - \Omega_c/\gamma) = -a_x \cos(\Omega\tau + \phi) - a_y \sin(\Omega\tau + \phi) \tag{2.37}$$

$$\dot{v_z} = a_z \tag{2.38}$$

where $\Omega_c = eB_0/m_e$.

Consider the electric field of a TE circular waveguide mode. The electric field of a TE_{mp} mode is given by,

$$\mathbf{E}_\perp = Re\left[C_{mp}\left(k_{mp}J'_m(k_{mp}R)\hat{\theta} + i\frac{m}{R}J_m(k_{mp}R)\hat{R}\right)f(z)e^{i(\omega t - m\theta)}\right] \tag{2.39}$$

where the normalization constant C_{mp} is given by

$$C_{mp} = \frac{1}{\sqrt{\pi(\nu_{mp}^2 - m^2)}J_m(\nu_{mp})}$$

and $k_{mp} = \nu_{mp}/r_w$ where ν_{mp} is the nth zero of the J'_m and r_w is the waveguide wall radius.

From Eq. 2.35 and applying the Graf's formula for Bessel functions introduced in Eq. 2.10, Eq. 2.36 and Eq. 2.37 are changed to

$$\begin{aligned}\frac{d\hat{v_\perp}}{dt} &= -\frac{e}{2m_e}k_{mp}C_{mp}J_{m-n}(k_{mp}R_e)[J_{n-1}(k_{mp}r) - J_{n+1}(k_{mp}r)] \\ &\quad \times|f|\cos[(\omega - n\Omega)\tau + \omega t_0 - n\phi - \psi]\end{aligned} \tag{2.40}$$

$$\begin{aligned}(\phi + \Omega - \Omega_c/\gamma)\hat{v_\perp} &= -\frac{e}{2m_e}k_{mp}C_{mp}J_{m-n}(k_{mp}R_e)[J_{n-1}(k_{mp}r) + J_{n+1}(k_{mp}r)] \\ &\quad \times|f|\sin[(\omega - n\Omega)\tau + \omega t_0 - n\phi - \psi]\end{aligned} \tag{2.41}$$

Here, we have expressed the axial dependence of the RF field $f(z)$ by the complex profile function

$$f(z) = |f(z)|e^{-i\psi(z)}.$$

Introducing the new slow time scale phase variable

$$\Lambda = \left(\frac{\omega}{n} - \Omega\right)\tau + \frac{\omega}{n}t_0 - \phi$$

and expressing the Larmor radius according to

$$r = r_L = \frac{\hat{v_\perp}}{\Omega_c}$$

leads to

$$\begin{aligned}
\frac{d\hat{v_\perp}}{dt} &= -\frac{e}{2m_e}k_{mp}C_{mp}J_{m-n}(k_{mp}R_e)\left[J_{n-1}\left(\frac{m_e k_{mp}\hat{v_\perp}}{eB_0}\right) - J_{n+1}\left(\frac{m_e k_{mp}\hat{v_\perp}}{eB_0}\right)\right] \\
&\quad \times |f|\cos(n\Lambda - \psi) \qquad (2.42) \\
\frac{d\Lambda}{dt} &= \frac{e}{2m_e}k_{mp}\frac{C_{mp}}{u_\perp}J_{m-n}(k_{mp}R_e)\left[J_{n-1}\left(\frac{m_e k_{mp}\hat{v_\perp}}{eB_0}\right) + J_{n+1}\left(\frac{m_e k_{mp}\hat{v_\perp}}{eB_0}\right)\right] \\
&\quad \times |f|\sin(n\Lambda - \psi) + \frac{\omega}{n} - \frac{\Omega_c}{\gamma}. \qquad (2.43)
\end{aligned}$$

Wave equation for RF field profile function

Starting with the Maxwell curl equations,

$$\begin{aligned}
\nabla \times \mathbf{H} &= \mathbf{J} + \epsilon\frac{\partial \mathbf{E}}{dt} \\
\nabla \times \mathbf{E} &= -\mu\frac{\partial \mathbf{H}}{dt}
\end{aligned}$$

the wave equation of RF field can be obtained,

$$\nabla^2\mathbf{E} - \frac{1}{c^2}\frac{\partial^2\mathbf{E}}{dt^2} = \mu\frac{\partial \mathbf{J}}{dt}. \qquad (2.44)$$

Assuming the steady state time-dependence $e^{i\omega t}$, the current density $\mathbf{J}$ is given by,

$$\mathbf{J}_\omega(\mathbf{R}, t) = \mathbf{J}_\omega(\mathbf{R})e^{i\omega t} \qquad (2.45)$$

where,

$$\mathbf{J}_\omega(\mathbf{R}) = \frac{1}{2\pi}\int_0^{2\pi} \mathbf{J}(\mathbf{R},t)e^{-i\omega t}d(\omega t).$$

Substituting Eq. 2.45 into Eq. 2.44 gives the time-independent wave equation,

$$\nabla^2\mathbf{E} + \frac{\omega^2}{c^2}\mathbf{E} = i\mu\omega\mathbf{J}_\omega. \tag{2.46}$$

The electric field for a TE_{mp} circular mode is expressed as,

$$\mathbf{E}(\mathbf{R},t) = Re[\mathbf{E}(\mathbf{R})e^{i\omega t}] \tag{2.47}$$

where,

$$\mathbf{E}(\mathbf{R}) = \mathbf{E}_\perp(\mathbf{R})\mathbf{E}_{mp}(R,\theta)f(z) \tag{2.48}$$

and

$$\mathbf{E}_{mp}(R,\theta) = C_{mp}\left[k_{mp}J'_m(k_{mp}R)\hat{\theta} + \frac{im}{R}J_m(k_{mp}R)\hat{R}\right]e^{-imt}. \tag{2.49}$$

Substituting Eq. 2.48 into Eq. 2.46, one obtains,

$$\mathbf{E}_{mp}\left[\frac{d^2}{dz^2} + \frac{\omega^2}{c^2} - k_{mp}^2\right]f(z) = i\mu\omega\mathbf{J}_\omega. \tag{2.50}$$

Using the orthonormality of $\mathbf{E}_{mp}$, we multiply Eq. 2.50 by $\mathbf{E}^*_{mp}$ and integrate over the waveguide cross section. The resultant equation is written as follows,

$$\left[\frac{d^2}{dz^2} + \frac{\omega^2}{c^2} - k_{mp}^2\right]f(z) = i\mu\omega\int \mathbf{E}^*_{mp}\cdot\mathbf{J}_\omega da. \tag{2.51}$$

In order to complete Eq. 2.51, the right hand side of Eq. 2.51 has to be evaluated. One notes that the transverse current density $\mathbf{J}_\perp$ is expressed as

$$\mathbf{J}_\perp = \rho\mathbf{v}_\perp \tag{2.52}$$

where ρ is the linear charge density. If an idealized electron beam with a single guiding radius R_e is considered, $\rho = -I_0/v_z$ where I_0 is the DC beam current. Substituting

Eq. 2.49 and Eq. 2.52 using the linearized expression for the current density into the right hand side of Eq. 2.51 leads to,

$$\begin{aligned}\int \mathbf{E}^*_{mp} \cdot \mathbf{J}_\omega da &= -I_0 k_{mp} C_{mp} \frac{1}{2\pi} \\ &\times \int_0^{2\pi} d(\omega t) \frac{v_\perp}{v_z} J_{m-1}(k_{mp} R) e^{-i(\omega t - (m-1)\theta - \Omega\tau - \phi)}. \end{aligned} \quad (2.53)$$

Using Graf's formula for Bessel functions (Eq. 2.10) and considering the interaction with a single cyclotron harmonic Eq. 2.53 yields,

$$\begin{aligned}\int \mathbf{E}^*_{mp} \cdot \mathbf{J}_\omega da &= -I_0 k_{mp} C_{mp} J_{m-n}(k_{mp} R_e) \\ &\times \frac{1}{2\pi} \int_0^{2\pi} d(\omega t) \frac{v_\perp}{v_z} J_{n-1}(k_{mp} r) e^{-i[(\omega - n\Omega)\tau + \omega t_0 - \phi]}. \end{aligned} \quad (2.54)$$

In order to express the final formula of the field equation with respect to a slowly varying phase variable, Λ, the following equations are used. Since,

$$t = t_0 + \int \frac{dz}{v_z}$$

and,

$$v_z \approx v_{z0},$$

where v_{z0} is the initial longitudinal velocity, the average over ωt in Eq. 2.54 can be approximately replaced by an average over ωt_0. Moreover, since

$$\Lambda_0 = \Lambda(t = t_0) = \frac{\omega}{n t_0} - \phi$$

where $\phi_0 = \phi(t = t_0)$, then,

$$d(\omega t_0) = n d\Lambda_0.$$

Therefore one can obtain the final equation for the RF profile function,

$$\left[\frac{d^2}{dz^2}+\frac{\omega^2}{c^2}-k_{mp}^2\right]f(z) = -i\mu\omega I_0 k_{mp} C_{mp} J_{m-n}(k_{mp}R_e) \times \int_0^{2\pi}\frac{v_\perp}{v_z}J_{n-1}\left(\frac{k_{mp}u_\perp}{\Omega_c}\right)e^{-in\Lambda}d\Lambda_0 \qquad (2.55)$$

Self-consistent single mode gyrotron theory

Finally Eq. 2.42, Eq. 2.43 and Eq. 2.55 constitute a set of non-linear, coupled equations for the gyrotron.

Using a dimensionless quantity, ζ

$$\zeta = \frac{\omega z}{v_{z0}}$$

the time variable is conveniently changed to the dimensionless length variable.

$$\frac{d}{dt} = \frac{v_{z0}}{\omega v_z}\frac{d}{dz}$$

Therefore the equations (2.42, 2.43, and 2.55) are reexpressed in terms of ζ. The nonlinear, coupled equations are solved self-consistently and the proper boundary conditions have to be satisfied. The input RF boundary condition for a gyrotron is a growing evanescent wave and the output RF boundary condition is an outgoing traveling wave. The formulation of the boundary condition for the RF field profile function at the resonant input is

$$|f| = |f(\zeta=\zeta_0)|e^{k_0(\zeta-\zeta_0)}$$

where

$$k_0 = \sqrt{k_\perp^2(\zeta_0)-\omega^2/c^2}.$$

And the output RF boundary condition is formulated as

$$\frac{df}{d\zeta} = -ik_{\zeta_f}f(\zeta_f)$$

where

$$k_{\zeta_f} = \sqrt{\omega^2/c^2 - k_\perp^2(\zeta_f)}.$$

For the fixed axial field profile, basic features of the gyrotron can be provided by a set of dimensionless parameters, (F, μ, Δ) at the first stage of designing the gyrotron cavity as discussed in Section 2.3. However, the self-consistent calculation must be followed for determining the cavity shape and gyrotron parameters such as alpha value, beam current and beam voltage in order to determine the overall efficiency by considering an altered axial field profile due to the electron beam.

2.5 Mode Interaction Theory

In Section 2.3 and Section 2.4 we have assumed that one mode is solely excited in the cavity by the electron beam. However, in highly overmoded gyrotron cavities, the spectrum of modes is very dense so that the electrons can interact with several modes simultaneously (not only with the designed cavity mode), which may cause unstable and low efficiency operation of the gyrotron. Therefore, one of the most important challenges in pursuing high efficiency gyrotrons is to avoid the mode competition between a design mode and unwanted modes. Single mode operation is indeed possible if the cavity shape is well designed and the starting scenario is well analyzed in a given cavity design. The mode interaction theory in gyrotrons is well described in the review paper of Nusinovich [5, 20, 21].

In this section, the fully nonlinear, time-dependent multimode formulation for conventional gyrotron waveguide cavities will be treated by following the approach of Fliflet et al. in [22].

The electron transit time is

$$t_{tr} = \frac{L}{v_{z0}}$$

where L is the length of the interaction region. Typically the transit time, t_{tr}, is much

shorter than the cavity field decay time which is defined by

$$t_{decay} = \frac{Q}{\omega}.$$

The condition, $t_{tr} \ll t_{decay}$, allows one to neglect changes in the mode amplitudes during the pass of one electron through the cavity. Therefore one can express the transverse electric field as a superposition of modes of the cavity incorporated in the complex mode amplitudes $A_n(z,t)$ which can be assumed to be fixed during one electron pass,

$$\mathbf{E}(r,\theta,z,t) = \sum_{n=1}^{N} A_n(z,t)\mathbf{E}_n(r,\theta,z)e^{-i\omega_0 t} \tag{2.56}$$

where n is the mode index, N is the number of modes and $\mathbf{E_n} = \hat{z} \times \nabla_\perp \Psi$ is the waveguide transverse mode vector function and Ψ is the corresponding scalar mode function which satisfies a Helmholtz equation with respect to the transverse coordinates.

As we have discussed already in Section 2.4, the transverse electric field in Eq. 2.56 is plugged into the wave equation in Eq. 2.44 and the equation is integrated over the cavity cross section. The resultant equation is expressed as

$$\left[\frac{\partial^2}{\partial z^2} + \frac{\omega_0^2 - \omega_{nc}^2}{c^2} + 2i\frac{\omega_0}{c^2}\frac{\partial}{\partial t}\right] A_n(z,t) = -i\mu_0\omega_0 \int da \mathbf{E}_n^* \cdot \mathbf{J}_\omega \tag{2.57}$$

where ω_{nc} is the local mode cutoff frequency, which may depend on the axial position.

Now, multiply Eq. 2.57 by A_n^* and multiply the complex conjugate of Eq. 2.57 by A_n and then add and subtract the resulting equations, and integrate the sum and the difference over the axial distance. The final expressions lead to

$$\left[A_n^*\frac{\partial A_n}{\partial z} - A_n\frac{\partial A_n^*}{\partial z}\right]\Bigg|_0^L = -i\mu_0\omega_0 \int_V dadz(A_n^*\mathbf{E}_n^* \cdot \mathbf{J}_\omega + A_n\mathbf{E}_n \cdot \mathbf{J}_\omega^*) \tag{2.58}$$

$$\frac{\partial|A_n^2|}{\partial z}\Bigg|_0^L + \int_0^L dz\left[-2\left|\frac{\partial A_n}{\partial z}\right|^2 + \frac{(\omega_0^2 - \omega_{cn}^2}{c^2}|A_n|^2 + 2i\frac{\omega_0}{c^2}\left(A_n^*\frac{\partial A_n}{\partial t} - A_n\frac{\partial A_n^*}{\partial t}\right)\right]$$

$$= -i\mu_0\omega_0 \int_V dadz(A_n^*\mathbf{E}_n^* \cdot \mathbf{J}_\omega - A_n\mathbf{E}_n \cdot \mathbf{J}_\omega^*). \tag{2.59}$$

At the cavity output, the mode amplitude function has the form of an outgoing wave with amplitude a_{nL} and wave number k_{nz}, i.e.,

$$A_n(z = L, t) = a_{nL}(t)e^{i(k_{nz}z - \psi_n(t))} \tag{2.60}$$

where ψ_n is a slowly varying mode phase parameter. The mode amplitude inside the cavity is approximated by the separable form

$$A_n(z, t) = a_n(t)e^{-i\psi_n(t)}h_n(z) \tag{2.61}$$

where $h_n(z)$ is an axial profile function which satisfies the Helmholtz equation

$$\left[\frac{d^2}{dz^2} + k_{nz}^2\right] h_n(z) = 0 \tag{2.62}$$

The mode amplitude in the cavity can be related to the mode amplitude at the cavity output via the output Q factor according to

$$a_{nL}(t) = \left(\frac{W}{k_{nz}Q_n}\right)^{1/2} \frac{\omega_0}{c} a_n(t). \tag{2.63}$$

Using Eqs. 2.60-2.63, Eq. 2.58 and Eq. 2.59 yield the free-running oscillator equations for the mode amplitude and phase as below:

$$\frac{da_n}{dt} + \frac{\omega_0 a_n}{2Q_n} = -\frac{\omega_0}{2\epsilon_0} Im\mathcal{P}_n(t) \tag{2.64}$$

$$\frac{d\psi_n}{dt} + \omega_0 = \omega_{n0} - \frac{\omega_0}{2\epsilon_0 a_n} Re\mathcal{P}_n(t) \tag{2.65}$$

where

$$\mathcal{P}_n(t) = \frac{i}{W}\int_V dadzh(z)\mathbf{E}_n^* \cdot \mathbf{J}_\omega e^{i\psi_n}$$

is the complex, slow time scale component of the electron beam polarization for the mode n,

$$W = \int_0^L dz|h(z)|^2.$$

The equations of electron motion and the equation for the RF field profile function are similarly obtained in the same manner as the single particle approximation discussed in Section 2.4. The transverse electric field components with multimodes are inserted in the equations of electron motion and the field equation.

2.6 Start-Up Scenario

The dense spectrum of modes in a cavity requires proper control of the start-up scenario. Because the beam parameters (beam voltage, beam current and velocity ratio α) change as a function of time, the mode excited in the cavity can change as a function of time as well. Current neutralization in a long pulse or in CW operation can especially influence the beam parameters, possibly resulting in an unexpected mode excitation during the beam voltage flattop.

Typically, the starting currents of possible modes in a cavity for a given beam voltage and velocity ratio evolution give a fairly reasonable determination of which mode will be excited first. The final steady state in a gyrotron cavity is usually dominated by a single mode. Therefore, the mode which is excited first is very likely the mode that will result in a stable oscillation at the final stage. The first detailed experimental verification of a mode excitation depending on the start-up scenario was done by Whaley et al., and the details can be found in [23]. They were able to change the start-up 'paths' by using a triode electron gun. By changing various start-up paths, they demonstrated that the selection of a mode during start-up was possible, and the starting current theory matched excellently to the experimental results.

2.7 Computer Code for Gyrotron Cavity Design

As discussed in the previous sections (Sections 2.4-2.6), solving the pendulum equations is not simple. The dynamics of the interaction between the electrons and the cavity RF fields must satisfy the self-consistent equations with boundary conditions given at both cavity ends. Moreover, excitations of other spurious modes, which

degrade the interaction efficiency in an overmoded cavity, are very common [24]. Therefore, taking into account the mode competition between the design mode and neighboring modes is necessary for designing an overmoded gyrotron cavity. Since the operating parameters, beam voltage, beam velocity ratio, and beam current change during pulsed gyrotron operation, the mode start-up has a time-dependence as discussed in Section 2.6. The time sequences of excitations of modes are also to be checked with a realistic voltage rise time.

MAGY is a gyrotron and gyro-klystron cavity design code that has been developed by the University of Maryland and the Naval Research Laboratory (NRL) and is widely utilized in the United States [25]. MAGY is a non-stationary, multi-frequency code that is time-dependent and self-consistent in solving the gyrotron equations. It has been successfully used in analyzing and designing gyrotron cavities and has been discussed in numerous papers [26, 27, 28, 29].

Important factors that are exhibited in real situations, such as magnetic field tapering, beam voltage profiling, voltage depression, velocity spread, energy spread, window reflections, and non-ideal conductivities in various cavity materials are included in MAGY. Typical output results give the RF axial field and phase profile inside the cavity as a function of time and power at each mode.

2.8 Gyrotron Efficiency Constraints

2.8.1 Ohmic Loss

Maxwell equations for sinusoidally varying fields are expressed by,

$$\nabla \times \mathbf{B} = i\mu_0\epsilon_0\omega\mathbf{E}$$

$$\nabla \times \mathbf{E} = i\omega\mathbf{H}.$$

where ω is the cold-cavity frequency which has a real and imaginary part,

$$\omega = \omega_r + i\frac{\omega_i}{2Q}.$$

The real part gives the mode eigenfrequency and the imaginary part accounts for losses. In gyrotrons, two losses are considered to be important. One is diffraction loss, which is a result of radiation leaking out of the cavity, and other is ohmic loss, which manifests itself as power dissipation in the cavity walls. The total quality factor, Q, is expressed as

$$\frac{1}{Q} = \frac{1}{Q_D} + \frac{1}{Q_{ohm}}$$

where Q_D and Q_{ohm} are the diffraction loss and the ohmic loss, respectively. Q_D is approximately expressed as

$$Q_D = \frac{Q_{D,min}}{1 - |R_1||R_2|}$$

where $|R_1|$ and $|R_2|$ are the reflection coefficients at the entrance and at the exit of the cavity and $Q_{D,min}$ is the minimum diffractive Q, approximately equal to,

$$Q_{D,min} \simeq 4\pi \left(\frac{L}{\lambda}\right)^2$$

which ignores the reflections of both ends. Q_{ohm} is defined by

$$Q_{ohm} P_{ohm} = \omega W$$

from the energy balance equation. In the case of rotating modes, Q_{ohm} can hence be written as,

$$Q_{ohm} = \frac{r_w}{\delta_{sk}} \left(1 - \frac{m^2}{\nu_{mp}^2}\right)$$

where r_w is the cavity wall radius, δ_{sk} is the skin depth, which is defined as

$$\delta_{sk} = \sqrt{\frac{2}{\mu_0 \omega \sigma}}.$$

Here σ is the wall conductivity equal to $5.8 \times 10^7 / \Omega m$ in SI units for pure copper. The power loss due to the ohmic loss in the cavity is now expressed as

$$P_{ohm} = \frac{Q}{Q_D} P_{out}.$$

In the case of high power gyrotrons, P_{ohm} can be further expressed in terms of the known cavity parameters

$$P_{ohm} \simeq \frac{P_{out}}{\lambda^2} \frac{L\delta_{sk}}{r_w^2(1-m^2/\nu^2)}$$

by considering $Q \simeq Q_D$.

The total efficiency that takes into account the ohmic losses is now given by

$$\eta_{total} = \frac{\eta_{el}}{1+\frac{Q}{Q_{ohm}}} \tag{2.66}$$

using,

$$\begin{aligned} \eta_{total} P_{in} &= P_{out} \\ \eta_{el} P_{in} &= P_{out} + P_{ohm}. \end{aligned}$$

Typically in high power gyrotrons, $\frac{Q}{Q_{ohm}}$ is maintained to be small enough to be ignorable. The maximum P_{ohm} is desired to be below 2.0 kW/cm^2 for CW operation due to limitations of the cooling technology.

2.8.2 Voltage Depression and Limiting Current

Voltage depression is one of the limiting factors in the operation of high power gyrotrons. It introduces changes of the resonance condition as well as the velocity ratio (α), resulting in the mirroring of the beam. In addition, the velocity spread in β_z will increase, leading to the degradation of the beam quality and reductions in efficiency. Voltage depression and limiting current in gyrotrons were first analyzed by Drobot and Kim (1981) and Ganguly and Chu (1984) [30, 31].

Let's consider a thin hollow electron beam passing through a gyrotron cavity as shown in Fig. 2-8. Here, r_c and r_b are the cavity radius and the beam radius, respectively. The potential at the cavity wall is V_c and the voltage depression between the cavity wall and the electron beam is ΔV. The electron beam is assumed to be

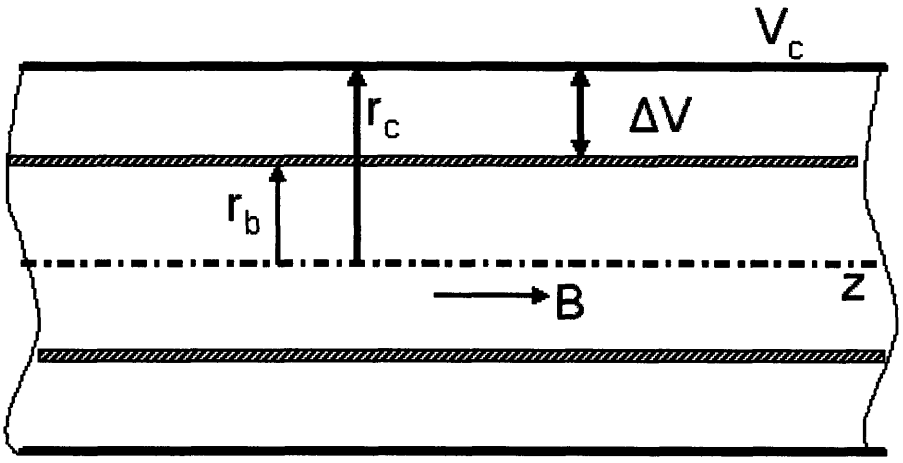

Figure 2-8: Hollow electron beam in a gyrotron cavity.

thin and monoenergetic. The voltage depression of the beam with respect to the cavity wall is expressed by the Poisson equation,

$$\Delta V = \frac{I}{2\pi\epsilon_0 v_z} \ln \frac{r_c}{r_b}. \tag{2.67}$$

One can notice that Eq. 2.67 contains v_z, which can be expressed in the nonrelativistic approximation,

$$v_z = \sqrt{2\frac{e}{m_e}(V_c - \Delta V) - v_\perp^2} \tag{2.68}$$

where $v_\perp$ does not depend on ΔV. $v_\perp$ can be expressed as

$$\begin{aligned} \alpha_0 &= \frac{v_\perp}{v_{z0}} \\ &= \frac{v_\perp}{\sqrt{2\,(e/m_e) - v_\perp^2}} \end{aligned} \tag{2.69}$$

where v_{z0} is the parallel velocity without the voltage depression. Therefore, by using Eq. 2.69, Eq. 2.68 is written as

$$v_z = \sqrt{\frac{2e}{m_e} V_c} \sqrt{\frac{1}{1+\alpha_0^2} - \delta} \tag{2.70}$$

where $\delta = \frac{\Delta V}{V_c}$ is the relativistic voltage depression. Substituting Eq. 2.70 into Eq. 2.67, one can find the current is

$$I = \frac{2\pi\epsilon_0\sqrt{\frac{2e}{m_e}}V_c^{3/2}\delta\sqrt{\frac{1}{1+\alpha_0^2}-x}}{\ln(r_c/r_b)}. \tag{2.71}$$

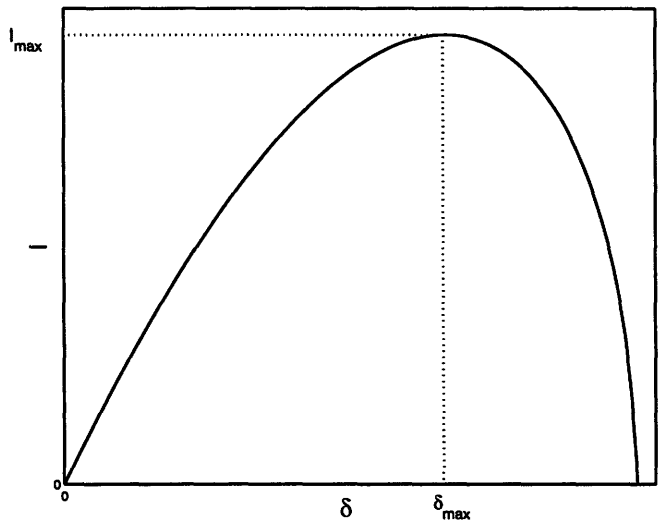

Figure 2-9: Plot of voltage depression as a function of δ.

According to Eq. 2.71, the current I initially grows with δ, and drops after it reaches the maximum. The maximum δ can be easily found from Eq. 2.71,

$$\delta_{max} = \frac{2}{3(1+\alpha_0^2)} \tag{2.72}$$

and corresponding maximum current I_{max} is

$$I_{max} \simeq \frac{0.4V_c^{3/2}}{(1+\alpha_0^2)^{3/2}\ln(r_c/r_b)} \tag{2.73}$$

here, I and V_c are in Amperes and kilovolts, respectively.

The limiting current I_L is the current beyond which the voltage depression becomes so large that $v_z \rightarrow 0$ and mirroring of the beam occurs. Therefore I_{max} corresponds to I_L.

Chapter 3

Experimental Setup and Diagnostics

3.1 Experimental Setup

3.1.1 Electron Gun

The magnetron injection gun (MIG) used in this experiment is an old diode gun from prior experiments and it was designed by Dr. Steve Korbly, a former graduate student at MIT, working with Dr. Stephen Cauffman of CPI, Palo Alto, CA. The electron gun was designed and optimized by the EGUN beam optics code [32]. The design and operating parameters of the electron gun are summarized in Table 3.1.

The cathode is a thermionic M-type dispenser cathode built by SpectraMat. The M designation refers to the standard M-type cathode commonly used in the microwave tube industry. The M-type cathode has a sintered tungsten matrix impregnated with barium oxide and lesser amounts of calcium oxide and aluminum oxide. The emitting surface has an osmium/ruthenimum film deposited on it. The M-type cathodes have the advantaged of low evaporating rates of the impregnates, low operating temperature and long life of operation. The impregnate ratio of a mixture of $BaO:CaO:Al_2O_3$ is 4:1:1 which is known to be much less susceptible to cathode poisoning than the previous 5:3:2 mixture cathode that failed to activate [33, 34].

Table 3.1: Design and operating parameters for the electron gun

Beam voltage	96 kV
Beam current	40 A
Beam alpha ($\alpha = v_\perp/v_\parallel$)	1.4
Emission current density	4 A/cm^2
Emitter angle	36°
Emitter width	0.36 cm
Cathode-anode distance	1.5 cm
Emitter radius	4.8 cm
Beam radius in cavity	1.024 cm
Beam thickness Δr_b	0.09 cm
Velocity spread ($\Delta v_\perp/v_\perp$)	2.5 %
Magnetic field compression	22.13

A typical I-V curve for the electron gun was measured in June, 2006 and is plotted in Fig. 3-1. The cathode was usually operated at 75-95 % of the gun filament rating.

3.1.2 Superconducting Magnet

The superconducting magnet for the experiment is a Cryomagnetics 7.5 T magnet previously used for a 170 GHz gyrotron experiment. This experiment is designed for a 110 GHz oscillating frequency, therefore the nominal magnetic field is 4.3 T. The field homogeneity is better than 0.7 % over 2.5 cm. The magnet has two sets of coils that charge serially with a ratio of the magnetic field to the current of 0.0976 T/A. The experiment was usually performed with the magnet in persistent mode, and the drift of the magnetic field is better than 0.004 T over 24 hours.

3.2 Diagnostics

3.2.1 Frequency Measurement

The frequencies were measured using a heterodyne receiver system that mixes the gyrotron signal with a harmonic of a tunable local oscillator (LO). A schematic of the frequency measurement system is shown in Fig. 3-2. The LO in the experiment

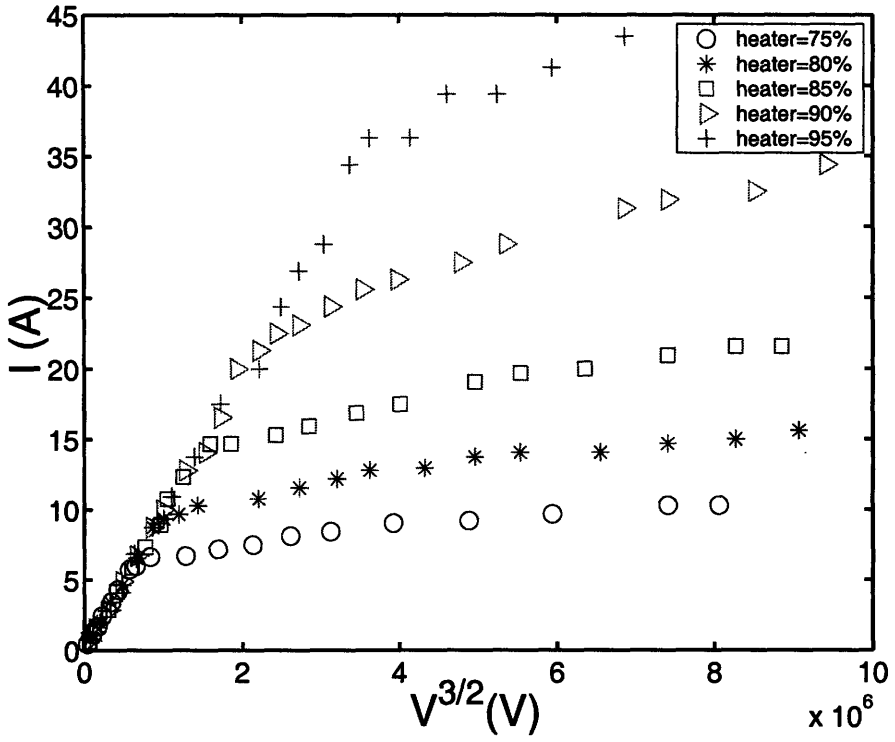

Figure 3-1: The measured I-V curve for the electron gun.

is an 8-18 GHz tunable YIG oscillator and its frequency is measured by a microwave frequency counter (EIP, Model 548) with an accuracy of a few Hz. The mixer mixes the high frequency gyrotron signal with the $n-th$ harmonic of the tunable LO. The resulting intermediate frequency (IF) signal from the harmonic mixer is amplified by a series of solid-state amplifiers and is bandlimited between 150-500 MHz by filters. The output of the IF is fast Fourier analyzed on a digital oscilloscope (LeCroy waverunner, Model LT372, Bandwidth 500 MHz, 4 GS/s) to display the sidebands.

$$f_{RF} = nf_{LO} \pm f_{IF} \tag{3.1}$$

From Eq. 3.1, f_{RF} is the unknown gyrotron frequency, f_{LO} is the local oscillator frequency multiplied by n which is the harmonic number. Since the IF is bandlimited 150-500 MHz, we chose f_{IF} to be 300 MHz. By tuning the LO frequency the upper

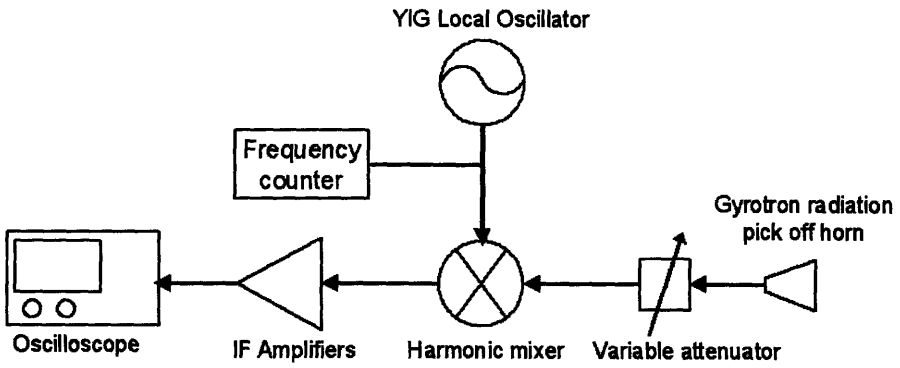

Figure 3-2: Block diagram of the frequency measurement heterodyne system.

frequency of the LO and the lower frequency of the LO can be found as shown in Eq. 3.2.

$$f_{RF} = nf_{LO,upper} - 0.3\ GHz$$
$$f_{RF} = nf_{LO,lower} + 0.3\ GHz \tag{3.2}$$

By equating the two equations for f_{RF}, the harmonic number n can be obtained and therefore using one of the equations in Eq. 3.2 the unknown gyrotron frequency f_{RF} can be found.

The heterodyne receiver system is capable of measuring very high frequencies, though the mixer signal becomes rather weak when the harmonic number increases beyond 15 to 20. The precision of the measured output frequency is ± 20 MHz due to the drifting of the local oscillator signal.

3.2.2 Power Measurement

The measurement of output power from a short pulse gyrotron at a frequency of >100 GHz is not trivial. We have adopted a technique borrowed from laser power measurement using a dry calorimeter for measuring gyrotron output power. It consists of a 20 cm diameter calorimeter plate (Scientech 378, Model No. 360801) and an

accompanying analog signal meter. The dry calorimeter surface was modified as described in [35] for better absorption at microwave frequencies. The back panel of the calorimeter has a series of thermoelectric elements attached underneath the absorbing surface that transform the temperature rise to a voltage signal. The gyrotron was typically operated at a 1 Hz repetition rate, extendable to 4 Hz. The microwave pulse shape was recorded using a broadband video detector.

A small correction for the power reflection from the calorimeter is made by measuring the absorption rate on a Vector Network Analyzer (Agilent Technologies E8363B, PNA Series Network Analyzer) at 110 GHz. The absorption at the surface of the calorimeter plate was measured to be 85 %. The surface absorption uniformity was also measured using the PNA. The absorption was measured at 9 different locations in a 4×4 cm patch of the calorimeter plate and the uniformity is ±2.1 %.

3.2.3 Velocity Ratio Measurement

One of the most important parameters for gyrotron operation is the so-called alpha (α) value, or the velocity pitch factor, in the cavity. The alpha value is defined as the ratio of perpendicular velocity to parallel velocity of the electrons. In the experiment, we measure the averaged alpha value at the entrance of the cavity, which indicates the averaged alpha value in the cavity. The velocity pitch factor of the beam ($\alpha = \langle v_\perp \rangle / \langle v_z \rangle$) was measured using a cylindrical capacitance probe located near the cavity [36]. The capacitance probe consists of two concentric cylinders, one of which is grounded and the other concentric to it to measure the voltage induced by beam current traveling through it. A schematic for the experimental setup is shown in Fig. 3-3. A macor piece is used to insulate the inner electrode from the outer electrode.

The principle of measurement is that the alpha probe directly measures the charge density per a unit length (ξ) from the voltage induced (V_p) by the electron beam as

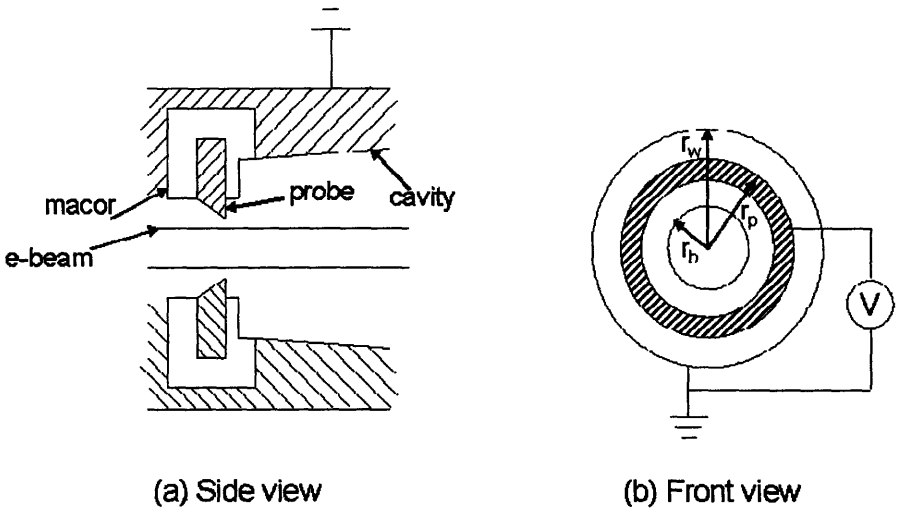

Figure 3-3: The alpha probe setup. (a) The side view: The alpha probe is located just before the cavity entrance. The cavity and the outer wall of the probe are grounded. (b) The front view: r_w, r_p, and r_b represent the wall radius, probe radius, and the beam radius, respectively.

indicated in Eq. 3.3,

$$V_p = \int_{r_w}^{r_p} E_r dr = \frac{\xi}{2\pi\epsilon} \ln\left(\frac{r_w}{r_p}\right) = \frac{\xi}{C_p}. \tag{3.3}$$

E_r and C_p stand for the radial electric field and the electrode capacitance per unit length, respectively. Therefore the averaged parallel velocity of the beam is determined with ξ and the known beam current, I_b, measured at the collector, given by Eq. 3.4,

$$\langle v_z \rangle = I_b/\xi = I_b/C_p V_p. \tag{3.4}$$

In this equation the probe capacitance is the only unknown. C_p is determined by the geometrical factors of the probe. In our experiments, however, a calibration method is used to determine the capacitance. The probe can be calibrated *in-situ* at low voltages from the assumption that the perpendicular velocity of the beam is almost negligible at low voltages and therefore $\langle \beta_z \rangle$ can be written as $\langle \beta_z \rangle = \sqrt{1 - \frac{1}{\gamma^2}}$. From Eq. 3.4 C_p can be determined.

Now the averaged perpendicular velocity of the beam can be determined from the measured v_z and the beam energy, γ and is given by,

$$\langle \beta_\perp \rangle = \sqrt{1 - \frac{1}{\gamma^2} - \langle \beta_z \rangle^2} \tag{3.5}$$

where the beam energy γ is expressed as

$$\gamma = 1 + \frac{e\,(V_b - \Delta V)}{m_0 c^2}. \tag{3.6}$$

γ has to take into account the voltage depression (ΔV) in the cavity and it is approximately expressed by Eq. 3.7 in the case of a thin annular beam.

$$\Delta V \simeq \frac{\xi}{2\pi\epsilon} \ln\left(\frac{r_w}{r_b}\right) \tag{3.7}$$

Finally, the alpha value can be obtained from Eq. 3.4 and Eq. 3.5.

The uncertainty in determining the alpha value comes mostly from the calibration of C_p and the error is estimated to be about 10 %. Nonetheless, the capacitive probe allows one to measure the alpha value of the beam very easily with a reasonably good precision. The alpha probe can also be utilized for measuring the behavior of the electron beam. For example, low frequency oscillations have been observed in the gun region due to reflected electrons, and the alpha probe serves as an antenna for picking up these oscillations. The result of the probe voltage is fast Fourier transformed in order to see the steady-state oscillations in the frequency domain. The alpha probe also indicates if the beam hits some part of the tube during operation by picking up some voltage spikes on the probe signal when it happens. If the tube itself is not properly aligned, the alpha probe also shows a slope which may be due to a nonuniform charge density (Normally the alpha probe should have a flat-top concurrent with the voltage pulse).

Chapter 4

Axial Configuration Experiment

4.1 Introduction

We present results from a 110 GHz, 1.5 MW gyrotron operating with a 3 μs pulse width in the $TE_{22,6}$ mode. The $TE_{22,6}$ mode has been successfully used in 1 MW industrial tubes [37] and in our previous studies at the 1.5 MW power level [38]. Operation at such a pulse width allows us to investigate various physics and microwave engineering issues of the design over a wider parameter space than is possible in a CW tube built by industry. The present study focuses on increasing the electronic efficiency of the gyrotron interaction by improving the cavity design. In previous research, we have reported the generation of 1.43 MW with 37 % efficiency [38]. The cavity used in those studies was also used in the industrial gyrotron and is designated the "V-2003" cavity. A new cavity, designated "V-2005," was designed to have lower ohmic losses than the V-2003 cavity by reducing the output taper angle. Results for the cavity (V-2005) are reported here and they include an increase in efficiency to 42 %. The reasons for the increase in efficiency of this low ohmic loss cavity go beyond the reduction of ohmic losses. It has been found experimentally that the new design is less susceptible to mode competition and thus allows access to the high efficiency operating regime. Theoretical modeling using a starting current simulation strongly supports the experimental results. Much of the detailed results of the axial configuration experiment are presented in [39].

Table 4.1: Nominal design parameters for the gyrotron

Frequency	110 GHz
Microwave Power	1.5 MW
Beam Voltage	96 kV
Beam Current	40 A
Beam Alpha ($\alpha = v_\perp/v_z$)	1.4
Operating Mode	$TE_{22,6}$
Pulse Length	3 μs
Cavity Magnetic Field	4.3 T

This chapter is organized as follows. In Section 4.2 we present the results of our theoretical study of gyrotron efficiency variation as a function of the basic parameters of the cavity and present the design of the V-2005 cavity. The experimental setup is described in Section 4.3 and the experimental results are presented in Section 4.4. Theoretical modeling of the startup scenario of the V-2003 and V-2005 cavities and their comparison to experiment are detailed in Section 4.5 followed by conclusions in Section 4.6.

4.2 Cavity Design Study

As the operating power approaches the MW level, the ohmic loss of the cavity wall and its dissipation become serious issues. The mean value of ohmic loss density can be expressed by Eq. 2.66,

$$\begin{aligned} P_{ohm} &= \frac{Q_D}{Q_{ohm}} \frac{P_{out}}{2\pi r_w L} \\ &\propto \frac{P_{out}}{\lambda^2} \frac{L\delta_{sk}}{r_w^2(1-m^2/\nu_{m,p}^2)} \end{aligned} \tag{4.1}$$

where, Q_D and Q_{ohm} are respectively, the diffractive and the ohmic Quality factors, P_{out} is the power exiting the cavity, L is the cavity length, λ is the wavelength, r_w is the cavity radius, m is the azimuthal index of the mode, $\nu_{m,p}$ is the eigenvalue of the

pth root of $J'_m(\nu_{m,p}) = 0$ and δ_{sk} is the skin depth which is defined as

$$\delta_{sk} = \frac{1}{2\pi}\sqrt{\frac{\lambda c}{\sigma}},$$

where σ is the conductivity of copper. From Eq. 4.1, it is evident that in order to limit the ohmic loss on the cavity wall to an acceptable value, it is advantageous to decrease the diffractive Q factor. To systematically study the optimization of the cavity, we have chosen three basic parameters of the cavity, namely, the input taper angle, the output taper angle, and the straight section length. The cavity consists of a straight section with a downtaper towards the gun and an uptaper towards the collector.

Based on the successful study of the previous cavity, V-2003, the new cavity was optimized using the multi-mode, self-consistent and time-dependent simulation code, MAGY [25]. The simulations were performed considering three coupled modes nearest to the operating mode ($TE_{21,6}$, $TE_{22,6}$, $TE_{23,6}$). The design parameters for the gyrotron are listed in Table 4.1. For a given value of the length of the straight section, the efficiency and ohmic loss can be calculated and plotted as a function of the input and output taper angles. The best results were obtained for a straight section length of 1.8 cm, the same as the length of the V-2003 cavity, and only results for that length are presented in this chapter. The simulation results from MAGY are shown in Fig. 4-1. The variation in efficiency with input and output taper angles is shown in Fig. 4-1(a). In Fig. 4-1(b), we notice that the peak ohmic heating diminishes as the uptaper angle is reduced while maintaining the same output power and efficiency.

The points for the final designs of the V-2003 and V-2005 cavities are marked as a star and cross respectively, in Fig. 4-1. The final ohmic loss design value for the V-2005 cavity is 0.8 kW/cm^2, which is reduced by 24 % compared to the V-2003 cavity while maintaining the same theoretical efficiency. The new cavity design parameters are shown in Table 4.2 and the cavity profile and axial electric field profile are shown in Fig. 4-2. For comparison, the V-2003 cavity has an uptaper of 1.2°, straight section length of 1.8 cm and a downtaper angle of 2.5°. In each case, the final cavity

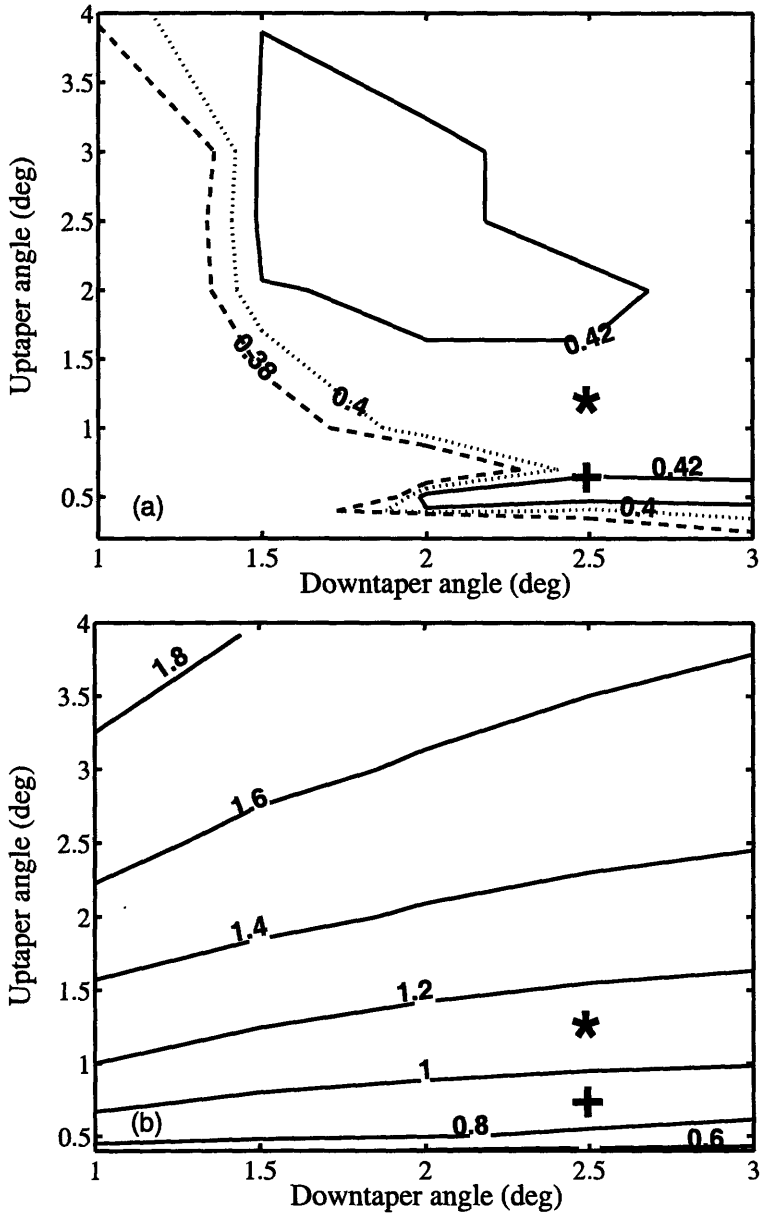

Figure 4-1: (a) Efficiency contour plot (lines) for optimization of the V-2005 cavity as a function of input and output taper angles using MAGY simulations. The cavity length is fixed at 1.8 cm. (Star: V-2003, Cross: V-2005) (b) Ohmic heating (P_{ohm}[kW/cm^2]) contour plot (lines) for optimization of the V-2005 cavity as a function of input and output taper angles using MAGY simulations. The conductivity of room temperature copper is used. (Star: V-2003, Cross: V-2005)

Table 4.2: V-2005 cavity parameters

Input taper	2.5 deg
Straight section length	1.8 cm
Output Taper	0.7 deg
Mode purity	99.78 %
Frequency	110.069 GHz
Q factor	837
Peak ohmic power	0.8 kW/cm^2
Normalized length (μ)	16.1
Power (triplet)	1.62 MW
Power (triplet, velocity spread 5 %)	1.4 MW

design included additional nonlinear output uptapers, which were designed using CASCADE [40].

Using a cold cavity simulation (without introducing the electron beam) the starting current plots for the V-2005 cavity are generated and shown in Fig. 4-3. The $TE_{22,6}$ mode has the smallest starting current among possibly excited modes in the range of the main magnetic field for an excitation of the $TE_{22,6}$ mode. The $TE_{21,6}$ and the $TE_{23,6}$ modes are excited where the main magnetic field is tuned for those modes. From the starting current curve of the $TE_{22,6}$ mode, the $TE_{19,7}$ mode is the strongest competing mode.

4.3 Experimental Setup

The 110 GHz, 1.5 MW gyrotron oscillator schematic is shown in Fig. 4-4 in the axial configuration (without an internal mode converter). A diode Magnetron Injection Gun (MIG) built by SpectraMat nominally operated at 96 kV and 40 A is used to form an electron beam of 1.0 cm radius in the cavity. A superconducting magnet is used to generate the 4.3 T field needed for operation at 110 GHz. The electron beam radius as well as the electron velocity ratio (alpha) can be fine tuned by a room temperature copper coil (referred to as the gun coil) by altering the field at the cathode to change the compression ratio. The V-2005 cavity was fabricated

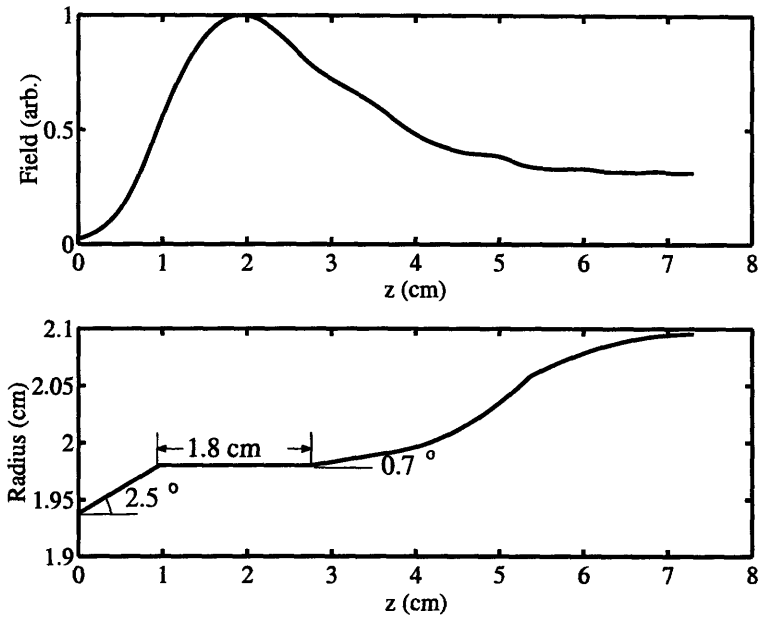

Figure 4-2: V-2005 cavity axial electric field (top) simulated by MAGY and cavity geometry profile (bottom).

by electroformation with a tolerance of better than 0.01 mm (0.4 mil) by Custom microwave, Inc., Colorado. A picture of the electroformed V-2005 cavity is shown in Fig. 4-5.

The microwave radiation generated in the cavity is brought to the 3.91 mm thick, fused quartz window through a 2.23 cm radius cylindrical waveguide which also serves as the collector for the spent electron beam. The reflection measurement of the window is done by a Vector Network Analyzer (Agilent Technologies E8363B, PNA Series Netwrok Analyzer). The result is shown in Fig. 4-6 and there is no significant reflection at 110 GHz.

4.4 Experimental Results

The V-2005 cavity was fabricated and installed in the axial configuration to verify its performance. The alignment of the gyrotron is crucial in having the right mode

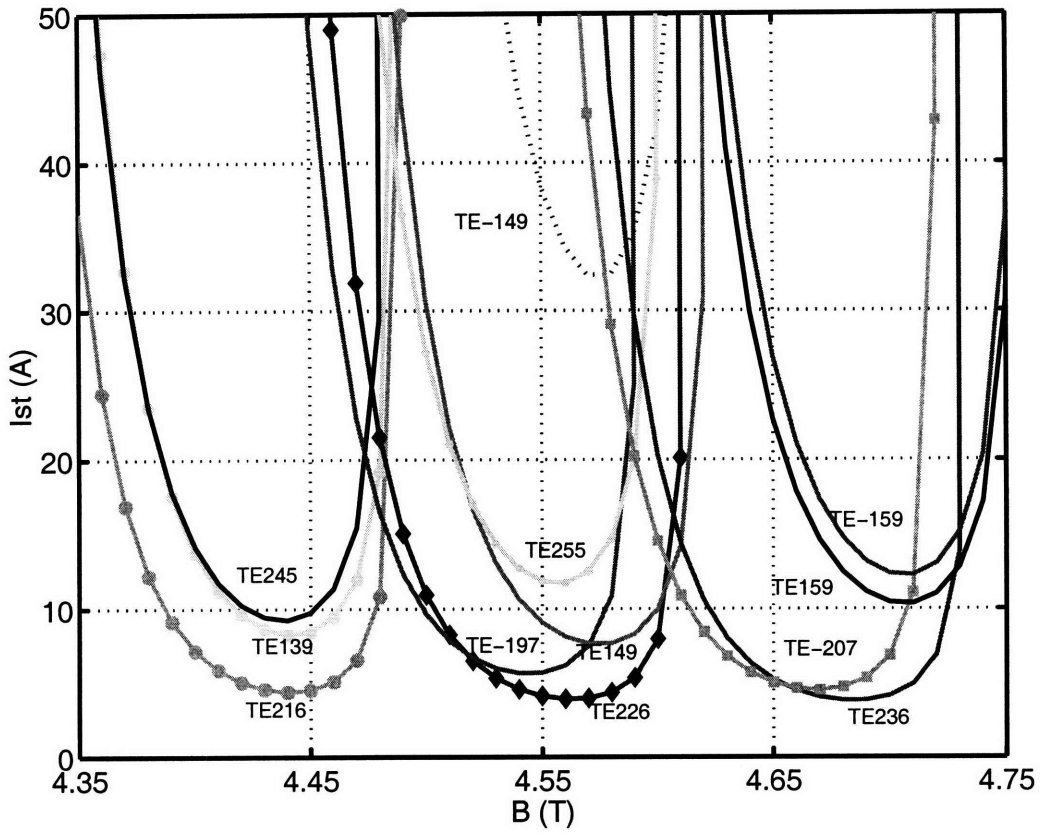

Figure 4-3: Calculated starting current curves of various modes in the V-2005 cavity. A voltage depression of 6 kV was included in the simulation.

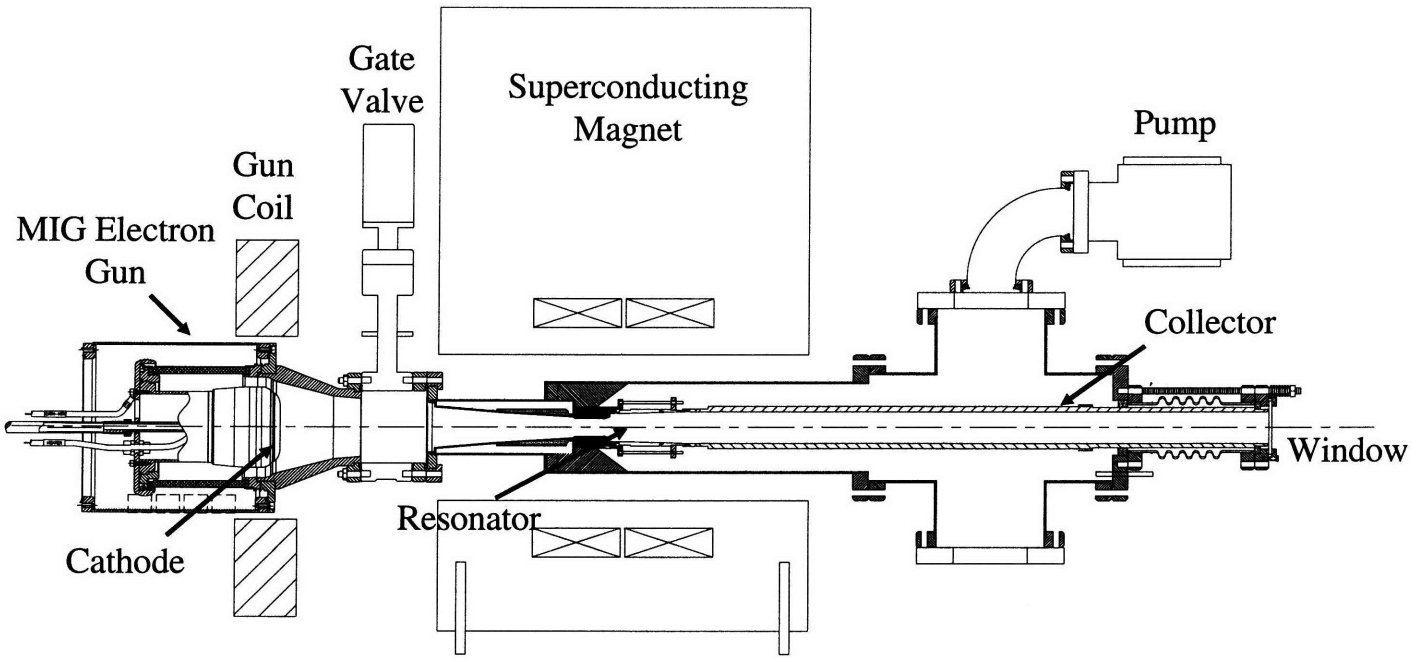

Figure 4-4: 1.5 MW, 110 GHz gyrotron experiment schematic in the axial configuration

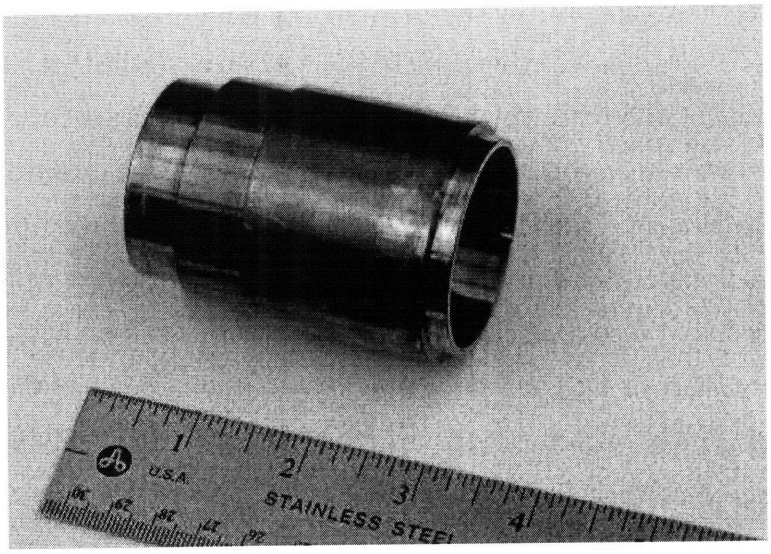

Figure 4-5: A picture of the V-2005 cavity.

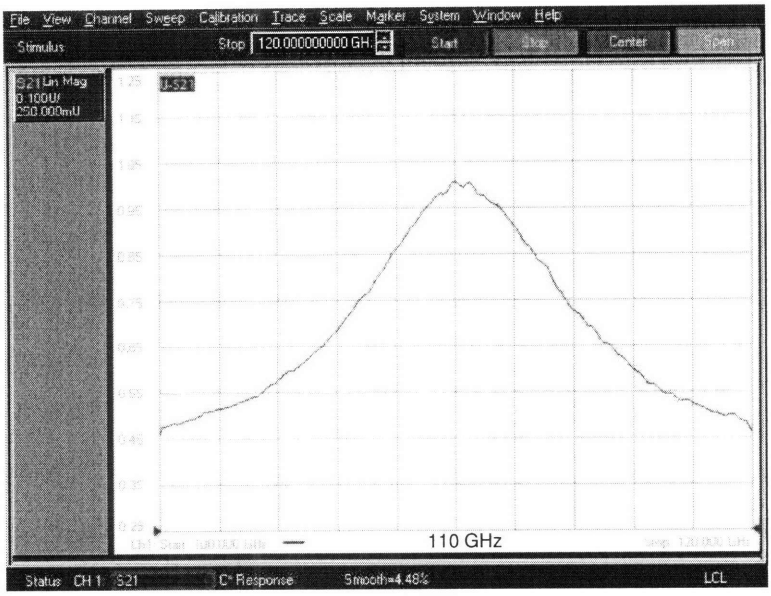

Figure 4-6: Transmission measurement of the window using a PNA.

and maximum efficiency. The gyrotron was aligned based on the measurement of the onset of body current. The electron beam passes through the beam tunnel which consists of a series of beam scrapers. The beam scrapers are made of alternating rings of copper and recessed ceralloy microwave absorber (Ceralloy 13740, 40 % SiO and 60 % BeO) whose diameter is smaller than the entrance of the cavity, therefore, when the tube is misaligned the electron beam will first hit the copper rings of the beam scraper resulting in measurable body current. The tube side and the gun side are deliberately misaligned independently at low voltage and current in the direction of x and y (assuming z is the gyrotron axis) at a fixed axial position of the tube. In each direction, the onset of body current gives the center position of the tube and the gun. The alignment accuracy is better than 0.05 mm. The procedure for the alignment of the tube continues iteratively until the center position of the gyrotron converges to one location. The final alignment for the gyrotron is by means of measuring power. The identification of the output gyrotron mode is the first step for gyrotron experiments. From identifying the modes, the operating parameters can be fine-tuned initially. The identification of modes is done by measuring the oscillation frequencies and comparing them to a chart of modes. Even though measuring frequencies is not a direct way to identify a mode, measurement of a sequence of modes and their spacing in frequency is, in fact, accurate enough to determine the design mode and satellite modes by comparison of the measured data to the calculated frequencies within good precision.

Fig. 4-7 shows the results of power measurements of various modes around the design mode, $TE_{22,6}$, as a function of main magnetic field. The power was measured by a dry calorimeter, which was discussed in Section. 3.2.2. The voltage and current were maintained near 97 kV and 40 A during these measurements. A maximum power of 1.67 MW was measured at 97 kV and 41 A in the $TE_{22,6}$ design mode. The beam velocity pitch factor was measured to be 1.35 at this point. The power at other points in Fig. 4-7 was optimized by changing the cathode magnetic field to adjust the beam radius and alpha. The maximum power measured in the $TE_{24,5}$ mode was 1.51 MW corresponding to an efficiency of 39 %. At high main magnetic fields, the

Table 4.3: Measured and calculated frequencies (cold-cavity simulation) at various modes in V-2005 cavity

Mode	f_{exp} (GHz)	f_{ccpc} (GHz)
$TE_{24,5}$	107.10	107.055
$TE_{21,6}$	107.17	107.128
$TE_{22,6}$	110.05	110.069
$TE_{20,7}$	112.65	112.630
$TE_{23,6}$	113.00	113.001

$TE_{20,7}$ and $TE_{23,6}$ modes are excited at different beam compression regimes, that is, different values of magnetic field at the cathode. The maximum power at the $TE_{20,7}$ mode is 1.33 MW. We estimate that the power measurements are accurate to ± 5 % on an absolute scale.

The frequencies of various modes were compared with the theoretical calculations performed using a cold cavity code. The results are shown in Table 4.3. The measured frequencies are in a good agreement with the calculated frequencies with a difference of ± 45 MHz.

Fig. 4-8 shows the result of power measurements as a function of beam current. The beam voltage is fixed to be 96.7 kV and the main magnetic field is also fixed at 4.541 T, which is 0.18 T higher field than the magnetic field at which the maximum power was obtained for all measurements. The alpha value decreases as the beam current increases, which agrees well with the EGUN simulation. Power increases smoothly with beam current and saturates at around 42 A due to an increase of the velocity spread at high beam currents.

To investigate the excitation regime of various modes, a mode-map was generated by varying the cathode magnetic field and the main magnetic field while holding the voltage and current fixed near 97 kV and 40 A, respectively. In the course of the generation of the mode map, both the gun magnetic field and the main magnetic field were adjusted. Lower values of the gun field at a fixed value of the main magnetic field resulted in a smaller beam radius in the cavity and higher velocity pitch factor, which eventually led to reflection of the beam towards the gun at high values of compression.

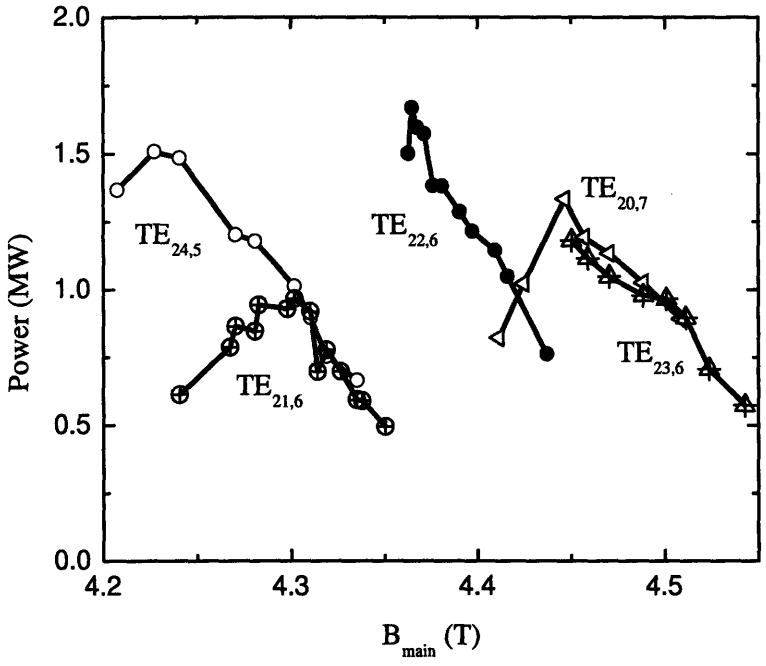

Figure 4-7: Power as a function of magnetic field at various modes in the V-2005 cavity. The beam voltage is 97 kV and the current is 40 A.

Higher values of the gun magnetic field at a fixed value of the main magnetic field result in larger beam radius and eventually led to beam interception in the tube. The mode map is shown in Fig. 4-9. From Fig. 4-9 we see a fairly wide region over which the design mode, $TE_{22,6}$ is excited. The highest efficiency point is found as expected at lower values of magnetic field. For comparison, the mode map of the V-2003 cavity was measured using the identical experimental system and methods, with the results shown in Fig. 4-10. These results are in very good agreement with our previous results for the same cavity, published in [38], as expected.

An interesting difference in the operation of the two cavities is the absence of the excitation of the counter-rotating $TE_{19,7}$ mode in the mode map of the V-2005 cavity. As seen in Fig. 4-10, for the V-2003 cavity, the $TE_{19,7}$ mode is excited near the $TE_{22,6}$ mode regime at lower values of main magnetic field and gun magnetic field. This prevents access to the high efficiency regime of the $TE_{22,6}$ design mode. In the V-2003 cavity, a series of $TE_{m,7}$ modes is excited, including a small region of the

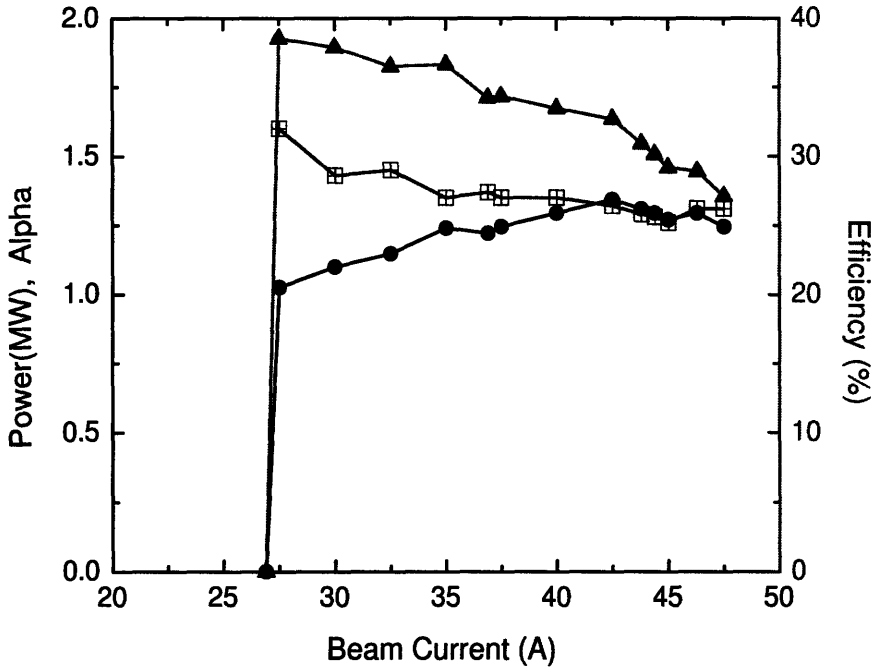

Figure 4-8: Power as a function of collector current at a fixed voltage of 96.7 kV and at a fixed magnetic field at B=4.541 T which is away from the maximum power point.

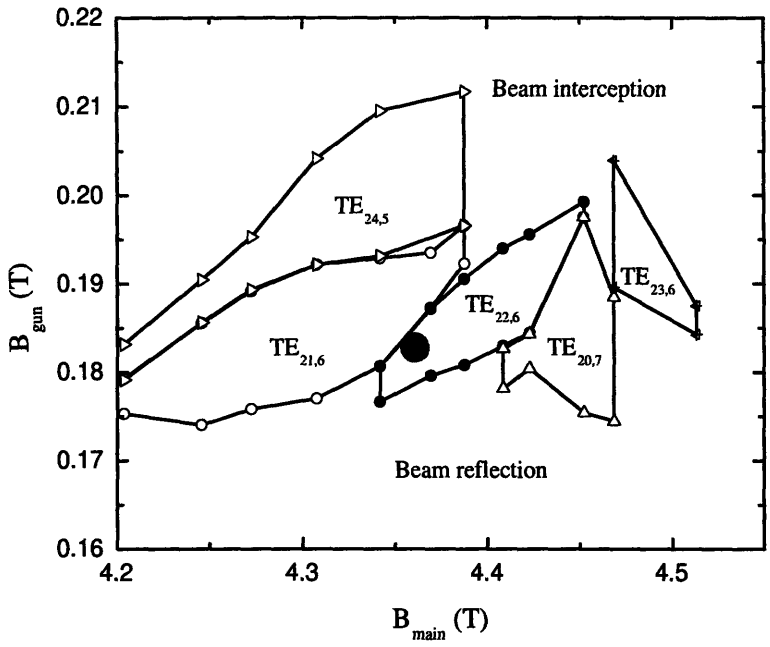

Figure 4-9: Mode map plot for the V-2005 cavity measured at 97 kV and 40 A. The circle indicates the maximum efficiency point.

$TE_{18,7}$ mode and a wide region of the $TE_{20,7}$ mode. The $TE_{m,7}$ modes are not seen in the V-2005 cavity mode map. This effect is explained in Section 4.5 by a startup scenario analysis of both the V-2005 and V-2003 cavities.

Fig. 4-11 shows a power comparison as a function of magnetic field for the V-2003 and V-2005 cavities. The highest power produced in the V-2003 cavity was 1.43 MW with an efficiency of 37 %. This result is reproducibly the same as our previous results published in [38], therefore the error bar on power measurement is very small, less than ±2 %. The highest power produced in the V-2005 cavity was 1.67 MW with an efficiency of 42 % in the $TE_{22,6}$ mode. It is evident from Fig. 4-11 that the V-2005 cavity demonstrates higher power and efficiency than the V-2003 cavity. The efficiency in the V-2005 cavity was increased from 37 % to 42 % compared to the V-2003 cavity, a major improvement.

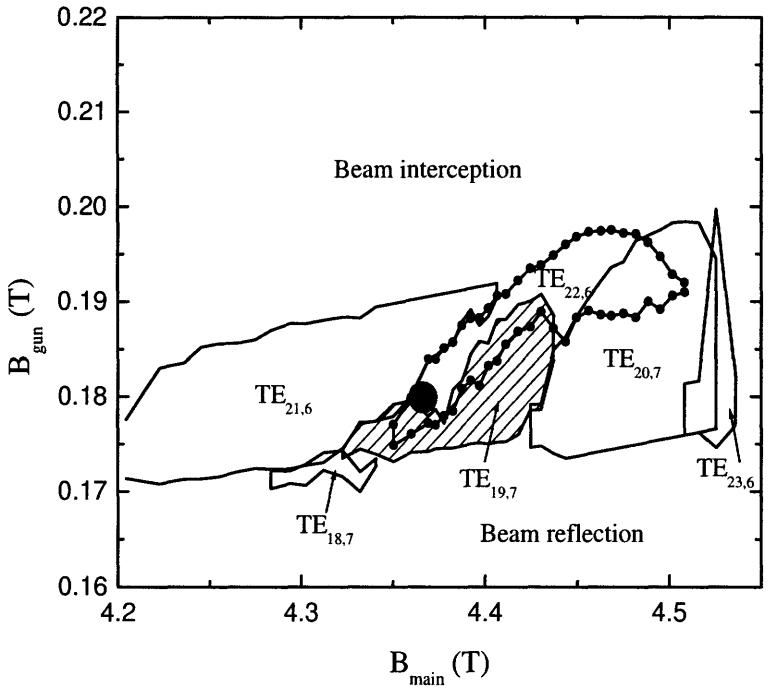

Figure 4-10: Mode map plot for the V-2003 cavity measured at 97 kV and 40 A. The $TE_{19,7}$ mode is shown hatched. The circle indicates the maximum efficiency point.

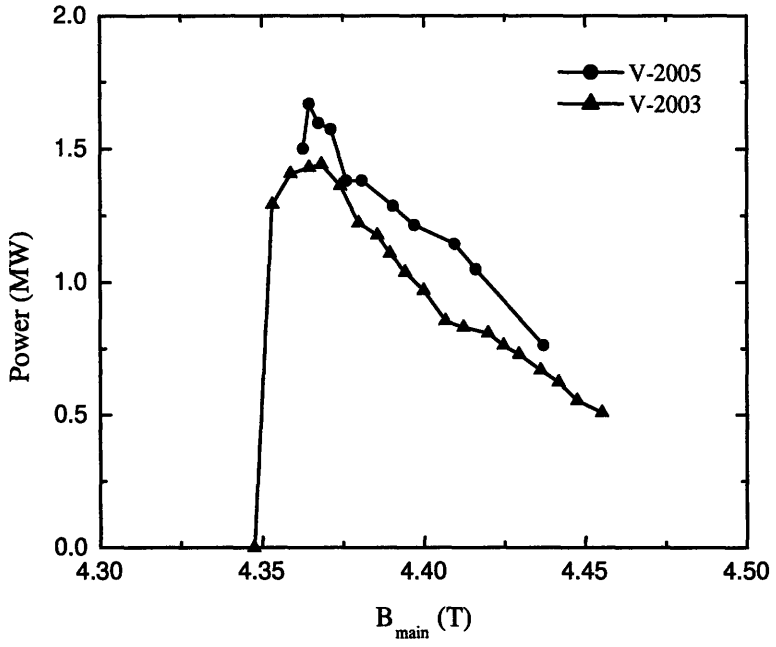

Figure 4-11: Power comparison between the V-2003 cavity (the cavity tested previously) and the V-2005 cavity as a function of the main magnetic field

4.5 Startup Scenario Analysis

A very interesting feature of the above experimental results is that a slight change in the uptaper angle between the two cavities resulted in a significant change in the mode competition. In this section we analyze the mode competition and startup scenarios of the $TE_{22,6}$ and the $TE_{19,7}$ modes in both the V-2003 and V-2005 cavities. It is well known that the sequence of the mode startup is vital in deciding the eventual dominant mode [23, 41]. By studying the relative values of start current of the two modes during the evolution of the voltage, current and alpha we can predict the eventual dominant mode. The generalized equation for the start current in an overmoded gyrotron is found in [42].

$$I_b^{st} = \frac{2\pi(mc^3\gamma_0/e)(1/\lambda)\int_0^L |f(z)|^2 dz}{[n^n/(2^{n-2}n!)]^2 Q \int W_\beta(\beta_{\perp_0})\beta_{\perp_0}^{2(s-3)}\langle\chi'' G\rangle_{r_b} d\beta_{\perp_0}} \tag{4.2}$$

where, n is the cyclotron resonance harmonic number, Q is the quality factor accounting for ohmic and diffractive losses, $\beta_{\perp_0}$ is the initial orbital electron velocity normalized to the speed of light, r_b is the electron guiding center radius, and the function $f(z)$ describes the axial structure of the resonant electric field. $G(r_b) = J^2_{m\pm s}(k_\perp r_b)/(\nu^2 - m^2)J^2_m(\nu)$ is usually defined as the coupling coefficient. Eq. 4.2 is a generalized start current equation taking into account the nonuniform magnetic field, finite radial thickness of the electron beam and velocity spread of the beam. $W_\beta(\beta_{\perp_0})$ describes the distribution function for the velocity spread defined such that

$$\int_{\beta_{\perp_0}-\Delta\beta_{\perp_0}/2}^{\beta_{\perp_0}+\Delta\beta_{\perp_0}/2} W_\beta(\beta_{\perp_0})d\beta_{\perp_0} = 1. \tag{4.3}$$

χ'' is the imaginary part of the linearized dielectric susceptibility of an electron beam defined as

$$\chi'' = -\left(n + \frac{\partial}{\partial\Delta_0}\right)\left|\int_0^{\zeta_{out}} f(\zeta)\left(i\left(\Delta_0\zeta + \int_0^\zeta \tilde{\Delta}d\zeta'\right)\right)d\zeta\right|^2 \tag{4.4}$$

where n is the harmonic number, ζ is the axial position variable defined in Eq. 2.19, ζ_{out} is the exit coordinate of the interaction space and $\Delta = \Delta_0 + \tilde{\Delta}$ is the detuning parameter defined in Eq. 2.24 with Δ_0 being constant part of Δ and $\tilde{\Delta} = (2/\beta^2_{\perp_0})(1 - B_0(\zeta)/B_0(0))$ describing the effect of magnetic field tapering. In our analysis we have assumed an ideal beam with no radial spread in guiding centers and no velocity spread. The actual measured magnetic field profile is used in the simulations. In order to simulate the start current, the electric field profile magnitudes and phases at each mode (the $TE_{22,6}$ and $TE_{19,7}$ modes) were generated using MAGY in the absence of the electron beam as shown in Fig. 4-12.

Fig. 4-13 shows the coupling coefficients of the $TE_{22,6}$ and $TE_{19,7}$ modes. The beam radius is normalized to the cavity wall radius. The $TE_{22,6}$ mode couples strongly to the electron beam for normalized beam radii values between 0.5 and 0.55. As the normalized beam radius is decreased below 0.5, the $TE_{19,7}$ mode has a stronger coupling and so it is likely that the $TE_{19,7}$ mode will be excited and will eventually dominate

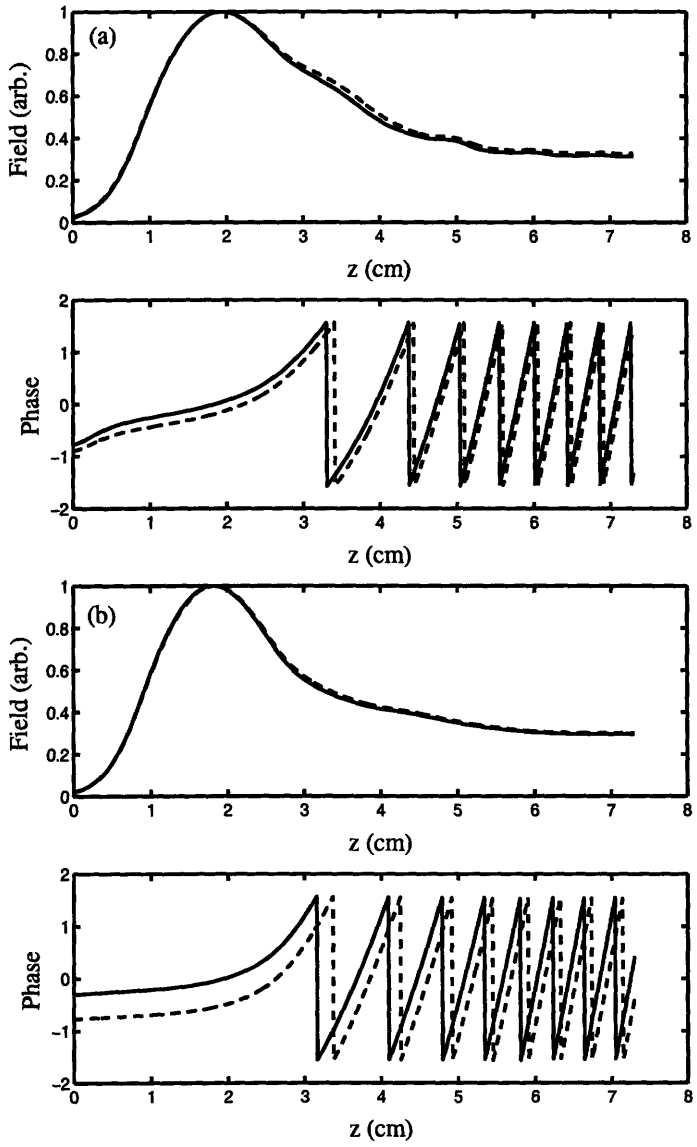

Figure 4-12: (a) Normalized field amplitude (upper) and phase profile (bottom) of cold-cavity MAGY simulation for the V-2005 cavity (solid line is the $TE_{22,6}$ mode and dashed line is the $TE_{19,7}$ mode). (b) Normalized field (upper) and phase profile (bottom) of cold-cavity MAGY simulation for the V-2003 cavity (solid line is the $TE_{22,6}$ mode and dashed line is the $TE_{19,7}$ mode)

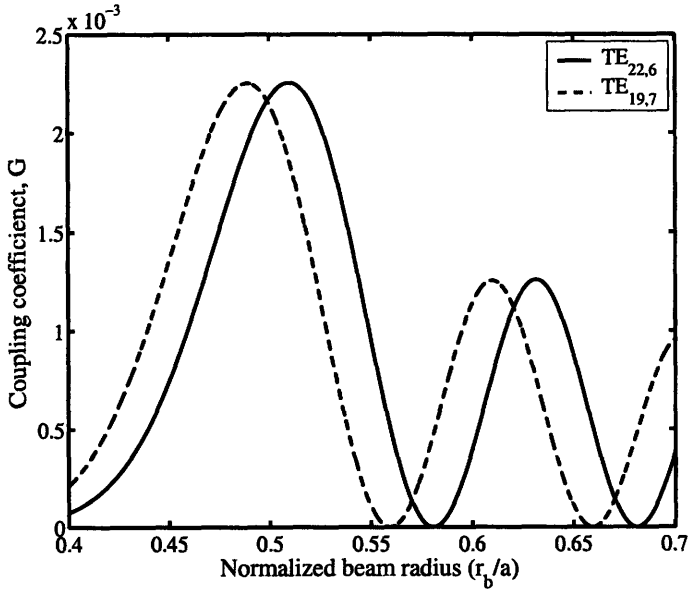

Figure 4-13: Coupling coefficient of the $TE_{22,6}$ mode and $TE_{19,7}$ mode. r_b is the beam radius and a is the cavity radius.

over the $TE_{22,6}$ design mode. From this simple coupling coefficient calculation, we can see that the beam radius can help to determine the eventual dominant mode.

Fig. 4-14 shows the start current for the $TE_{22,6}$ and $TE_{19,7}$ modes for various values of beam radius as the beam voltage, current and alpha evolve during the startup. The start current contour plots at $I_{st} = 40$ A as a function of beam alpha and beam voltage were generated for the $TE_{22,6}$ and $TE_{19,7}$ modes. The competing $TE_{22,6}$ and $TE_{19,7}$ modes are excited in the region within the solid ($TE_{22,6}$) and the dashed ($TE_{19,7}$) curves in each plot. The plot also shows the evolution of the beam velocity pitch factor α with voltage calculated using an adiabatic theory as follows:

$$\alpha = (\frac{\gamma^2 - 1}{\gamma^2 \beta_\perp^2} - 1)^{-1/2} \tag{4.5}$$

where γ is the relativistic factor and $\beta_\perp$ is perpendicular velocity normalized to the

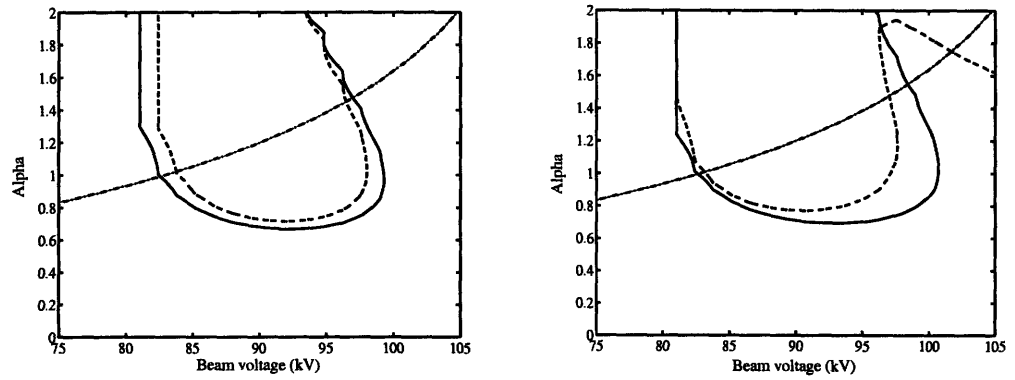

(a) $r_b = 0.52a$ (b) $r_b = 0.52a$

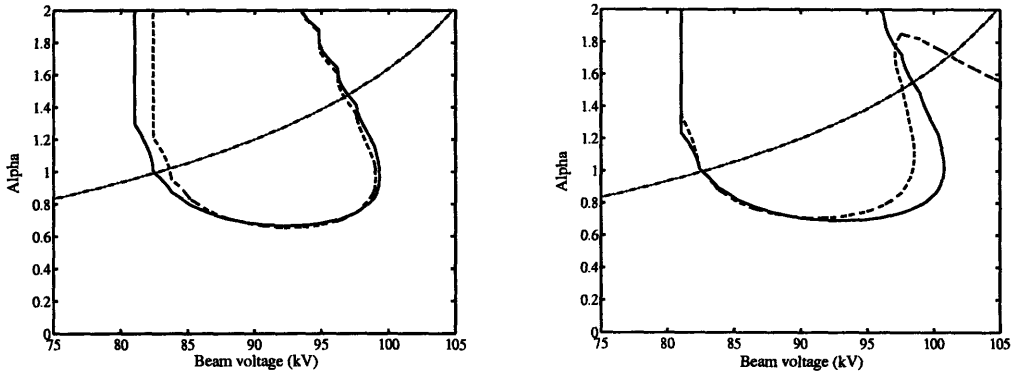

(c) $r_b = 0.505a$ (d) $r_b = 0.505a$

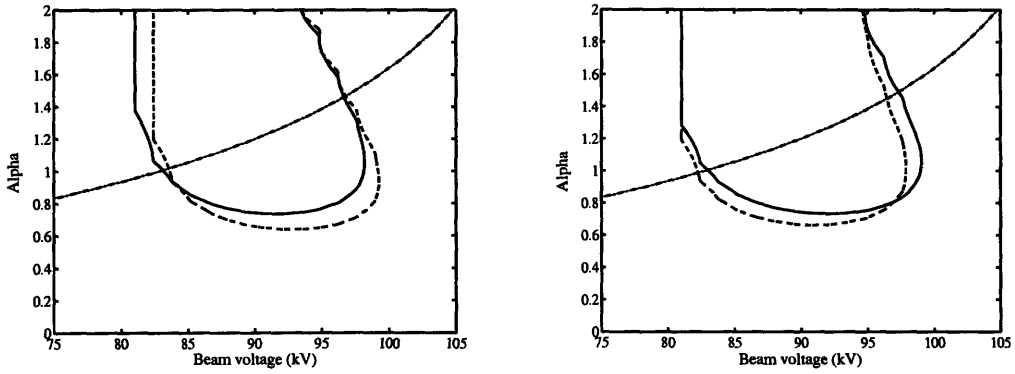

(e) $r_b = 0.48a$ (f) $r_b = 0.48a$

Figure 4-14: Iso-start current contour plot at $I_{st} = 40$ A in the alpha and beam voltage plane for different values of the beam radius. The solid line is the $TE_{22,6}$ mode, the dashed line is the $TE_{19,7}$ mode and the dash dot line is the evolution of the beam velocity pitch factor. (Electric fields and phases are obtained by MAGY simulation): (a), (c), (e) V-2005 cavity: (a) $r_b = 0.52a$, (c) $r_b = 0.505a$, (e) $r_b = 0.48a$, (b), (d), (f) V-2003 cavity: (b) $r_b = 0.52a$, (d) $r_b = 0.505a$ and (f) $r_b = 0.48a$. a is the cavity radius.

velocity of light expressed by,

$$\beta_\perp = (\frac{E_g}{cB_g})\sqrt{\frac{B_0}{B_g}}.$$

E_g and B_g are the electric and magnetic fields at the gun cathode and B_0 is the main cavity magnetic field. The adiabatic behavior of the electron gun pitch factor vs. beam voltage given in Eq. 4.5 was verified by runs of the simulation code EGUN. The plots are obtained at values of the normalized beam radius 0.52, 0.505, and 0.48. Fig. 4-14 shows the results for the V-2005 and V-2003 cavities. It is seen that the start-up path vs. beam voltage moves into the excitation region of the $TE_{22,6}$ mode first, and then the $TE_{19,7}$ mode for $r_b = 0.52a$ for both cavities. However, in the V-2003 cavity, the start current contours of the $TE_{22,6}$ mode and the $TE_{19,7}$ mode overlap each other at the beam radius $r_b = 0.505a$. In contrast the beam passes the $TE_{22,6}$ mode start current contour line first for a beam radius $r_b = 0.505a$ in the V-2005 cavity. For this cavity, even at $r_b = 0.48a$, the $TE_{22,6}$ mode wins over the $TE_{19,7}$ mode. However, in the V-2003 cavity, the $TE_{19,7}$ start current curve is excited first for $r_b = 0.48a$, which likely leads to stable $TE_{19,7}$ mode excitation. We see from Fig. 4-14 in general the margin between the excitation of the $TE_{22,6}$ and the $TE_{19,7}$ modes is smaller in the V-2003 cavity when compared to the V-2005 cavity. This can explain the easy excitation of the competing $TE_{19,7}$ mode in the V-2003 cavity, which prevents access to the high efficiency regime of the $TE_{22,6}$ mode. This start up scenario simulation strongly supports the experimental observation of different mode competition between the $TE_{22,6}$ and $TE_{19,7}$ modes in the two cavities that were investigated.

4.6 Conclusions

We have presented results for a cavity with reduced ohmic losses and have compared them to those from an earlier cavity. Higher power and efficiency were obtained using the low ohmic loss cavity when compared to the previous cavity. Since the

power measurements were made in the same experimental system with only the cavities interchanged, the measured efficiency difference may be reported with very high confidence. The primary reason for the increase in power and efficiency in the new cavity is the cavity profile, which changes the startup scenario as discussed in detail in Section 4.5. The absence of competition from the $TE_{19,7}$ mode allows access to the higher efficiency regime of the operating $TE_{22,6}$ mode. Powers up to 1.67 MW were measured at an efficiency of 42 %, which is a significant improvement over the 37 % efficiency measured with the previous cavity. The experimental results from this work suggest that a careful design of the cavity to ensure that the operating mode has a fairly wide range of excitation without competition from parasitic modes can lead to a major advantage in increasing the efficiency of the device.

The promising results from the low ohmic loss cavity experiments justify further investigation of the feasibility of using such a cavity in the 1.5 to 2 MW class of gyrotrons at 110 GHz.

Chapter 5

Internal Mode Converter

5.1 Introduction

Mode converters are essential components in modern high power gyrotrons. The mode converter converts the high order cavity mode into a simple Gaussian beam. Since the mode converter is mounted inside the gyrotron tube, it is called an "internal mode converter" (IMC). The internal mode converter consists of a launcher, which converts a cavity mode into a Gaussian-like mode, and 4 mirrors that focus and direct the Gaussian beam to the window. There is also a considerable power loss in the internal mode converter in gyrotrons. Most recent results, however, show that a well-designed mode converter will significantly reduce the possible losses in gyrotrons [43]. In this chapter, the internal quasi-optical mode converter system will be reviewed. In Section 5.2, new analytic calculations from geometrical optics and quasi-optical approximations are discussed and compared to the numerical results. The design of the mode converter as well as the experiments will be discussed in Section 5.3 and Section 5.4.

5.2 Geometrical Optics and Quasi-Optical Approximations for Radiation from a Helical Cut of a Circular Waveguide

Radiation from a helical cut of a circular waveguide is used in gyrotrons [21, 44], vacuum microwave and millimeter-wave high power sources. Gyrotrons often operate using a rotating higher order mode of a circular waveguide. To transmit the gyrotron radiation, it has to be converted into a Gaussian-like wave beam. Such an antenna-converter, also called a Vlasov antenna, has been proposed in [45]. This mode converter consists of a launcher formed as a helical cut of a circular waveguide and a cylindrical mirror. Optimized modifications of a Vlasov antenna are known [46, 47, 48, 49, 50, 51]. These modifications allow one to improve the efficiency of conversion of a rotating circular waveguide mode into a Gaussian beam.

In this section, we present a geometrical optics and quasi-optical theory of radiation from a helical cut of a waveguide. This theory is useful for designing mode converters in the millimeter wavelength range. The high power gyrotron mode converters have been designed using advanced launchers that are helical cuts of irregular circular waveguides [49]. The launchers are optimized numerically using the surface current integral equation method [52]. Nevertheless, a conventional Vlasov antenna can be used in submillimeter wave gyrotrons [53, 54]. This theory is of interest for understanding diffraction at an open end of a circular waveguide and also diffraction of a whispering gallery mode at an edge [55, 56].

5.2.1 Geometrical Optics Representation for a Waveguide Mode

In this section, we derive equations for the fields from a launcher following from the theory of [57]. For a TE waveguide mode, the Helmholtz equation for the axial

magnetic field $u = H_z$ is written in cylindrical coordinates (r, ϕ) as

$$\frac{\partial^2 u}{\partial r^2} + \frac{1}{r}\frac{\partial u}{\partial r} + \frac{1}{r^2}\frac{\partial^2 u}{\partial \varphi^2} + k_\perp^2 u = 0 \tag{5.1}$$

where $k_\perp = \sqrt{k^2 - k_z^2}$ is the transverse wave number. The solution for TE_{mn} modes is

$$u = J_m(k_\perp r)e^{-im\varphi} \tag{5.2}$$

The geometrical optics solution can be derived within the approximation $k_\perp r \gg 1$, $m \gg 1$. We represent the solution of Eq. 5.1 as $u = A(r)e^{-ik_\perp s(r,\varphi)}$, where $k_\perp$ is a large parameter. The terms with the second order of $k_\perp$ give an eikonal equation,

$$\left(\frac{\partial s}{\partial r}\right)^2 + \frac{1}{r^2}\left(\frac{\partial s}{\partial \varphi}\right)^2 = 1 \tag{5.3}$$

and the function $s(r, \varphi)$ is called "eikonal". The term with the first order of $k_\perp$ gives the transfer equation as shown below.

$$2\frac{\partial A}{\partial r}\frac{\partial s}{\partial r} + \left(\frac{\partial^2 s}{\partial r^2} + \frac{1}{r}\frac{\partial s}{\partial r} + \frac{1}{r^2}\frac{\partial^2 s}{\partial \varphi^2}\right) A = 0 \tag{5.4}$$

Assuming $s(r, \varphi) = f(r) + \frac{m\varphi}{k_\perp}$, we obtain from Eq. 5.3

$$\begin{aligned} f(r) &= \int \sqrt{1 - \frac{m^2}{k_\perp^2 r^2}}\, dr \\ &= \int \frac{1}{\sqrt{1 - \frac{m^2}{k_\perp^2 r^2}}} dr - \int \frac{\frac{m^2}{k_\perp^2 r^2}}{\sqrt{1 - \frac{m^2}{k_\perp^2 r^2}}} dr \\ &= \int \frac{r\,dr}{\sqrt{r^2 - \frac{m^2}{k_\perp^2}}} - \int \frac{\cos^2\theta}{\sin\theta}\frac{m}{k_\perp}\frac{1}{\cos^2\theta}\sin\theta\, d\theta \\ &= \sqrt{r^2 - \frac{m^2}{k_\perp^2}} - \frac{m}{k_\perp}\cos^{-1}\left(\frac{m}{k_\perp r}\right) \end{aligned}$$

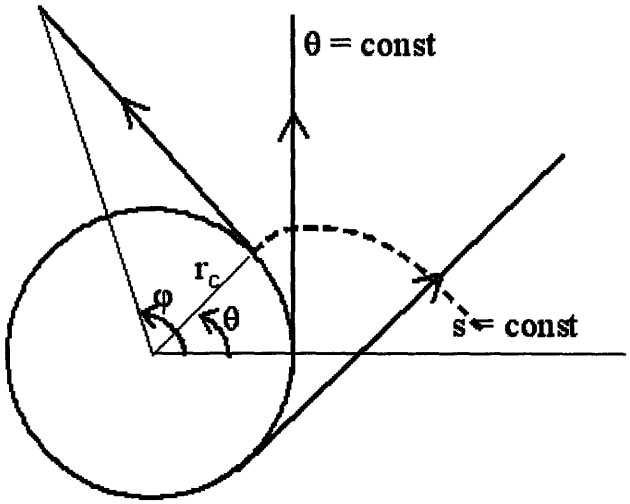

Figure 5-1: The representation of ray coordinates.

Therefore, the eikonal is

$$s(r,\varphi) = \sqrt{r^2 - \frac{m^2}{k_\perp^2}} + \frac{m}{k_\perp}\left(\varphi - \cos^{-1}(\frac{m}{k_\perp r})\right) \tag{5.5}$$

From Eq. 5.4 we obtain the amplitude,

$$A(r) = \frac{1}{\sqrt[4]{r^2 - \frac{m^2}{k_\perp^2}}} \tag{5.6}$$

The geometrical interpretation of the solution Eqs. 5.5, 5.6 is the following. There is a caustic of a radius of r_c=$\frac{m}{k_\perp}$. The rays are tangential to the caustic. The density of rays tends to go to infinity as r goes to r_c. That is why the amplitude Eq. 5.6 goes to infinity at the caustic.

The equation of a ray is,

$$\theta = \varphi - \arccos(\frac{r_c}{r}) = const. \tag{5.7}$$

Eq. 5.5 is the equation of constant phase (eikonal).

$$s(r,\varphi) = \sqrt{r^2 - \frac{m^2}{k_\perp^2}} + \frac{m}{k_\perp}\left(\varphi - \cos^{-1}(\frac{m}{k_\perp r})\right) = const. \tag{5.8}$$

The surfaces $s = const$ are the evolvents of the caustic. They are perpendicular to the rays at every point. The geometrical optics representation of Eq. 5.5 and Eq. 5.6 corresponds to the Debye approximation for the Hankel function,

$$H_m^{(2)}(k_\perp r)e^{-im\varphi} \sim \frac{1}{\sqrt[4]{r^2 - \frac{m^2}{k_\perp^2}}} exp\left(-ik_\perp\sqrt{r^2 - \frac{m^2}{k_\perp^2}} - im\left(\varphi - \arccos(\frac{m}{k_\perp r})\right) + i\frac{\pi}{4}\right). \tag{5.9}$$

The TE_{mn} mode field distribution is a superposition of the outgoing and incoming cylindrical waves:

$$\begin{aligned} J_m(k_\perp r) &= \frac{1}{2}\left(H_m^{(1)}(k_\perp r) + H_m^{(2)}(k_\perp r)\right) \\ &\sim \frac{1}{\sqrt[4]{r^2 - \frac{m^2}{k_\perp^2}}} \cos\left(k_\perp\sqrt{r^2 - \frac{m^2}{k_\perp^2}} - m\arccos\left(\frac{m}{k_\perp r}\right) - \frac{\pi}{4}\right). \end{aligned} \tag{5.10}$$

5.2.2 Quasi-Optical Representation in Ray Coordinates

In this section, diffraction will be added to the description of the geometrical optics. This is so called 'quasi-optical' representation. Diffusion of light rays occurs by edge diffraction into the region where rays do not occur in a geometrical optics calculation. It is worth representing the diffraction theory in the ray coordinates. We transform the Helmholtz equation, Eq. 5.1 to the ray coordinates s,θ. (Eqs. 5.7, 5.8)

$$
\begin{aligned}
\frac{\partial u}{\partial r} &= \frac{\partial u}{\partial s}\frac{\partial s}{\partial r} + \frac{\partial u}{\partial \theta}\frac{\partial \theta}{\partial r} \\
\frac{\partial^2 u}{\partial r^2} &= \frac{\partial^2 u}{\partial s^2}\left(\frac{\partial s}{\partial r}\right)^2 + \frac{\partial u}{\partial s}\frac{\partial^2 s}{\partial r^2} + \frac{\partial^2 u}{\partial \theta^2}\left(\frac{\partial \theta}{\partial r}\right)^2 + \frac{\partial u}{\partial \theta}\frac{\partial^2 \theta}{\partial r^2} \\
\frac{\partial u}{\partial \varphi} &= \frac{\partial u}{\partial s}\frac{\partial s}{\partial \varphi} + \frac{\partial u}{\partial \theta}\frac{\partial \theta}{\partial \varphi} \\
\frac{\partial^2 u}{\partial \varphi^2} &= \frac{\partial^2 u}{\partial s^2}\left(\frac{\partial s}{\partial \varphi}\right)^2 + \frac{\partial^2 u}{\partial \theta^2}\left(\frac{\partial \theta}{\partial \varphi}\right)^2
\end{aligned}
\tag{5.11}
$$

From Eq. 5.11, the Helmholtz equation, Eq. 5.1 is expressed in terms of ray coordinates.

$$
\begin{aligned}
&\frac{\partial^2 u}{\partial s^2}\left[\left(\frac{\partial s}{\partial r}\right)^2 + \frac{1}{r^2}\left(\frac{\partial s}{\partial \varphi}\right)^2\right] + \frac{\partial u}{\partial s}\left[\frac{\partial^2 s}{\partial r^2} + \frac{1}{r}\frac{\partial s}{\partial r}\right] \\
&\qquad + \frac{\partial^2 u}{\partial \theta^2}\left[\left(\frac{\partial \theta}{\partial r}\right)^2 + \frac{1}{r^2}\left(\frac{\partial \theta}{\partial \varphi}\right)^2\right] + \frac{\partial u}{\partial \theta}\left[\frac{\partial^2 \theta}{\partial r^2} + \frac{1}{r}\frac{\partial \theta}{\partial r}\right] + k_\perp^2 u = 0
\end{aligned}
\tag{5.12}
$$

Now using the following derivatives,

$$
\begin{aligned}
\frac{\partial s}{\partial r} &= \sqrt{1 - \frac{r_c^2}{r^2}} \\
\frac{\partial^2 s}{\partial r^2} &= \frac{r_c^2}{r^2\sqrt{r^2 - r_c^2}} \\
\frac{\partial \theta}{\partial r} &= -\frac{r_c}{r\sqrt{r^2 - r_c^2}} \\
\frac{\partial^2 \theta}{\partial r^2} &= \frac{r_c}{r^2\sqrt{r^2 - r_c^2}} + \frac{r_c}{(r^2 - r_c^2)\sqrt{r^2 - r_c^2}}
\end{aligned}
\tag{5.13}
$$

the Helmholtz equation in the ray coordinates can be expressed as below.

$$
\frac{\partial^2 u}{\partial s^2} + \frac{\partial u}{\partial s}\frac{1}{(s - r_c\theta)} + \frac{\partial^2 u}{\partial \theta^2}\frac{1}{(s - r_c\theta)^2} + \frac{\partial u}{\partial \theta}\frac{r_c}{(s - r_c\theta)^3} + k_\perp^2 u = 0 \tag{5.14}
$$

Now, we convert the Helmholtz equation in the ray coordinates (Eq. 5.14) into a parabolic equation in the ray coordinates. So as to convert it, we represent u as

$$u = A(r,\theta)e^{-ik_\perp s}.$$

assuming that $k_\perp$ is a large parameter, we drop the terms $\frac{\partial^2 A}{\partial s^2}$ and $\frac{\partial A}{\partial s}\frac{1}{(s-r_c\theta)}$ which are small compared to -$2ik_\perp\frac{\partial A}{\partial s}$ and $\frac{-ik_\perp}{(s-r_c\theta)}A$, respectively. Therefore, Eq. 5.14 can be expressed as

$$-2ik_\perp\frac{\partial A}{\partial s} - \frac{ik_\perp}{(s-r_c\theta)}A + \frac{1}{(s-r_c\theta)^2}\frac{\partial^2 A}{\partial\theta^2} + \frac{r_c}{(s-r_c\theta)^3}\frac{\partial A}{\partial\theta} = 0 \tag{5.15}$$

We introduce $X = \sqrt{\alpha}s$, $Y = \alpha(s-r_c\theta)^2$. The derivatives of A are now expressed as X and Y.

$$\begin{aligned}
\frac{\partial A}{\partial\theta} &= -\frac{\partial A}{\partial Y}2\sqrt{\alpha}r_c\sqrt{Y} \\
\frac{\partial^2 A}{\partial\theta^2} &= \frac{\partial^2 A}{\partial Y^2}4\alpha r_c^2 Y + 2r_c^2\alpha\frac{\partial A}{\partial Y} \\
\frac{\partial A}{\partial s} &= \frac{\partial A}{\partial X}\sqrt{\alpha} + \frac{\partial A}{\partial Y}\sqrt{\alpha}2\sqrt{Y}
\end{aligned} \tag{5.16}$$

Using Eq. 5.16, Eq. 5.15 is transformed to

$$-i\frac{\partial A}{\partial X} - 2i\sqrt{Y}\frac{\partial A}{\partial Y} - i\frac{1}{2\sqrt{Y}}A + 2\alpha^{3/2}r_c^2\frac{1}{k_\perp}\frac{\partial^2 A}{\partial Y^2} = 0 \tag{5.17}$$

We define α such that the coefficient of $\frac{\partial^2 A}{\partial Y^2}$ is 1.

$$\alpha = \left(\frac{k_\perp}{2r_c^2}\right)^{2/3} \tag{5.18}$$

We express A as follows,

$$A = B(X,Y)exp\left(i\frac{2}{3}Y^{3/2}\right). \tag{5.19}$$

Therefore Eq. 5.17 can be rewritten as

$$-i\frac{\partial B}{\partial X}+\frac{\partial^2 B}{\partial Y^2}+YB=0. \tag{5.20}$$

Eq. 5.20 then can be solved using separation of variables.

$$B(X,Y)=e^{-itX}D(Y) \tag{5.21}$$

$$\frac{d^2D}{dY^2}-(t-Y)D=0 \tag{5.22}$$

The solution of Eq. 5.22 is a superposition of Airy functions $Ai(t-Y)$ and $Bi(t-Y)$. The radiation field is expressed by the functions.

$$D(Y)=w_2(t-Y)=Bi(t-Y)-iAi(t-Y) \tag{5.23}$$

Going back to the coordinates θ and $l=s-r_c\theta=\sqrt{r^2-r_c^2}$, we represent the solution of Eq. 5.15 using Eqs. 5.18, 5.19, 5.21 and 5.23 as follows.

$$A=exp\left(-it\sqrt{\alpha}(l+r_c\theta)\right)\cdot w_2(t-\alpha l^2)\cdot exp\left(i\frac{2}{3}\alpha^{3/2}l^3\right) \tag{5.24}$$

A general solution of Eq. 5.15 can be constructed as a superposition of the field (Eq. 5.24) with different variables t.

Eq. 5.24 is the quasi-optical representation of fields along the ray. To compare it with the geometrical optics representation, we use the asymptotic representation for the Airy function. To derive the asymptotics we use the following equation [58]

$$\begin{aligned} w_2(-z) &= Bi(-z)-iAi(-z) \\ &= \frac{-i}{\pi}\int_0^\infty e^{i\left(\frac{p^3}{3}-zp\right)}dp+\frac{1}{\pi}\int_0^\infty e^{-\frac{p^3}{3}-zp}dp \end{aligned} \tag{5.25}$$

where the second term is small for large $z>0$. We calculate the asymptotics of the

first integral in Eq. 5.25 using the method of stationary phase. The phase function is

$$\phi(p) = \frac{p^3}{3} - pz.$$

The stationary point is determined by the equation

$$\frac{d\phi}{dp} = 0.$$

Therefore, the stationary function is represented as $p_{st} = \sqrt{z}$. The phase function is represented as

$$\phi(p) = \phi(p_{st}) + \frac{1}{2}\frac{d^2\phi}{dp^2}|_{p_{st}}(p - p_{st})^2 = -\frac{2}{3}z^{3/2} + \sqrt{z}(p - \sqrt{z})^2.$$

The integral in Eq. 5.25 can be written as

$$w_2(-z) \sim -\frac{i}{\pi} exp\left(-i\frac{2}{3}z^{3/2}\right) \int_0^\infty exp\left(i\sqrt{z}(p - \sqrt{z})^2\right) dp. \tag{5.26}$$

Assuming that the stationary point $\sqrt{z}$ is far from the integration limit $p = 0$, we can integrate from $-\infty$ to ∞. The result of the integration is

$$w_2(-z) \sim \frac{1}{\sqrt{\pi}} z^{-1/4} exp\left(-i\frac{2}{3}z^{3/2} - i\frac{\pi}{4}\right) \tag{5.27}$$

Using Eq. 5.27 we derive the asymptotics of Eq. 5.23, assuming $\left|\frac{t}{Y}\right| \ll 1$.

$$w_2(t - Y) \sim \frac{1}{\sqrt{\pi}} Y^{-1/4} exp\left(-i\frac{2}{3}Y^{3/2} + it\sqrt{Y} - i\frac{1}{4}\frac{t^2}{\sqrt{Y}} - i\frac{\pi}{4}\right) \tag{5.28}$$

Therefore, the asymptotic representation for Eq. 5.24 assuming $|\alpha l^2 - t| \gg 1$ is the following.

$$A_{asymp} = \frac{1}{\sqrt{\pi}} \alpha^{-1/4} l^{-1/2} exp\left(-it\sqrt{\alpha} r_c \theta - i\frac{t^2}{4\sqrt{\alpha l}} - i\frac{\pi}{4}\right) \tag{5.29}$$

This asymptotic solution is still the quasi-optical approximation. The term $exp\left(-i\frac{t^2}{4\sqrt{\alpha l}}\right)$ is responsible for diffraction across the rays. However, for the example we will discuss

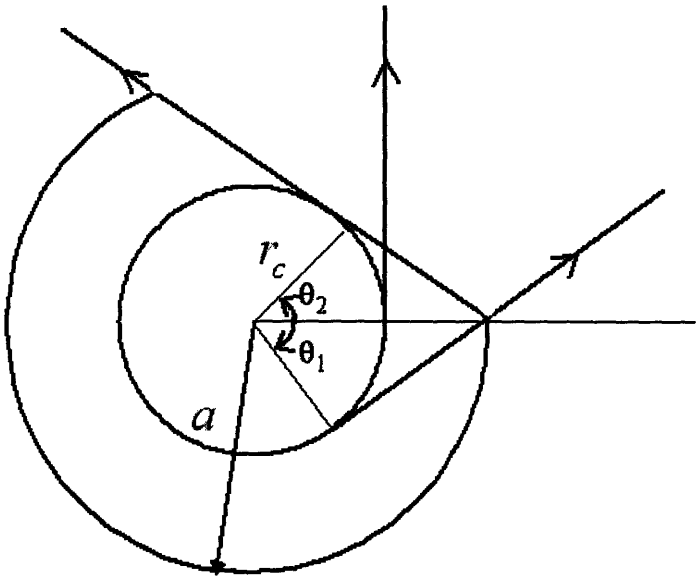

Figure 5-2: The representation of rays at the launcher tip where r_c is the caustic radius ($r_c = m/k_\perp$), a is the waveguide radius, $\theta_1 = -\arccos\left(\frac{r_c}{a}\right)$, and $\theta_2 = -\theta_1$.

this term is negligible. If we drop this term we end up with the geometrical optics expression for the field.

Now, we apply the rigorous solution in the ray coordinates Eq. 5.24 and the asymptotic solution Eq. 5.29 to describe the radiation from the launcher.

The radiation is in the interval of angles $\theta_1 < \theta < \theta_2$, where $\theta_1 = -\arccos\left(\frac{r_c}{a}\right)$ and $\theta_2 = \arccos\left(\frac{r_c}{a}\right)$, respectively, at $l = l_0 = \sqrt{a^2 - r_c^2}$, the field is uniform within the interval $\theta_1 < \theta < \theta_2$. We represent this field as a superposition of azimuthal harmonics,

$$A_0(\theta) = \sum_{n=-\infty}^{n=\infty} C_n e^{-in\theta}. \tag{5.30}$$

The coefficients can be determined as follows.

$$\begin{aligned} C_n &= \frac{1}{2\pi}\int_0^{2\pi} A_0(\theta) e^{in\theta} \\ &= \frac{1}{2\pi}\int_{\theta_1}^{\theta_2} e^{in\theta} d\theta = \frac{1}{2\pi}\frac{e^{in\theta_2} - e^{in\theta_1}}{in} \end{aligned} \tag{5.31}$$

for $n \neq 0$ and $C_0 = \frac{\theta_2 - \theta_1}{2\pi}$. The radiated field, therefore, can be written as

$$A = \sum_{n=-N}^{n=N} C_n e^{-in\theta} e^{-i\frac{n}{r_c}(l-l_0)} \frac{w_2\left(\frac{n}{\sqrt{\alpha} r_c} - \alpha l^2\right)}{w_2\left(\frac{n}{\sqrt{\alpha} r_c} - \alpha l_0^2\right)} \cdot exp\left(i\frac{2}{3}\alpha^{3/2}(l^3 - l_0^3)\right) \tag{5.32}$$

This is called the quasi-optical representation. The asymptotic equation for the radiated field is now written as,

$$A_{asymp} = \sum_{n=-N}^{n=N} \sqrt{\frac{l_0}{l}} C_n e^{-in\theta} exp\left(-i\frac{1}{4}\frac{n^2}{\alpha^{3/2} r_c^2}\left(\frac{1}{l} - \frac{1}{l_0}\right)\right) \tag{5.33}$$

This is called the geometrical optics approximation. Eq. 5.33 allows us to estimate the Fresnel parameter. At the aperture, the phase varies from 0 to $n\theta_2$, where $\theta_2 = \arctan\left(\frac{l_0}{r_c}\right)$. Let us assume

$$n\theta_2 \sim \pi. \tag{5.34}$$

If the phase in the second term varies by the same amount, diffraction occurs, therefore,

$$\frac{n^2}{4\alpha^{3/2} r_c^2}\left(\frac{1}{l} - \frac{1}{l_0}\right) \sim \pi \tag{5.35}$$

From these two equations (Eqs. 5.34, 5.35) and using Eq. 5.18 we obtain

$$\frac{4\theta_2^2}{\lambda}\frac{l l_0}{l - l_0} \sim 1$$

Introducing the aperture size $\sigma = l_0\theta_2$, we obtain the criterion of diffraction

$$N_F = \frac{4\sigma^2}{\lambda}\left(\frac{1}{l - l_0} + \frac{1}{l_0}\right) \sim 1,$$

where N_F is a generalized Fresnel parameter. $N_F \gg 1$ is the region of geometrical optics, $N_F \sim 1$ is the diffraction zone (or Fresnel zone).

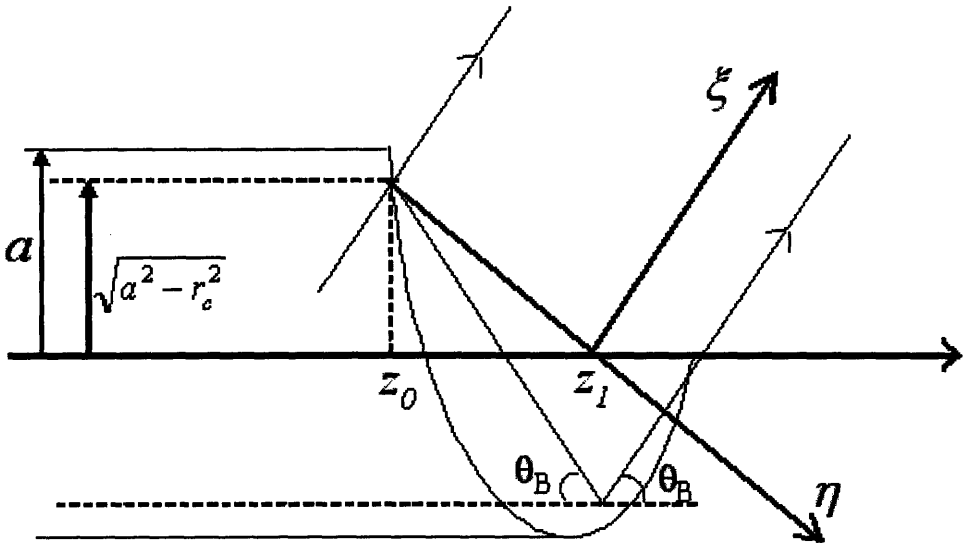

Figure 5-3: Ray propagation in the axial plane at the launcher tip.

5.2.3 Diffraction in Axial Plane

In the previous section, we have considered the radiation from the launcher in the azimuthal plane. In this section, we consider the axial plane where the geometry of the problem is shown in Fig. 5-3.

The radiation is coming out at the bounce angle $\theta_B = \arcsin\left(\frac{\nu}{ka}\right)$, where ν is the root of the equation $J'_m(\nu) = 0$. We introduce the coordinates (ξ, η), where ξ is in the direction of propagation and η is in the plane of the phase front.

$$\xi = (z - z_1)\cos\theta_B + y\sin\theta_B$$
$$\eta = (z - z_1)\sin\theta_B - y\cos\theta_B$$

z_1 is the coordinate at which the phase front intersects the z-axis,

$$z_1 = z_0 + \sqrt{a^2 - r_c^2}\tan\theta_B$$

The radiation field is described by the Helmholtz equation, Eq. 5.36,

$$\frac{\partial^2 u}{\partial \xi^2} + \frac{\partial^2 u}{\partial \eta^2} + k^2 u = 0 \tag{5.36}$$

which we represent in the quasi-optical approximation $u = Ae^{-ik\xi}$.

$$-2ik\frac{\partial A}{\partial \xi} + \frac{\partial^2 A}{\partial \eta^2} = 0 \tag{5.37}$$

The parabolic equation Eq. 5.37 has the solution.

$$A(\xi, \eta) = \int_{-\infty}^{\infty} A_0(\xi') G(\xi, \eta - \eta') d\eta' \tag{5.38}$$

where,

$$G(\xi, \eta - \eta') = \frac{C}{\sqrt{\xi}} exp\left(-i\frac{k(\eta - \eta')^2}{2\xi}\right) \tag{5.39}$$

is a Green's function. $A_0(\eta) = A(0, \eta)$ is the complex amplitude at the plane $\xi = 0$. The constant C can be determined from the condition,

$$\lim_{\xi \longrightarrow 0} G(\xi, \eta - \eta') = \delta(\eta, \eta').$$

Therefore,

$$\frac{C}{\sqrt{\xi}} \int_{-\infty}^{\infty} exp\left(-i\frac{k\eta^2}{2\xi}\right) d\eta = \frac{C}{\sqrt{\xi}} \left(\frac{\pi}{i\frac{k}{2\xi}}\right)^{1/2} = 1$$

and $C = \sqrt{\frac{ik}{2\pi}}$. We assume $A_0(\eta) = 1$ in the interval $\eta_1 < \eta < \eta_2$, where

$$\eta_1 = -\frac{\sqrt{a^2 - r_c^2}}{\sin\theta_B}$$

and,

$$\eta_2 = -\frac{\sqrt{a^2 - r_c^2}}{\cos\theta_B} + 4\sqrt{a^2 - r_c^2}\cos\theta_B.$$

From Eq. 5.38 and Eq. 5.39 we obtain

$$\begin{aligned} A(\xi,\eta) &= \sqrt{\frac{ik}{2\pi\xi}}\int_{\eta_1}^{\eta_2} exp\left(-i\frac{k(\eta-\eta')^2}{2\xi}\right)d\eta' \\ &= \sqrt{\frac{ik}{2\pi\xi}}\int_{\eta_1-\eta}^{\eta_2-\eta} exp\left(-i\frac{k\eta'^2}{2\xi}\right)d\eta' \\ &= \sqrt{\frac{ik}{2\pi\xi}}\sqrt{\frac{2\xi}{k}}\int_{\sqrt{\frac{k}{2\xi}}(\eta_1-\eta)}^{\sqrt{\frac{k}{2\xi}}(\eta_2-\eta)} exp\left(-it^2\right)dt \\ &= F\left(\sqrt{\frac{k}{2\xi}}(\eta_2-\eta)\right) - F\left(\sqrt{\frac{k}{2\xi}}(\eta_1-\eta)\right), \end{aligned} \tag{5.40}$$

where the Fresnel integral is expressed as,

$$F(x) = \sqrt{\frac{i}{\pi}}\int_{-\infty}^{x} e^{-it^2}dt. \tag{5.41}$$

5.2.4 Example of Calculation of the Launcher

We employ the Surf3D code to propagate the radiation from the launcher to the cylinder that is shown in Fig. 5-4, in (x_1, y_1) coordinates. Note that the Surf3D code is described in Section 5.3.2. The axis of the cylinder is at the caustic. The launcher radius is $a = 2.1966$ cm. The caustic radius for the mode $TE_{22,6}$ is $r_c = \frac{m}{\nu}a = 1.059\ cm$. And the mode wave number is $k = 23\ cm^{-1}$ at $f = 110\ GHz$. The transverse wave number is $k_\perp = \frac{\nu}{a} = 20.77\ cm^{-1}$. Therefore, the angle θ varies from $\theta_1 = -\arccos\frac{r_c}{a} = -1.067\ rad = -61.2°$ to $\theta_2 = 1.067\ rad = 61.2°$. The parameter $\alpha = \left(\frac{k_\perp}{2r_c^2}\right)^{2/3} = 4.409\ cm^{-2}$.

In Eq.5.32, we consider l and θ as functions of r_1 and φ_1.

$$l = \sqrt{r_1^2 - 2r_1 r_c \sin\varphi_1} \tag{5.42}$$

$$\theta = \arccos\left(-\frac{r_1\sin\varphi_1 - r_c}{\sqrt{l^2+r_c^2}}\right) - \arccos\left(\frac{r_c}{\sqrt{l^2+r_c^2}}\right) \tag{5.43}$$

The calculations have been carried out for r_1=3.3, 4, and 10 cm. Distributions of both amplitude and phase were calculated using Surf3D and have been compared to

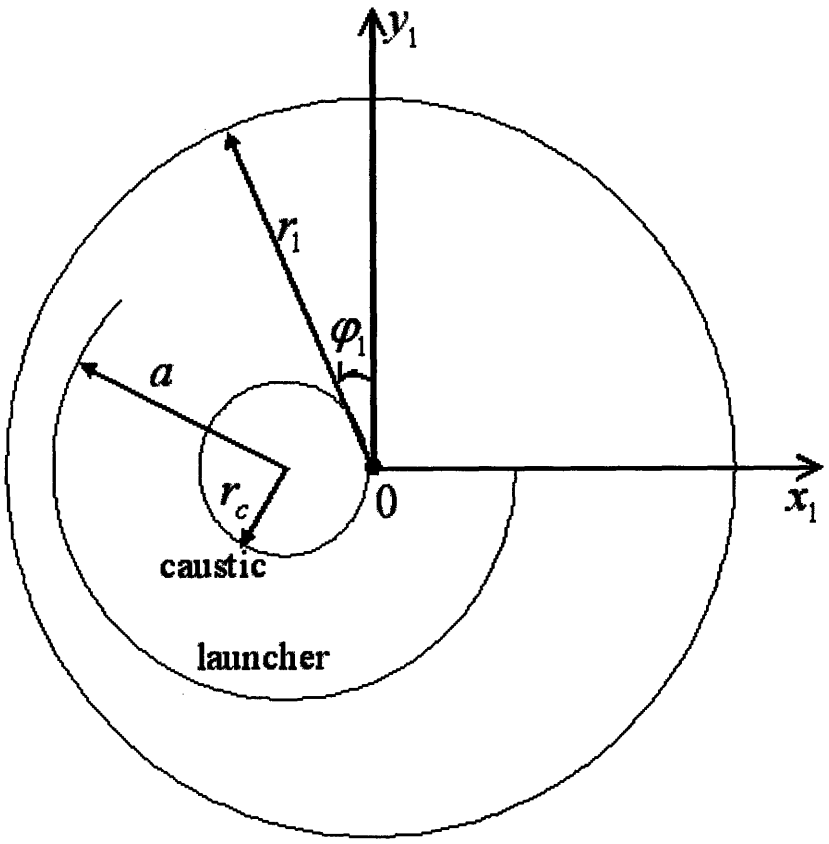

Figure 5-4: Coordinate of the radiation pattern.

the calculation from equation Eq. 5.32. The number of azimuthal harmonics, N, was chosen to be 18 in the calculation. Fig. 5-5 through Fig. 5-10 show the comparison between the Surf3D simulation and analytic solution at the measurement cylindrical plane of radius of 3.3, 4, and 10 cm. In figures, amplitudes are normalized to a maximum value of unity and phases are absolute values. As seen in the figures, the results are in good agreement.

5.2.5 Discussion of Example Results

We have calculated the radiation from a helical cut of a circular waveguide. The amplitude and phase distributions are calculated at several cylindrical surfaces. We have

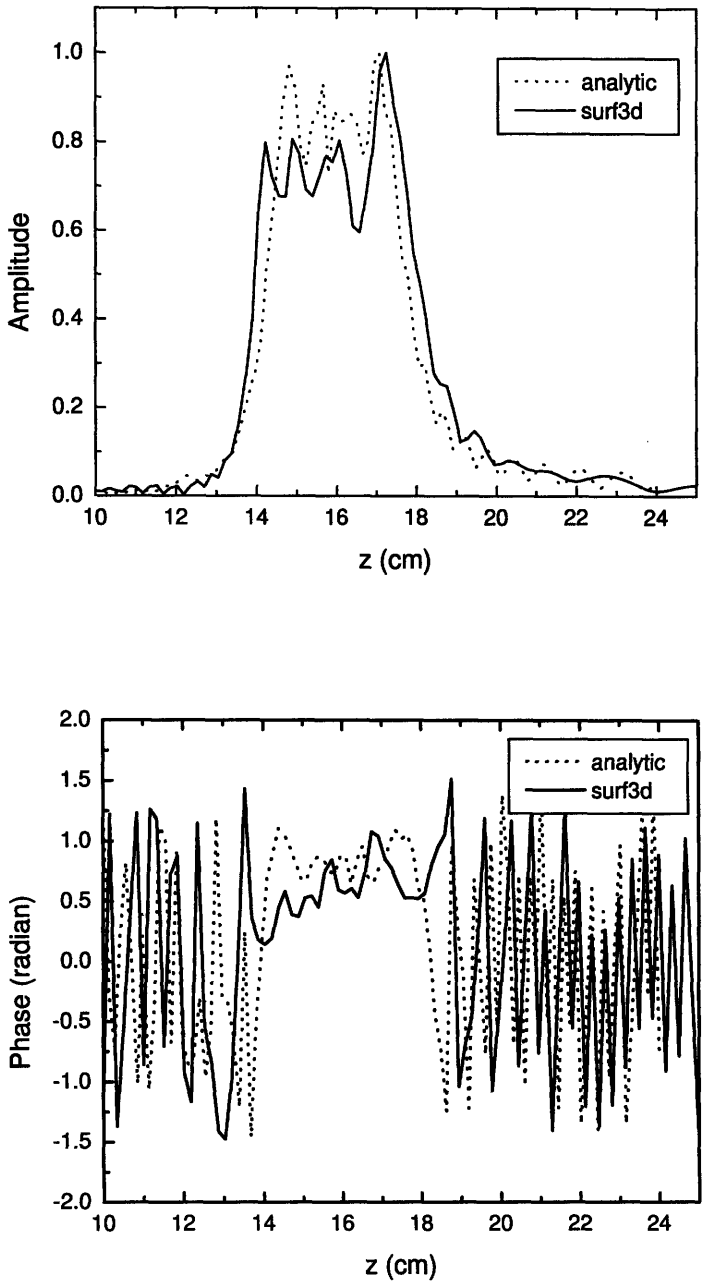

Figure 5-5: (a) Amplitude along z at radius of cylinder 3.3 cm. (solid: Surf3D, dot: analytic) (b) Phase along z at radius of cylinder 3.3 cm. (solid: Surf3D, dot: analytic)

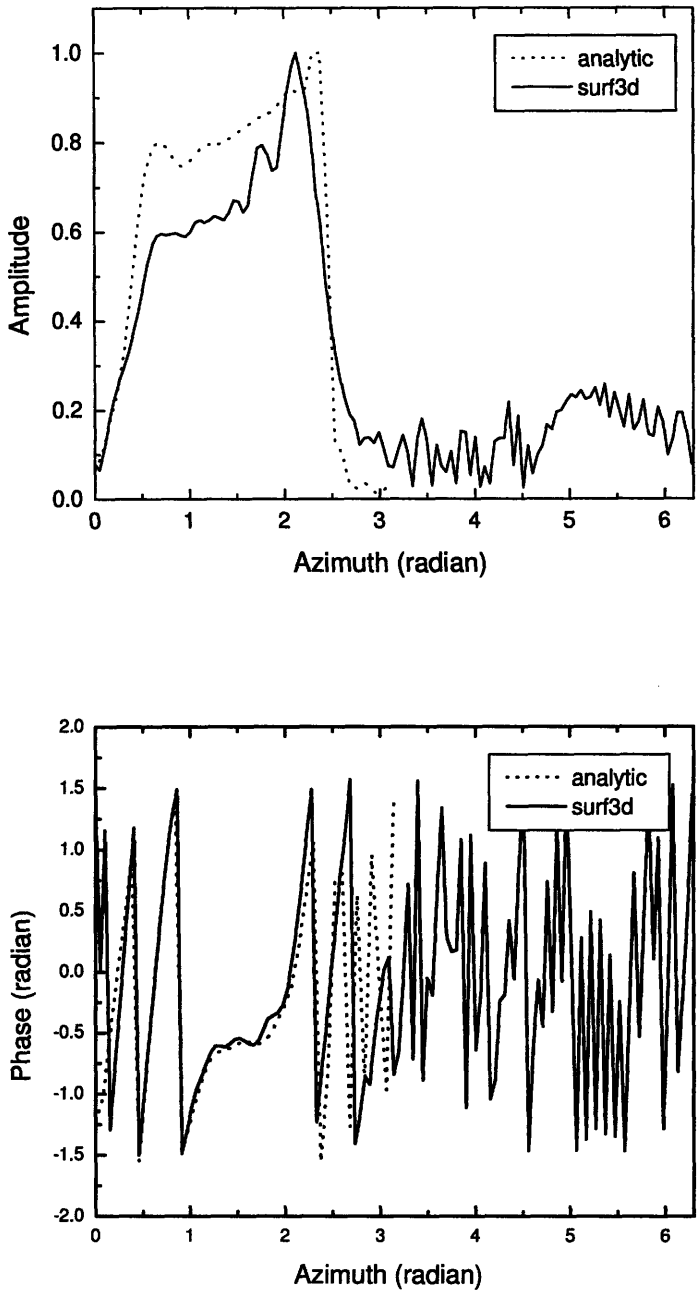

Figure 5-6: (a) Amplitude along azimuth ϕ at radius of cylinder 3.3 cm. (solid: Surf3D, dot: analytic) (b) Phase along ϕ at radius of cylinder 3.3 cm. (solid: Surf3D, dot: analytic)

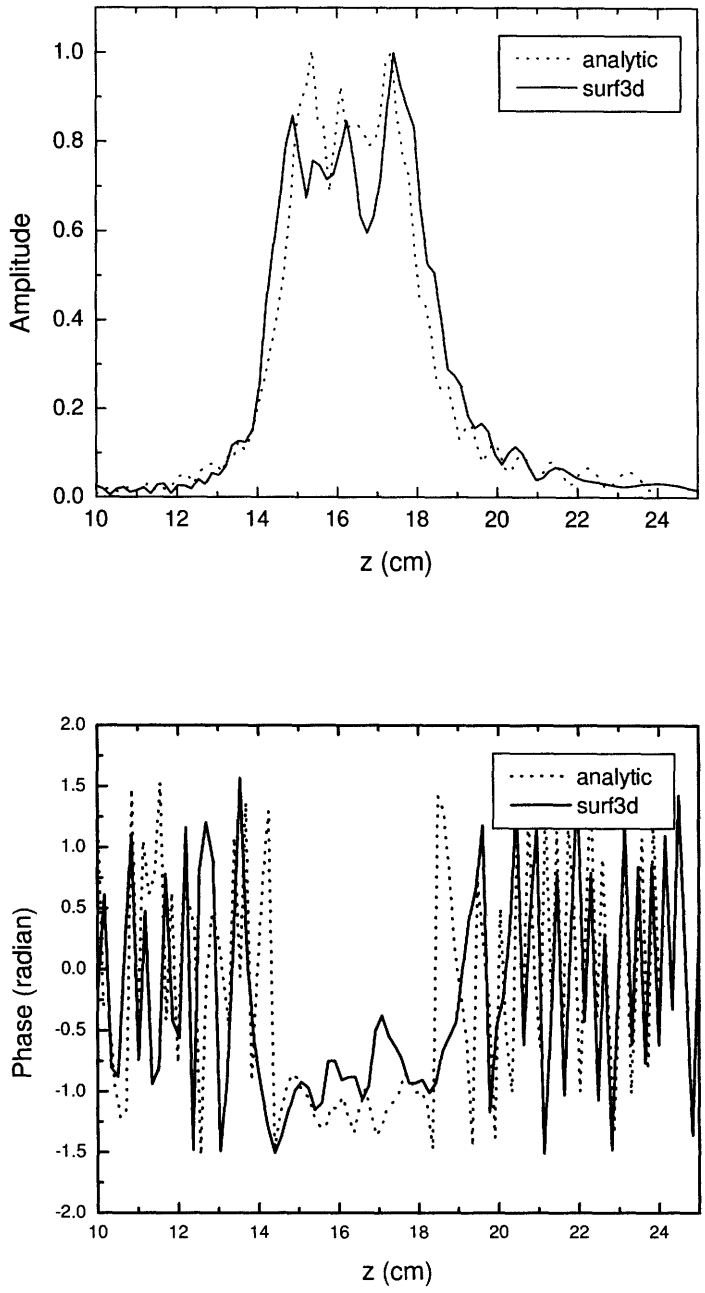

Figure 5-7: (a) Amplitude along z at radius of cylinder 4 cm. (solid: Surf3D, dot: analytic) (b) Phase along z at radius of cylinder 4 cm. (solid: Surf3D, dot: analytic)

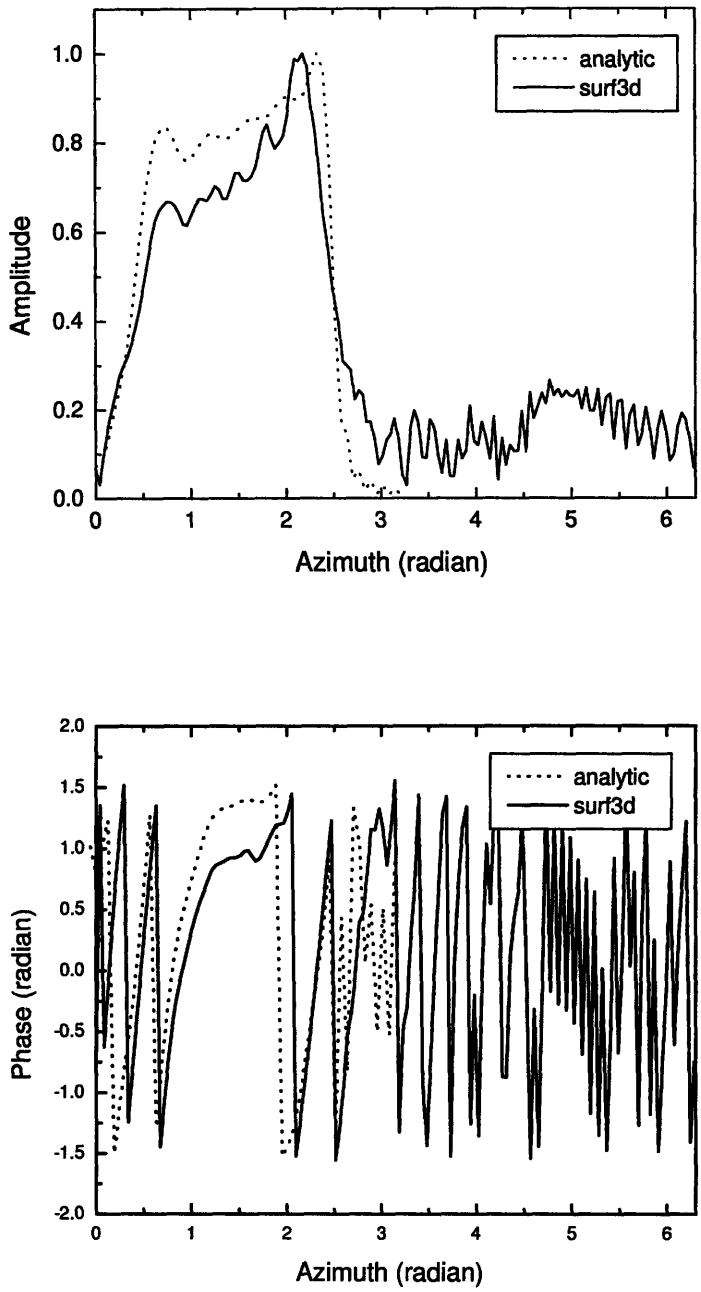

Figure 5-8: (a) Amplitude along azimuth ϕ at radius of cylinder 4 cm. (solid: Surf3D, dot: analytic) (b) Phase along ϕ at radius of cylinder 4 cm. (solid: Surf3D, dot: analytic)

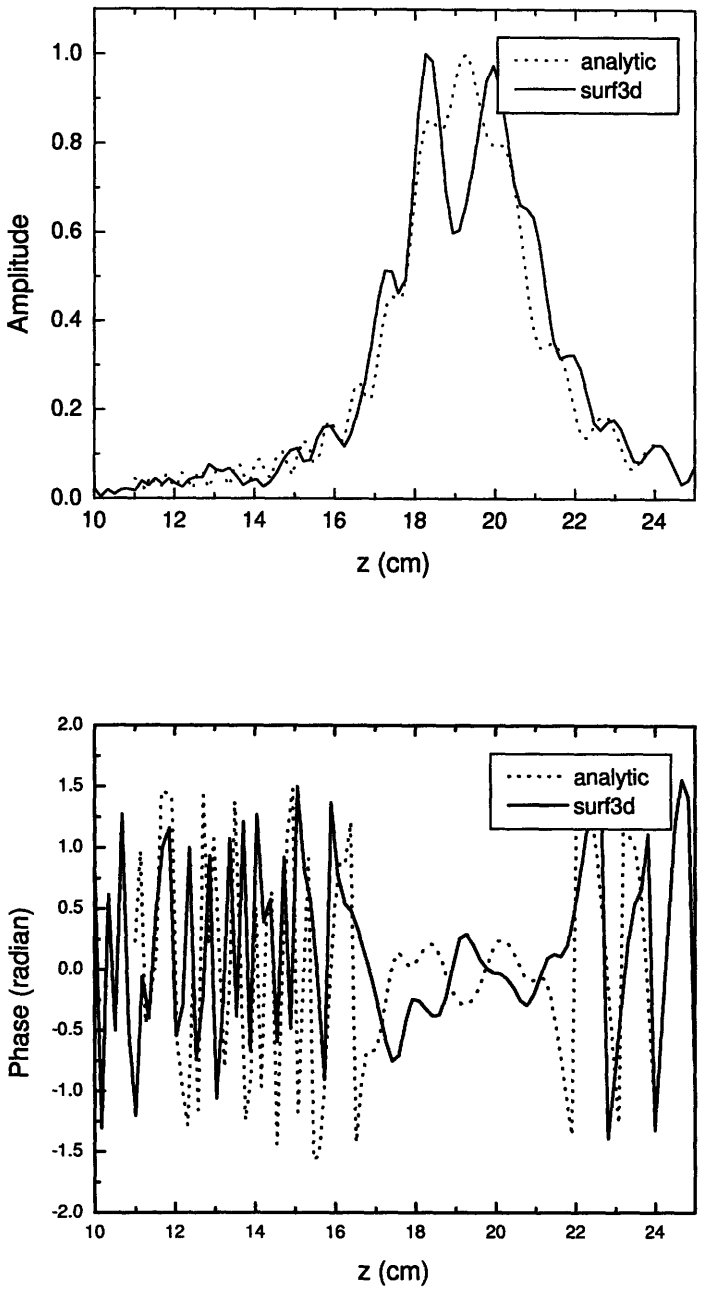

Figure 5-9: (a) Amplitude along z at radius of cylinder 10 cm. (solid: Surf3D, dot: analytic) (b) Phase along z at radius of cylinder 10 cm. (solid: Surf3D, dot: analytic)

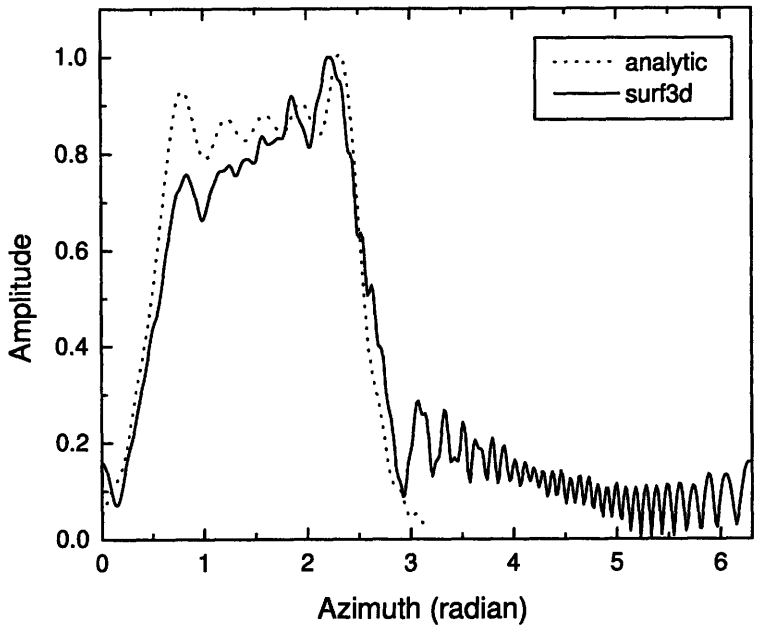

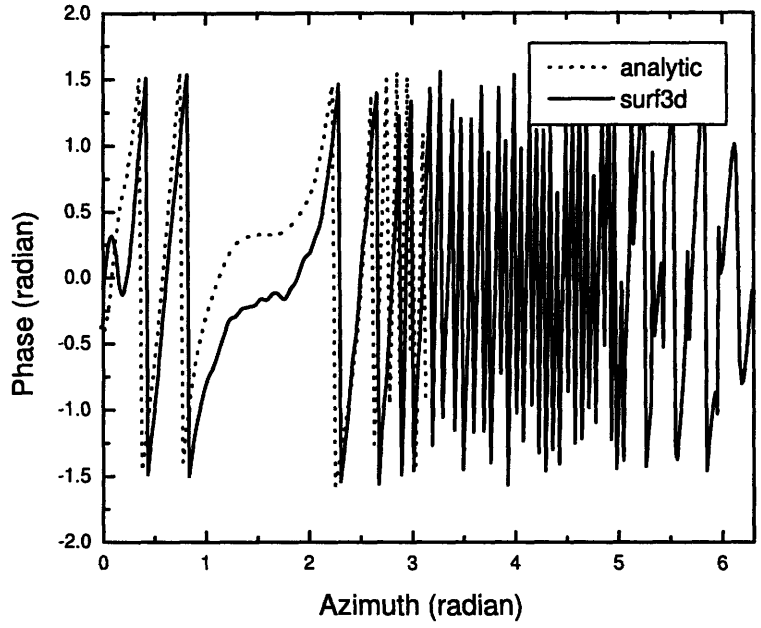

Figure 5-10: (a) Amplitude along azimuth ϕ at radius of cylinder 10 cm. (solid: Surf3D, dot: analytic) (b) Phase along ϕ at radius of cylinder 10 cm. (solid: Surf3D, dot: analytic)

found very good agreement between the asymptotic representation of the radiation field and the numerical simulations.

For the field distribution in the axial plane (z axis), the analytic results from the quasi-optical representation are plotted and compared to the numerical results in Figs. 5-5, 5-7, and 5-9. The radiated field patterns from the quasi-optical representation results up to the radius of cylinder of 4 cm match very well with the numerical results in terms of the change of the field amplitude and the phase amplitude. However, as the radius of observation cylinder becomes large (r_1=10 cm) there is a discrepancy at the center of the radiated field between the analytic result and numerical result. A better asymptotic is needed to explain the axial field distribution in the far field (Fig. 5-9(a)).

For the field distribution in the azimuthal plane, the results from the geometrical optics representation (Eq. 5.33) and the quasi-optical representation (Eq. 5.32) are generated and the results show identical field patterns for both representations. This means that once the ray leaves the waveguide it is in the geometrical optics zone which extends all the way to infinity (The calculated Fresnel number is $N_F = 32$ at infinity and is higher as we approach to the aperture of the waveguide cut.). Therefore, only quasi-optical results are plotted in Fig. 5-6, 5-8, and 5-10 and compared to the numerical results. The amplitude distributions in Figs. 5-6(a), 5-8(a), and 5-10(a) are plotted in the full region of the azimuthal direction which includes the light and dark regions. There is a good agreement between the analytic results and numerical results. The amplitude distribution is not symmetrical which is consistent with geometrical optics. In fact, one side on the light region is closer to the aperture than the other. However the sidelobes are present in the amplitude plots in the numerical results whereas the analytic results do not show the sidelobes. The phase distributions presented in Figs. 5-6(b), 5-8(b), and 5-10(b) show also a good agreement between the analytic theory and the numerical results. The phase flattens out in the light region surrounding the central ray according to the analytic representation. The phase becomes a quickly varying function of the azimuthal coordinate outside the light region because the observation cylinder does not coincide with the phase front

$s = const.$

Many gyrotron launchers and mirror designs are based on geometrical optics. The high power gyrotron mode converter cannot be rigorously described due to the operating frequency range and source beam characteristics. We have solved the geometrical optics solution for the rotating source in the representation of the ray coordinates. In the quasi-optical solution, we included the diffraction term for the edge effects. The Surf3D simulation code is a rigorous code that solves the electric field integral equation(EFIE). The comparison between the Surf3D simulation and analytic solution will give a somewhat better understanding for the mode converter description. The result shows that geometric optics describes the mode converter well enough to describe the radiation field qualitatively and to give reasonable quantitative information.

5.2.6 Conclusions

We found good agreement between the geometric optical and quasi-optical approximation results for the radiation from a helical cut of a circular waveguide and the numerical results using the surface integral equation method. The geometric optical and quasi-optical results are very close for the field outside the waveguide. The geometric optical approximation is especially simple and allows us to design the phase correcting mirrors for the radiation conversion and transmission. Internal gyrotron mode converters have been designed in the past using the geometrical optics approach. It has not been determined to what extent this approach can be used. The advanced mode converters utilize an irregular, dimpled waveguide with a helical cut. The results of this calculation can be generalized to represent the radiation from a helical cut of an irregular waveguide. This can be done if the azimuthal amplitude $A_0(\theta)$ and transverse amplitude $A_0(\xi)$ are non-uniform.

5.3 New Design of Internal Mode Converter

An internal mode converter was built for the gyrotron based on a previous MIT design [59, 60]. This converter worked well, as discussed in Section 5.4. A second

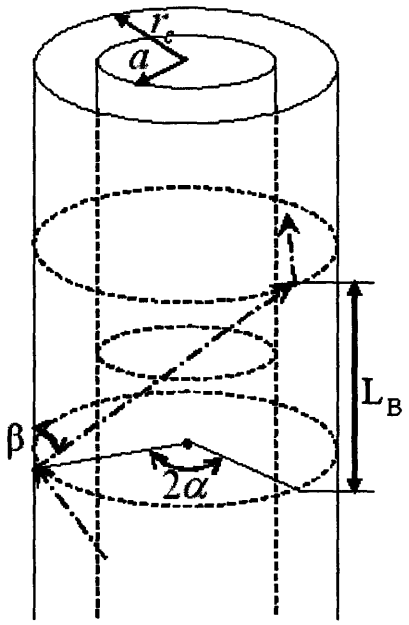

Figure 5-11: Ray propagation in a cylindrical waveguide.

mode converter was designed to attempt to achieve a higher efficiency. The design is discussed in this section. Section 5.3.1 discusses the basic design theory for a launcher and mirrors. Section 5.3.2 describes simulation codes for designing the launcher and mirrors. The launcher design and mirror design will be discussed in Section 5.3.3.

5.3.1 Design Theory

Launcher

The launcher design is based on geometrical optics, which represents waveguide modes as a series of rays. The ray representation describes with sufficient accuracy the fields of high order modes over the entire cross section of the waveguide, except for the region near the caustic. At the caustic, geometrical optics approaches an infinite field intensity, whereas in reality the field intensity at the caustic is finite. The caustic radius is $r_c = a\frac{m}{\nu_{mp}}$, where a is a wall radius, m is an azimuthal index, and ν_{mp} is the root of the equation $J_m^{'}(\nu_{mp}) = 0$.

Fig. 5-11 shows how a ray propagates in the cylindrical waveguide. L_B is the length that a ray has propagated in the axial direction between two subsequent reflections at the waveguide wall.

$$\begin{aligned} L_B &= \frac{2a\sin\alpha}{\tan\theta_B} \\ &= \frac{2a}{\tan\theta_B}\sqrt{1-\left(\frac{m}{\nu_{mp}}\right)^2} \end{aligned} \tag{5.44}$$

The Brillouin angle θ_B is expressed as follows.

$$\theta_B = \arcsin\left(\frac{\nu_{mp}}{ka}\right) \tag{5.45}$$

Each reflection point of the ray is shifted azimuthally relative to the previous one by an angle,

$$\beta = \arctan\left(\frac{\alpha\tan\theta_B}{\sin\alpha}\right) \tag{5.46}$$

and the distance (pitch) that a ray propagates in the axial direction with a complete full turn is expressed as Eq. 5.47, and is an important parameter in the launcher design known as the launcher cut.

$$D = 2\pi a\cot\beta = \frac{2\pi a\sin\alpha}{\alpha\tan\theta_B} \equiv L_c \tag{5.47}$$

The Brillioun region is defined as a section of the waveguide wall which is intercepted by a complete bundle of rays on one bounce. The complete bundle of rays carry the full power of the microwave beam. Therefore elimination of one Brillioun region on the waveguide wall at the end of the launcher makes all rays propagate out of the launcher and all of the power radiate from the waveguide.

The conventional launcher which is a simple cut in the waveguide wall and whose azimuthal and axial field distribution is uniform at the aperture leads to very high diffraction losses (about 20 % diffraction loss) due to sidelobes [45]. In high power gyrotrons, high diffraction losses result in serious problems of stray radiation inside the tube and a low quality Gaussian output beam. Therefore, preshaping the beam

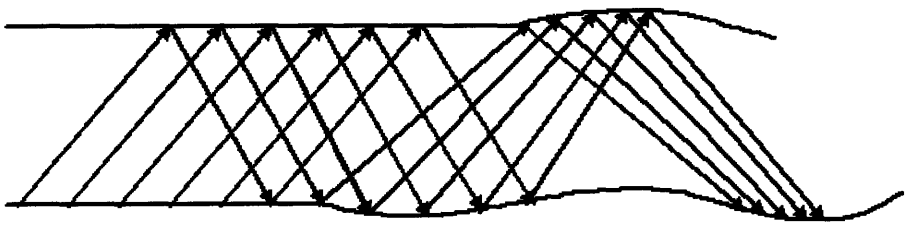

Figure 5-12: A schematic of an axial focusing of the beam in a dimpled wall launcher in axial propagation. Arrows represent rays.

at the aperture of the launcher before launching it to the mirrors is required in order to reduce possible diffraction losses. The goal for the launcher design is, therefore, to make the preshaped beam at the aperture high in Gaussian content before it is launched [61].

Fig. 5-12 shows the conceptual idea behind the dimpled wall launcher. As rays propagate by bouncing off the launcher dimples, they are focused along an axial direction as well as the azimuthal direction. In highly overmoded gyrotrons, the dimpled wall is designed by using the technique of mode mixture.

Now, we introduce a dimpled wall launcher. To achieve a well preshaped Gaussian beam at the aperture of the launcher, the waveguide mode must be converted to a mixture of modes by using a geometrical deformation of the launcher wall (scattering surface). A nearly Gaussian field distribution can be formed by a superposition of three waves in one coordinate. In the cylindrical launcher, we convert the waveguide beam mode in both axial and azimuthal coordinates. Therefore the field composition $f(\phi, z)$ of the main wave and a mixture of two neighboring waves can be written as [44],

$$f(\phi, z) = \left(1 + \frac{1}{2}e^{i(2\pi/L)z} + \frac{1}{2}e^{-i(2\pi/L)z}\right) \cdot \left(1 + \frac{1}{2}e^{i(\pi/\alpha)\phi} + \frac{1}{2}e^{-i(\pi/\alpha)\phi}\right). \quad (5.48)$$

The interference of the nine waveguide modes represented by Eq. 5.48 creates a bunching in the axial and azimuthal directions. There are requirements for the bunching.

1. Longitudinal bunching: The modes must have equal caustic radii and an interfer-

ence length close to the launcher cut length, L_c.

2. Azimuthal bunching: the modes must have equal caustic radii and similar Bessel function zeros. These conditions lead to the following mode selection rules,

$$\begin{aligned} \Delta\beta &= \pm\frac{2\pi}{L_c} \\ \Delta m &= \pm\frac{\pi}{\alpha} \end{aligned} \tag{5.49}$$

The wall deformation (dimples) is described by the following equation.

$$r(\phi, z) = r_0[1 + \epsilon_1 \cos(\Delta\beta_1 z - l_1\phi) + \epsilon_2 \cos(\Delta\beta_2 z - l_2\phi)] \tag{5.50}$$

where,

$$\Delta\beta_1 = \pm(\beta_1 - \beta_2), l_1 = \pm(m_1 - m_2) = \pm 1 \tag{5.51}$$

$$\Delta\beta_2 = \pm(\beta_1 - \beta_3), l_2 = \pm(m_1 - m_3) = \pm 3 \tag{5.52}$$

and r_0 is the input radius of the laucher, ϵ_1 and ϵ_2 are perturbation amplitudes, β_1 is the propagation constant of the operating waveguide mode, and β_2 and β_3 are the propagation constants of modes that satisfy the condition of Eq. 5.49. Eq. 5.50 has two terms of *cos* since the bunching occurs in axial and azimuthal directions. The required minimum launcher length is

$$L_{min} = \frac{\pi}{2|2\beta_{m,n} - \beta_{m+1,n} - \beta_{m-1,n}|}. \tag{5.53}$$

A simple explanation of the physical picture of the dimpled wall launcher in the geometrical point of veiw is the following (refer to the picture of the conceptual description in Fig. 5-12): The modes propagate on the launcher wall and the central mode, which is the waveguide mode, is reflecting at the reflecting point. At this point, the wall is going to be deformed such that the central mode will be focused near the reflection points and defocused at the remaing area. After several helical turns of the rays, the rays will converge to a well focused Gaussian beam.

In the case of the $TE_{22,6}$ operating mode, $\Delta m = \pm 3$ since $\alpha \approx \frac{\pi}{3}$, i.e. $m = 19$ or $m = 25$. And in the azimuthal direction for bunching, $\nu_{mp} \approx \nu_{22,6}$ ($k_z \approx k_{z_{22,6}}$), resulting in the selection of modes $TE_{19,7}$ and $TE_{25,5}$. In the longitudinal bunching case, $k_z - k_{z_{22,6}} \approx \frac{D_1}{2}$. Therefore for the longitudinal bunching, the selected modes are the $TE_{21,6}$ mode and the $TE_{23,6}$ mode.

The analysis on the launcher design is done using the coupled mode theory [59]. Generally, the fields in a deformed wall of the waveguide are not described by one normal mode. The wall perturbations now couple energy of the waveguide mode into several normal modes of the waveguide. In general, the equations for coupling between forward traveling modes are given by

$$\begin{aligned} \frac{dA_i^+}{dz} &= ik_{zi}A_i^+ + \sum_p c_{ip}A_p^+ + \sum_q c_{iq}A_q^+ \\ \frac{dA_j^+}{dz} &= ik_{zj}A_j^+ + \sum_p c_{jp}A_p^+ + \sum_q c_{jq}A_q^+ \end{aligned} \tag{5.54}$$

where the subscripts i and p denote TE modes and the subscripts q and j denote TM modes. A waveguide deformation in Eq. 5.50 can be used to determine the coupling coefficients in Eq. 5.54.

$$\begin{aligned} c_{ip} &= \frac{1}{2}\left[Q_{ip}\frac{\omega\mu}{\sqrt{k_{zi}k_{zp}}} + R_{ip}\sqrt{\frac{k_{zp}}{k_{zi}}}\right] \\ c_{iq} &= \frac{1}{2}S_{iq}\frac{\omega}{c\sqrt{k_{zi}k_{zq}}} \\ c_{jp} &= \frac{1}{2}\left[T_{jp}c\sqrt{\frac{k_{zj}}{k_{zp}}} + U_{jp}\frac{1}{c}\sqrt{\frac{k_{zp}}{k_{zj}}} + V_{jp}\frac{c}{\omega}\sqrt{k_{zj}k_{zp}}\right] \\ c_{jq} &= \frac{1}{2}\left[W_{jq}\sqrt{\frac{k_{zj}}{k_{zq}}} + X_{jq}\frac{\omega\epsilon}{\sqrt{k_{zj}k_{zq}}}\right] \end{aligned} \tag{5.55}$$

The expressions for Q_{ip}, R_{ip}, S_{iq}, T_{jp}, U_{jp}, V_{jp}, W_{jq}, X_{jq} are rather lengthy and may be found in the thesis of Dr. Monica Blank [59].

Mirror system

If the beam radiated from the launcher tip is a well-preshaped Gaussian beam, we can apply Gaussian beam optics from the first mirror in order to focus or defocus the beam to the window. The Gaussian beam is different from the beam of the geometrical optics description because it has a finite transverse beam size at the source in the Gaussian beam compared to the point source used in geometrical optics. The Gaussian beam optics fundamental mode is derived from the paraxial approximation in which it is assumed that the variation of the amplitude along the direction of propagation will be small over a distance compared to a wavelength, and that the axial variation will be small compared to the variation perpendicular to this direction [62]. Solutions to the paraxial wave equation are the Gaussian beam modes. There is no rigorous "cutoff" for the application of the paraxial approximation, but it is generally reasonably good as long as the angular divergence of the beam is confined to within 0.5 radian (or about 30 degrees) of the z axis [62]. Errors will be introduced beyond the paraxial approximation [63]. Here the most useful equations are as a result of solving the axially symmetric paraxial wave equation.

$$w = w_0 \left[1 + \left(\frac{2z}{kw_0^2}\right)^2\right]^{1/2} \tag{5.56}$$

$$R = z \left[1 + \left(\frac{kw_0^2}{2z}\right)^2\right] \tag{5.57}$$

where w_0 is the beam waist (minimum beam radius) at which the curvature radius R goes to infinity. Along with Eq. 5.56 and Eq. 5.57, the phase variation at a fixed value of z as a function of r can be written as,

$$\phi(r) \cong \frac{kr^2}{2R}. \tag{5.58}$$

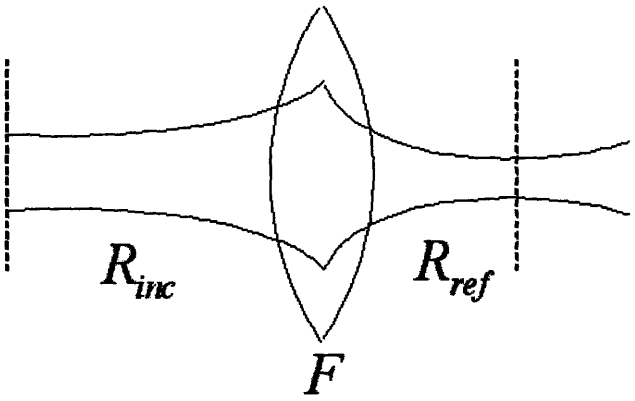

Figure 5-13: Schematic of Gaussian beam transformation by a focusing element.

The Gaussian beam expansion equations can be more generally written as

$$w_2 = w_1 \left[\left(1 + \frac{z'}{R_1} \right)^2 + \left(\frac{2z'}{kw_1^2} \right)^2 \right]^{1/2} \tag{5.59}$$

$$R_2 = z' \frac{\left(1 + \frac{z'}{R_1} \right)^2 + \left(\frac{2z'}{kw_1^2} \right)^2}{\frac{z'}{R_1} \left(1 + \frac{z'}{R_1} \right) + \left(\frac{2z'}{kw_1^2} \right)^2} \tag{5.60}$$

where at $z = z_1$ the beam radius w is w_1 and the phase front is $R = R_1$, and z' is $z' = z_2 - z_1$. Using optical mirrors, the Gaussian beam can be propagated as it is focused and defocused.

Fig. 5-13 shows a schematic of Gaussian beam propagation as it passes through a focusing element, which in fact is equivalent to mirror components in the mode converter system. As shown in the Fig. 5-13, the mirror curvature can be determined by matching the incoming Gaussian beam whose radius of curvature is R_{inc} with the reflecting Gaussian beam whose radius of curvature is R_{ref} by means of the following equation,

$$\frac{1}{F} = \frac{1}{R_{inc}} + \frac{1}{R_{ref}}. \tag{5.61}$$

Then, the mirror curvature, R_m, is given by the following equation,

$$F = \frac{R_m}{2}. \tag{5.62}$$

5.3.2 Codes

LOT(Launcher Optimization Tool)

A launcher is designed using the code LOT (version 1.21), which has been developed by Calabazas Creek Research, Inc. (CCR). LOT is a computer code for optimizing the design of Quasi-optical launchers used in high power gyrotrons [64]. The numerical optimization process allows us to have a design with very low diffraction losses and very high Gaussian content at the aperture of the launcher. It starts the optimization process by having a wall deformation function of a generalized form as,

$$r(\phi, z) = r_0 + \alpha z + \sum_l \sum_m a_{lm}(z) \cos(H_{lm}(z) - l\phi). \tag{5.63}$$

where r_0 is the average wall radius and α is the tapered slope. This generalized form gives results somewhat better than those obtained with the simpler form given by Eq. 5.50. $a_{lm}(z)$ and $H_{lm}(z)$ are modeled as cubic splines where the spline points are the free parameters for optimization. For minimizing possible spurious modes, an even more generalized surface form is used for intermediate and final optimizations. Eq. 5.64 expresses the surface form,

$$r(\phi, z) = r_0 + \alpha z + \sum_l [f_l(z) \cos(l\phi) + g_l \sin(l\phi)]. \tag{5.64}$$

where the functions $f_l(z)$ and $g_l(z)$ are modeled as cubic splines. The goal of the optimization of the surface synthesis is minimization of the field along the spiral cut of the launcher and maximization of the complex Gaussian content on the aperture. LOT uses a coupled mode theory to solve the field at the aperture and uses a Stratton-Chu formulation to obtain the radiated field from the aperture.

Surf3D

Surf3D is a computer code for calculation of the RF field scattered from an arbitrary metal surface with an incident field described in terms of a waveguide mode expansion. It solves the electric field integral equation (EFIE) given by

$$\int_S G(r,r') \cdot J(r')dS' = \frac{4\pi}{k\eta} E^i(r) \tag{5.65}$$

for r on surface S, where $J(r')$ is the unknown surface current, $E^i(r)$ is the incident waveguide source field and the Green's function is defined as

$$\begin{aligned} G(r,r') &= \left(I - \frac{1}{k^2}\nabla\nabla'\right) g(r,r') \\ g(r,r') &= \frac{e^{ikR}}{|r-r'|}. \end{aligned} \tag{5.66}$$

SCATTER

SCATTER was developed for the radiated field calculation at an arbitrary metal surface by Dr. Monica Blank, a former graduate student at MIT. It uses the Stratton-Chu formula [65], which is appropriate for the specified aperture integration and near field calculation. With the Stratton-Chu formula, the electric field and magnetic field are calculated at an observation point by integrating the source Green's function weighted by the amplitude and phase of the fields on the aperture over all source regions. The E and H fields at an observation point, r, are given by

$$\begin{aligned} \mathbf{E}(\mathbf{r}) = \oint_{S'} dS' \{ & i\omega\mu[\hat{\mathbf{n}} \times \mathbf{H}(\mathbf{r}')]g(\mathbf{r},\mathbf{r}') + [\hat{\mathbf{n}} \cdot \mathbf{E}(\mathbf{r}')]\nabla' g(\mathbf{r},\mathbf{r}') \\ & + [\hat{\mathbf{n}} \times \mathbf{E}(\mathbf{r}')] \times \nabla' g(\mathbf{r},\mathbf{r}')\} \end{aligned} \tag{5.67}$$

$$\begin{aligned} \mathbf{H}(\mathbf{r}) = \oint_{S'} dS' \{ & -i\omega\epsilon[\hat{\mathbf{n}} \times \mathbf{E}(\mathbf{r}')]g(\mathbf{r},\mathbf{r}') + [\hat{\mathbf{n}} \cdot \mathbf{H}(\mathbf{r}')]\nabla' g(\mathbf{r},\mathbf{r}') \\ & + [\hat{\mathbf{n}} \times \mathbf{H}(\mathbf{r}')] \times \nabla' g(\mathbf{r},\mathbf{r}')\} \end{aligned} \tag{5.68}$$

Using the physical optics approximation, the currents from the reflector surface from the fields obtained from Eq. 5.68 are expressed as,

$$\mathbf{J_s} = 2(\hat{\mathbf{n}} \times \mathbf{H}). \tag{5.69}$$

The surface currents from the above equation, Eq. 5.69 now can be re-radiated and the fields at a final observation point can be obtained from the following equations,

$$\mathbf{E} = \frac{i}{4\pi\omega\epsilon}\int_{S'}[(\mathbf{J_s}\cdot\nabla')\nabla' + k^2\mathbf{J_s}]\frac{e^{i\mathbf{k}\cdot\mathbf{R}}}{R}dS' \tag{5.70}$$

$$\mathbf{H} = \frac{1}{4\pi}\int_{S'}(\mathbf{J_s}\times\nabla')\frac{e^{i\mathbf{k}\cdot\mathbf{R}}}{R}dS'. \tag{5.71}$$

5.3.3 Design

Launcher

The new launcher optimization was done by using the code, LOT [66] by Dr. Jeff Neilson at CCR. The total length of the launcher is 16.4 cm. The launcher begins at the radius of 2.0955 cm which is exactly same value as the cavity output radius and ends at the radius of 2.1966 cm. Therefore, the launcher has a slight taper whose angle is 0.35° (0.006 radian).

As explained in the Section 5.3.1, a launcher pumps the cavity waveguide mode into a mixture of modes. Fig. 5-14 is a plot of modes as a function of z (z is the launcher and gyrotron axis) in the launcher. Based on the conditions in Eq. 5.49, the $TE_{22,6}$ waveguide mode is converted into proper satellite modes. Table 5.1 shows the fundamental composition of modes obtained from Eq. 5.49. The central mode is the $TE_{22,6}$. The optimization process of the launcher allows for inclusion of additional satellite modes, such as the $TE_{24,6}$ mode, the $TE_{16,8}$ mode and the $TE_{17,8}$ mode.

As the $TE_{22,6}$ mode is converted to the composition of satellite modes, azimuthal and axial bunching occurs, leading to the formation of the pre-shaped Gaussian beam. In Table 5.1, row modes are related to the axial bunching and column modes are related to the azimuthal bunching. Therefore, the field (H field) of the unwrapped

Table 5.1: Table of a set of modes in the launcher

$TE_{18,7}$	$TE_{21,6}$	$TE_{24,5}$
$TE_{19,7}$	$TE_{22,6}$	$TE_{25,5}$
$TE_{20.7}$	$TE_{23,6}$	$TE_{26,5}$

launcher will form the bunching axially and azimuthally. Fig. 5-15 clearly shows the formation of bunching in the unwrapped launcher geometry. The launcher cut is shown by the dotted white line of Fig. 5-15 which takes one of the bunched beams out to free space. The launcher cut length is optimized to be 4.1 cm. The resultant output pre-shaped Gaussian beam is shown in Fig. 5-16 at the launcher tip plane (here the launcher tip plane means the plane of the launcher cut whose directional vector is ϕ (azimuth).). The maximum of the beam is at the position of r=1.059 cm as shown in Fig. 5-16, which happens to be exactly the same value as the caustic radius.

The actual dimpled wall launcher shape is described in Fig. 5-17. The dimples are optimized and the geometry file for it is generated. The field pattern on a cylindrical surface of radius 5 cm is shown in Fig. 5-18 obtained from the Surf3D simulation. As shown in the Fig. 5-18, the beam from the launcher is very well focused without significant sidelobes up to -30 dB.

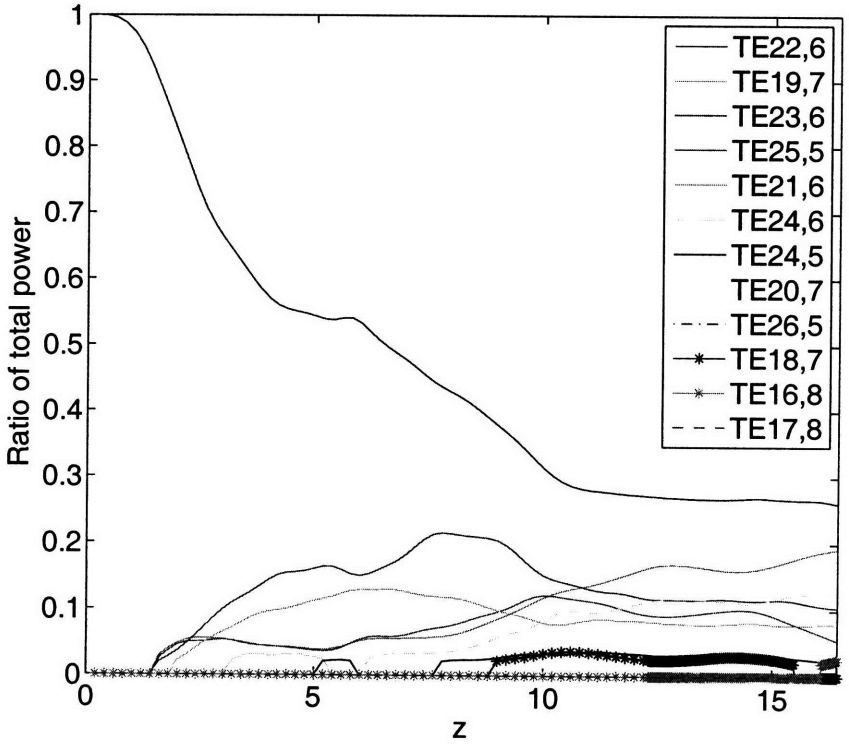

Figure 5-14: Mode mixture in the launcher simulated from LOT.

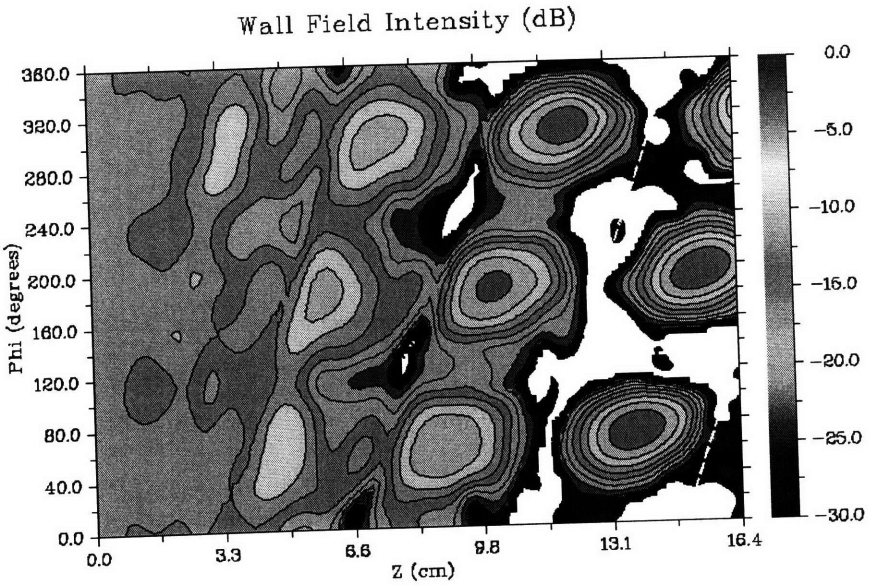

Figure 5-15: Wall Field of the launcher

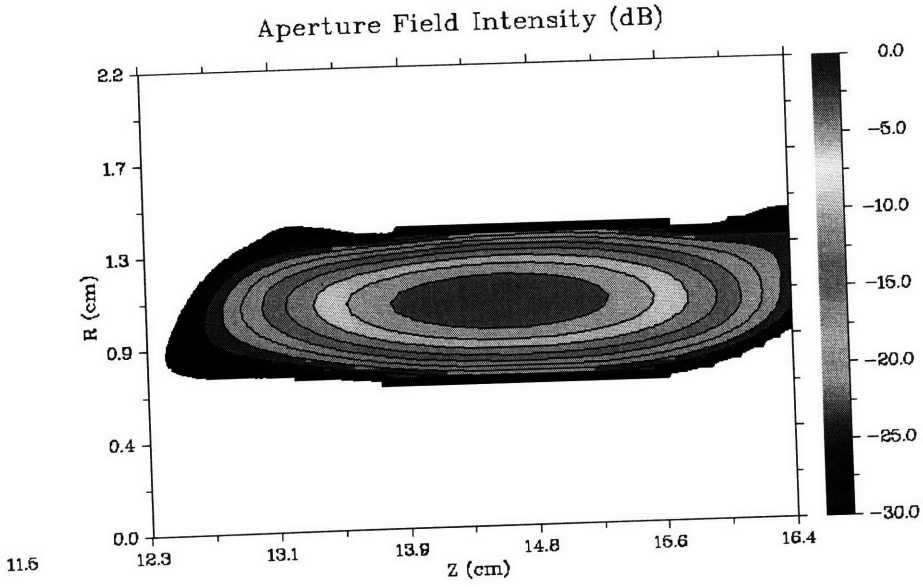

Figure 5-16: Field at the launcher aperture simulated from Surf3D.

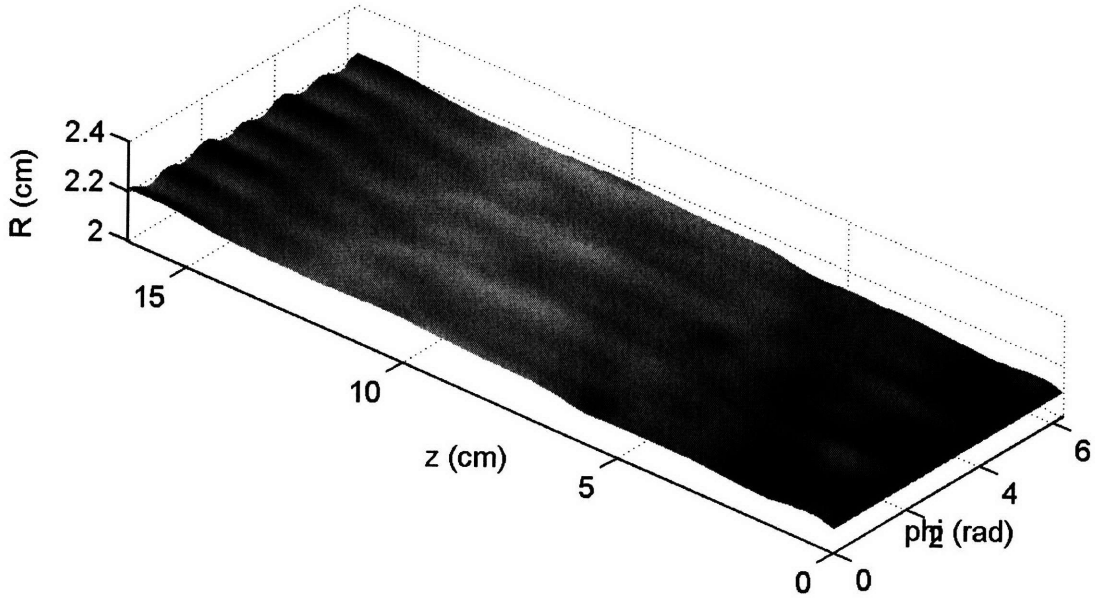

Figure 5-17: Unwrapped launcher geometry shape with dimples simulated from Surf3D.

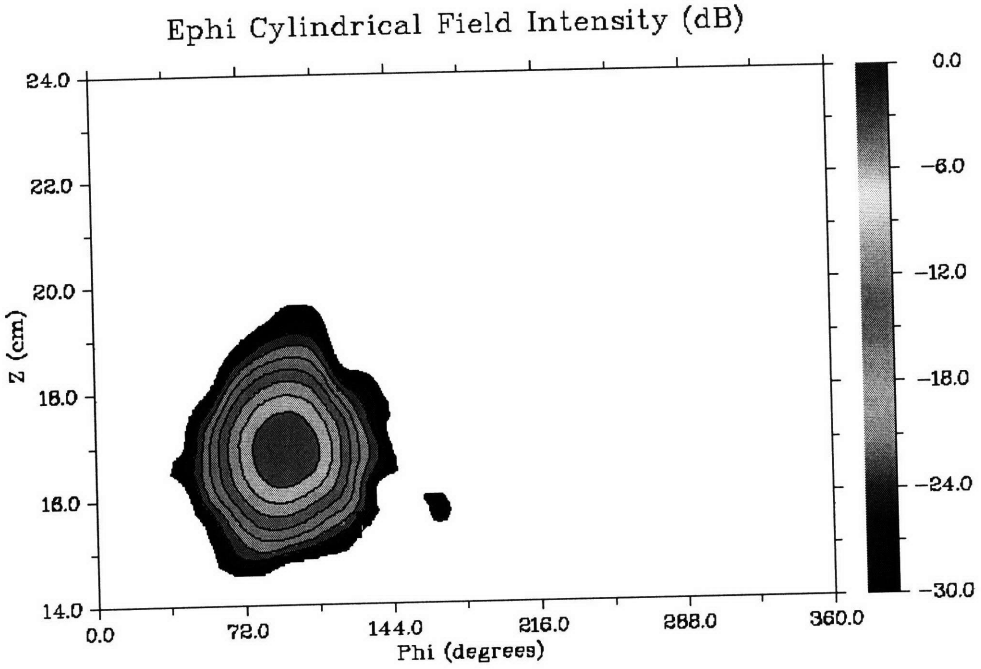

Figure 5-18: Surf3D plot of the field pattern taken on a cylindrical surface of radius of 5 cm centered at (x,y,z)=(1.059,0,0)

Mirrors

Based on the new launcher design in Section 5.3.3, the mirrors now can be designed. The mirror design can make use of the properly pre-shaped Gaussian beam of the new launcher. The Gaussian beam optics described in Section 5.3.1 are employed in the mirror design. Mirrors are considered to be lenses for focusing and defocusing the Gaussian beam. The new mirror system consists of 4 mirrors. The mirror design starts from the radiated field pattern obtained from the Surf3D simulation and designed by the SCATTER simulation as introduced in Section 5.3.2.

Fig. 5-19 shows the E_x field pattern along radius at the launcher tip. The beam can be considered to be Gaussian from the observation of not only the field amplitude but also the phase.

Let's consider the vertical beam size. The vertical beam waist at the launcher tip is determined to be 0.22 cm. By means of Eq. 5.56 and Eq. 5.57, the radius and the phase front of the beam at z=5 cm are determined. k is now $k \simeq \frac{\nu_{22,6}}{a}$ where a is the output radius of the launcher, a=2.1966 cm. As a result, the radius of the beam at z=5 cm is $w \simeq 2.2$ cm and the phase front of the beam is $R_{inc} \simeq 5$ cm. Therefore the first mirror, mirror 1 (M1) curvature (R_m) is determined by

$$\begin{aligned} \frac{1}{F} &= \frac{1}{R_{inc}} + \frac{1}{R_{ref}} = \frac{1}{5} + \frac{1}{\infty} \\ R_m &= 2F = 10\ cm \end{aligned}$$

imposing that the reflecting wave from the M1 is plane wave ($R_{ref} = \infty$). The curvature of M1 is 10 cm centered at (x_m, y_m)=(1.059 cm,5 cm). The coordinate of the mirror system is shown in Fig. 5-20 which follows the coordinate setup of the SCATTER code. The simulated E_x field amplitude and phase at M1 from Surf3D are shown in Fig. 5-21. A Gaussian-like amplitude and a flat phase are obtained at M1 which indicates the beam from the launcher is radiated following Gaussian beam optics.

Further propagation of the Gaussian beam from M1 to the window is done using Gaussian beam optics. Curvatures and positions of all mirrors (M2, M3, and M4) are

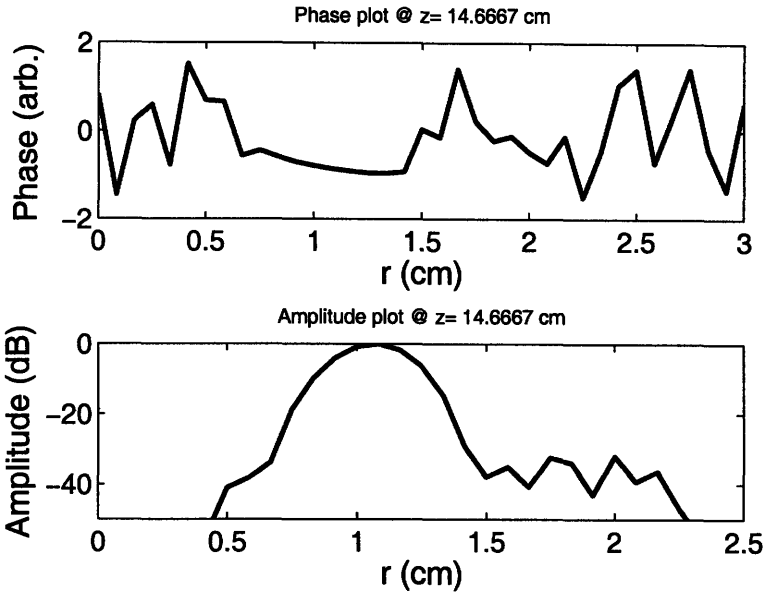

Figure 5-19: E_x field amplitude and phase along r at the launcher tip

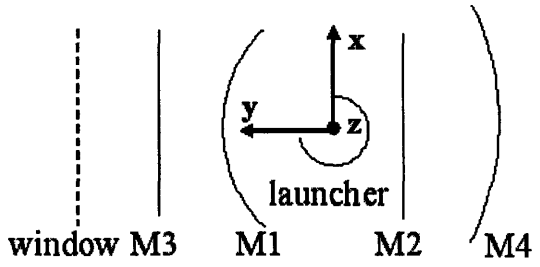

Figure 5-20: A coordinate of the mirror system for SCATTER.

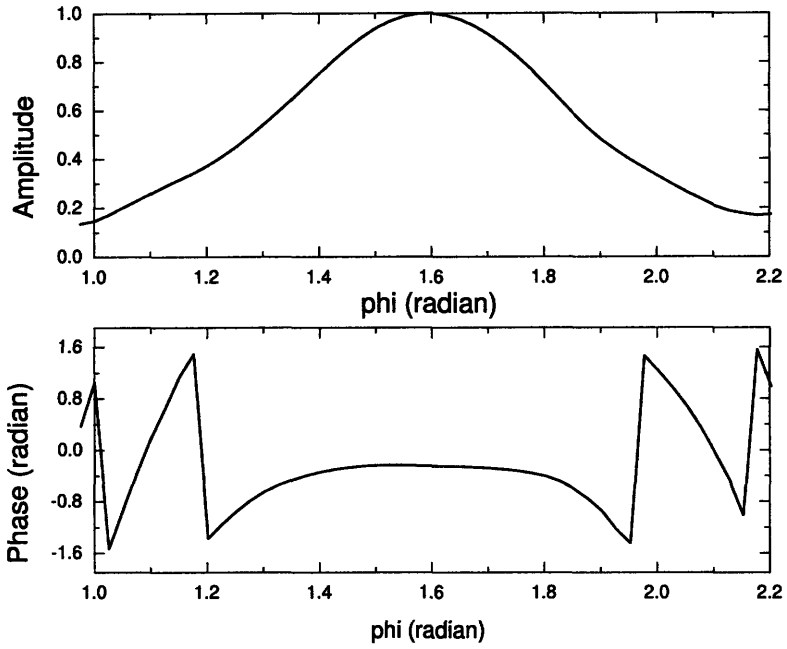

Figure 5-21: E_x amplitude and phase plots as a function of azimuth obtained in the cylinder of the radius R=10 cm at the center of (x_m, y_m)=(1.059 cm,5 cm) from Surf3D.

Table 5.2: Summary of the mode converter mirrors

	Beam size (w_x,w_z)	Mirror center (x_m,y_m,z_m)	Mirror size ($2R_x$,$2R_z$)	Curvature R_x	Curvature R_z
M1	(2.2,1.13)cm	(1.059,5,0)cm	(10,5)cm	10 cm	Flat
M2	(2.53,1.69)cm	(0,-5,5.038)cm	(10.2,6.8)cm	Flat	40 cm
M3	(2.71,2.474)cm	(0,11,12.48)cm	(10.9,10)cm	Flat	Flat
M4	(3.11,3.11)cm	(0,-10,22.55)cm	(14,14)cm	300 cm	120 cm
Window	(2.93,2.93)cm	(0,25.4,22.55)cm	(9.754,9.754)cm	Flat	Flat

determined. The window diameter is 3.84″ (9.754 cm), and the output beam size at the window is determined to be 2.93 cm.

Implementing the data of H fields from Surf3D on M2 to SCATTER, fields at the remaining mirror surfaces were simulated using SCATTER in order to check the design. The E_x fields simulated from SCATTER are plotted in Fig. 5-22 to Fig. 5-24. At last, the E_x field and phase on the window are obtained and the results are shown in Fig. 5-25 and Fig. 5-26. A very nice round Gaussian output beam and flat phase front up to -3 dB at the window is predicted from the SCATTER simulation, as shown in Fig. 5-25 and Fig. 5-26. The beam waist at the window predicted from SCATTER is roughly 2.9 cm and the value is in good agreement with the Gaussian beam design value.

5.4 Experiment

In this section, the experimental results from the existing MIT internal mode converter will be discussed. Former graduate students from this group have previously developed an internal mode converter [59, 60]. Mirrors 1 and 2 were designed by the Stratton-Chu vector diffraction theory, which is the basic formalism for the SCATTER code. Mirrors 3 and 4 were originally designed using the mirror synthesis technique based on the phase retrieval method. However, the measured field at Mirror 3 was found to have small phase errors. A method was developed at MIT to overcome this problem by using a phase retrieval technique in which measured field patterns are incorporated to design mirrors 3 and 4 [60]. This way, possible discrepancies

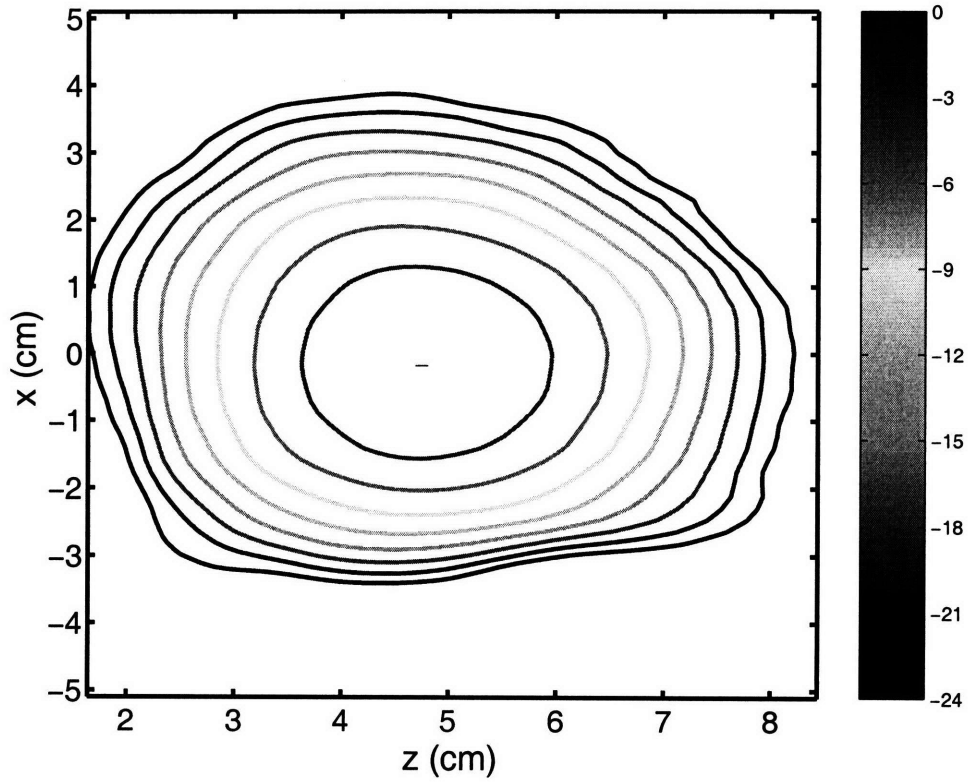

Figure 5-22: E_x amplitude contour plot on the M2 surface as a function of x and z obtained from SCATTER simulation. The contour color spectrum represents power in dB.

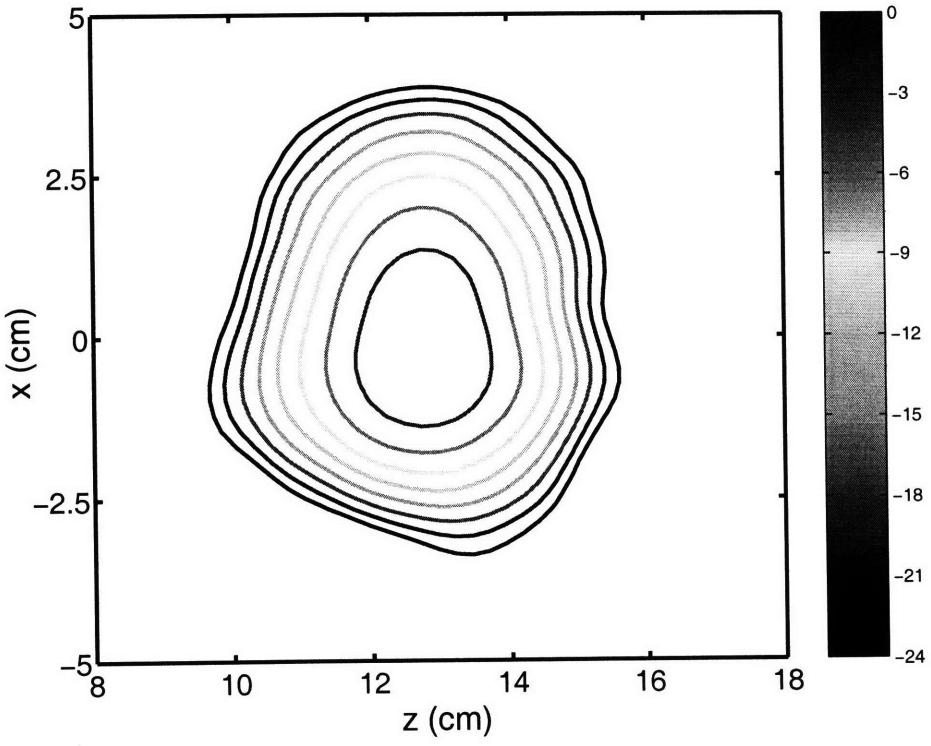

Figure 5-23: E_x amplitude contour plot on the M3 surface as a function of x and z obtained from SCATTER simulation. The contour color spectrum represents power in dB.

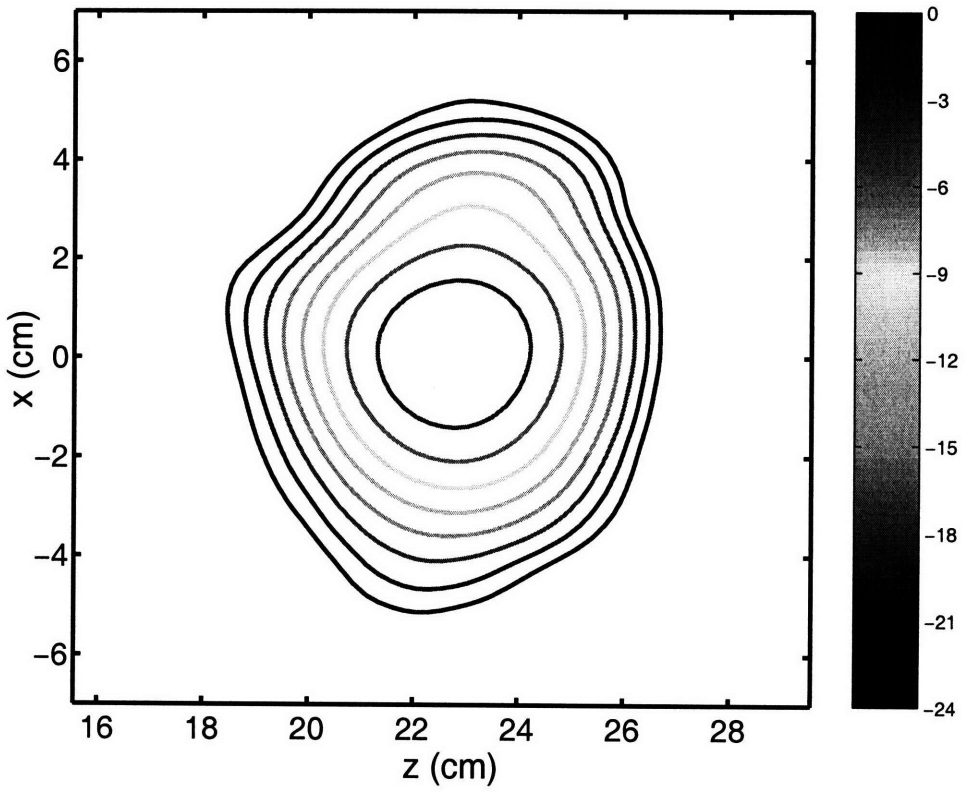

Figure 5-24: E_x amplitude contour plot on the M4 surface as a function of x and z obtained from SCATTER simulation. The contour color spectrum represents power in dB.

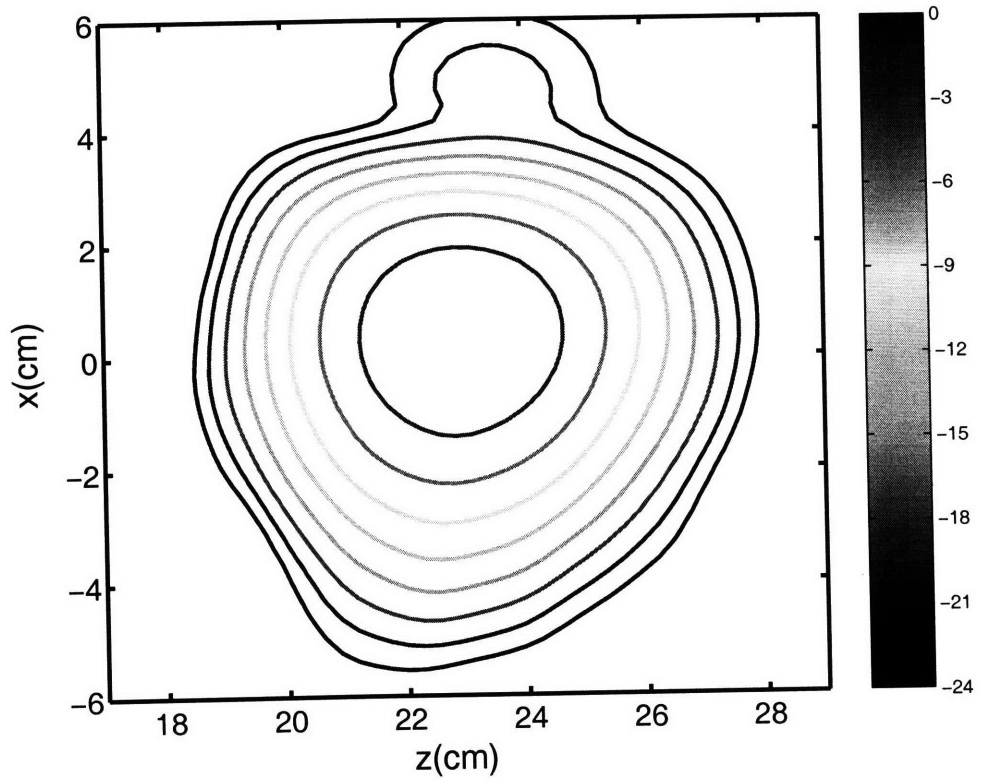

Figure 5-25: E_x amplitude contour plot on the window surface as a function of x and z obtained from SCATTER simulation. The contour color spectrum represents power in dB.

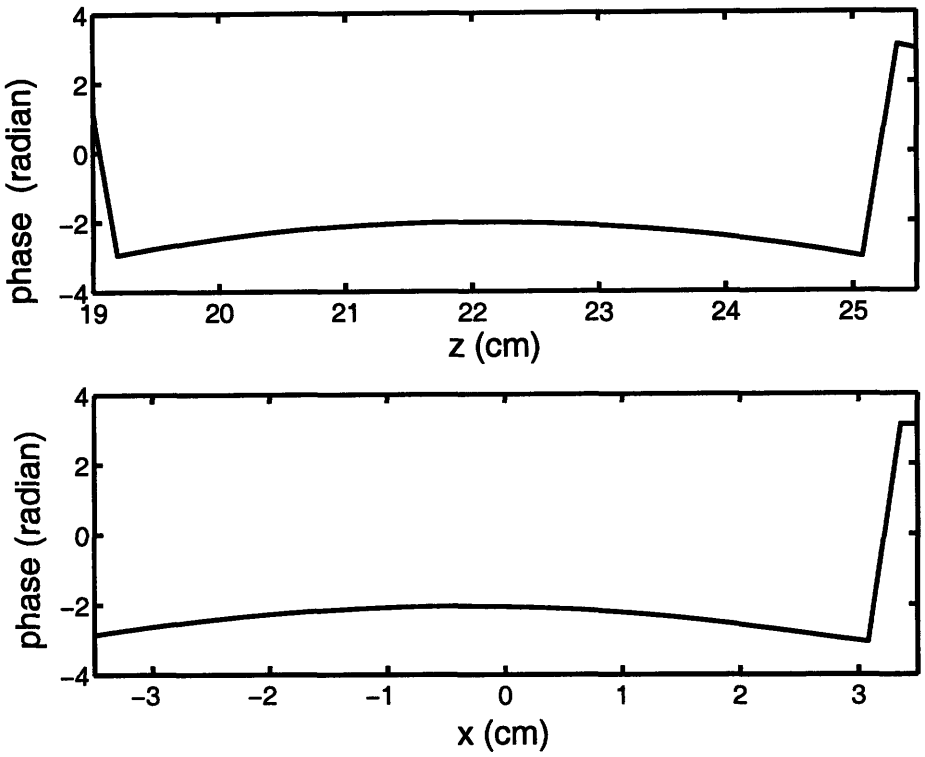

Figure 5-26: E_x phase plot on the window surface as a function of x and z obtained from SCATTER simulation.

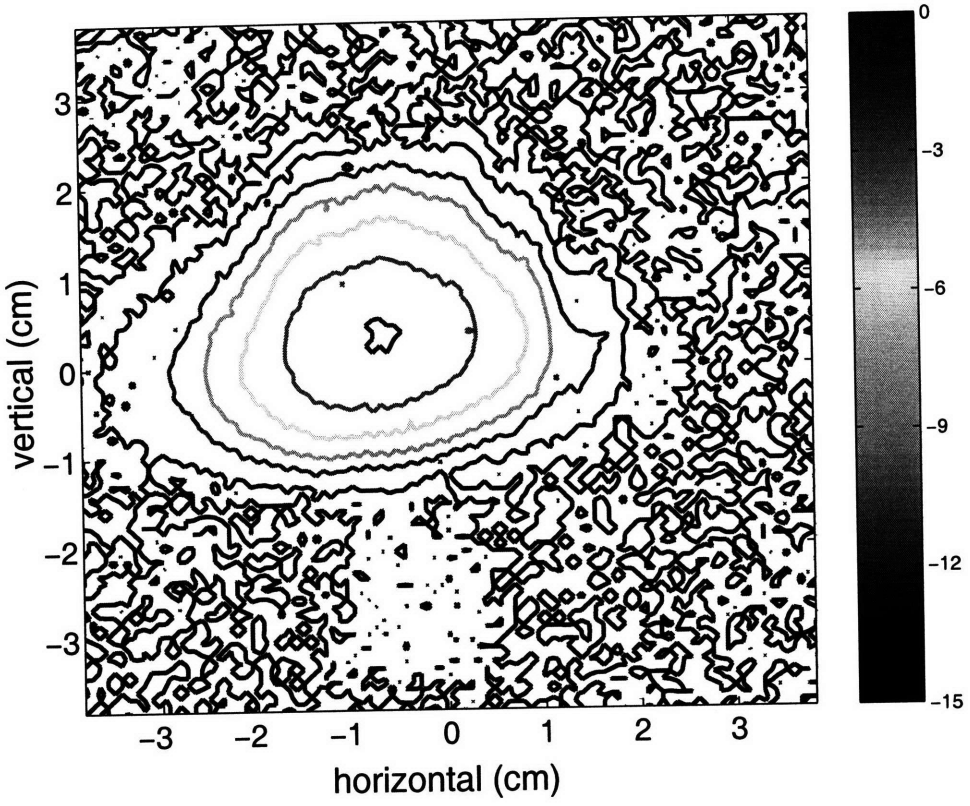

Figure 5-27: A cold test experimental measurement result. The measurement plane is 44.45 cm (17.5″) away from the mirror 4 center in y direction.

between the theory and the measurements are reduced so that an improved output beam profile can be obtained. The present launcher and mirrors are the same design as the one being used at CPI for a 1 MW, 110 GHz CPI gyrotron for long-pulse operation [67]. Our launcher and the whole mirror set were cold tested at CPI by Dr. Michael Shapiro and Dr. T. S. Chu in 2005. Fig. 5-27 is the result of a cold test experiment. The measurement plane is 44.45 cm away from the mirror 4 center in the y-direction and the center position in the measurement plane is the same as mirror 4. (Remember that the actual window location is 35.4 cm away in y direction from the mirror 4 center.) The results in Fig. 5-27 are very good and this mode converter was used at MIT.

Table 5.3: Nominal design parameters for the gyrotron

Frequency	110 GHz
Microwave Power	1.5 MW
Beam Voltage	96 kV
Beam Current	40 A
Beam Alpha ($\alpha = v_\perp/v_z$)	1.4
Operating Mode	$TE_{22,6}$
Pulse Length	3 μs
Cavity Magnetic Field	4.3 T
Depression voltage	None

5.4.1 Experiment setup

Fig. 5-28 shows the internal mode converter gyrotron experimental setup at MIT. Most of the gyrotron parts, including the electron gun and SC magnet that had previously been used in the axial configuration experiments (Chap. 4) were reused in the internal mode converter experiment. Based on the success of the V-2005 cavity, we continued to use it in these experiments. The part of the tube that contains the launcher and mirrors has been reconfigured. A new collector was mounted for the internal mode converter experiment. This setup allows us to compare results directly from the axial configuration. The design parameters for the internal mode converter configuration are shown in Table 5.3. A photo of the experiment with the author of this thesis is shown in Fig. 5-29.

In order to check the output beam shape, a 3D motorized data acquisition radiation scanner was used, as shown in Fig. 5-30. The scanner was developed by former student P. Borchard at MIT [68]. Radiation from the gyrotron is picked up by a WR-6 horn antenna and detected by a WR-6 detector. A remotely controllable and programmable variable attenuator measures the amplitude of the radiation. It is programmed on a PC so that a set value of input power has to be achieved by adjusting the attenuation automatically. Once the set value of attenuation is met the final attenuation value is acquired and recorded.

Power and frequencies were also measured by the same methodology as in the

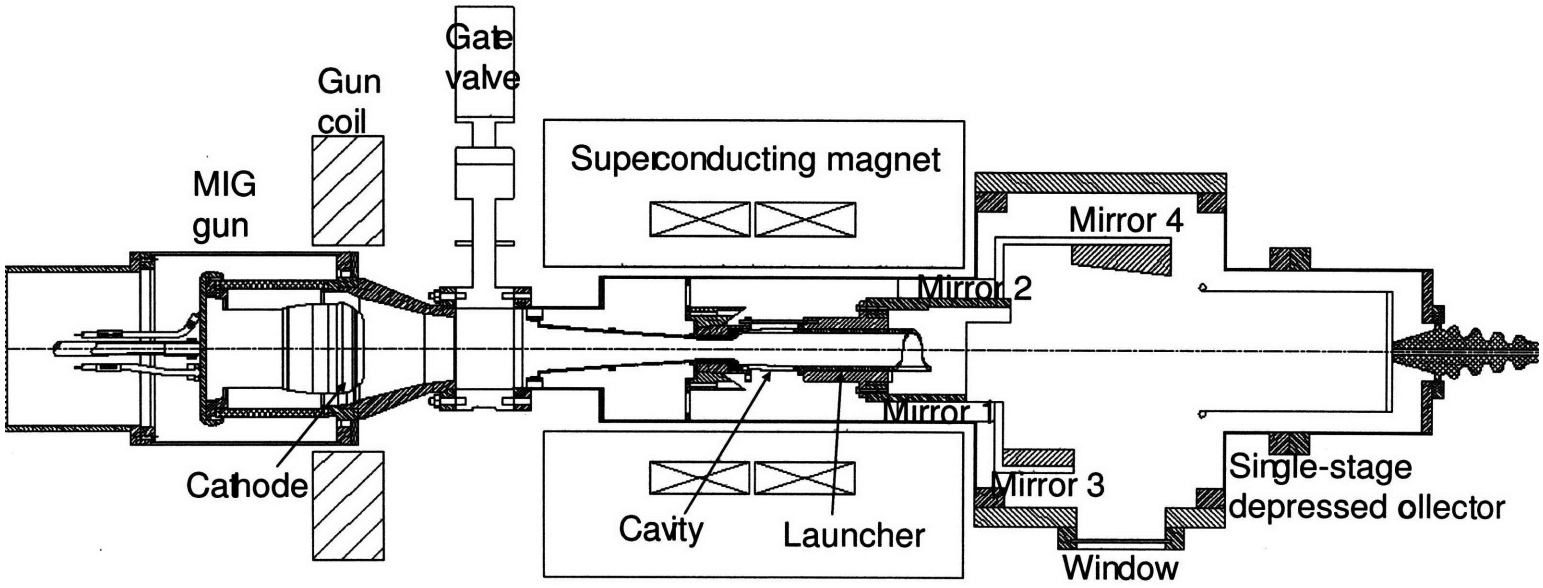

Figure 5-28: The 1.5 MW, 110 GHz gyrotron schematic in the internal mode converter configuration.

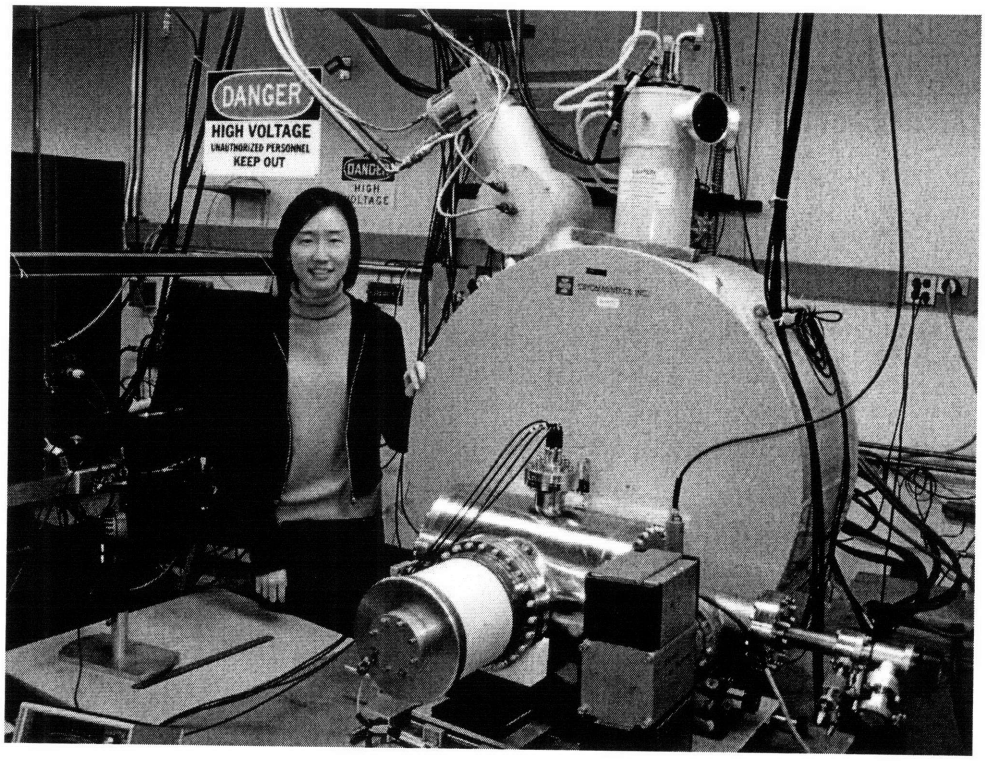

Figure 5-29: A picture of the gyrotron in the internal mode converter configuration.

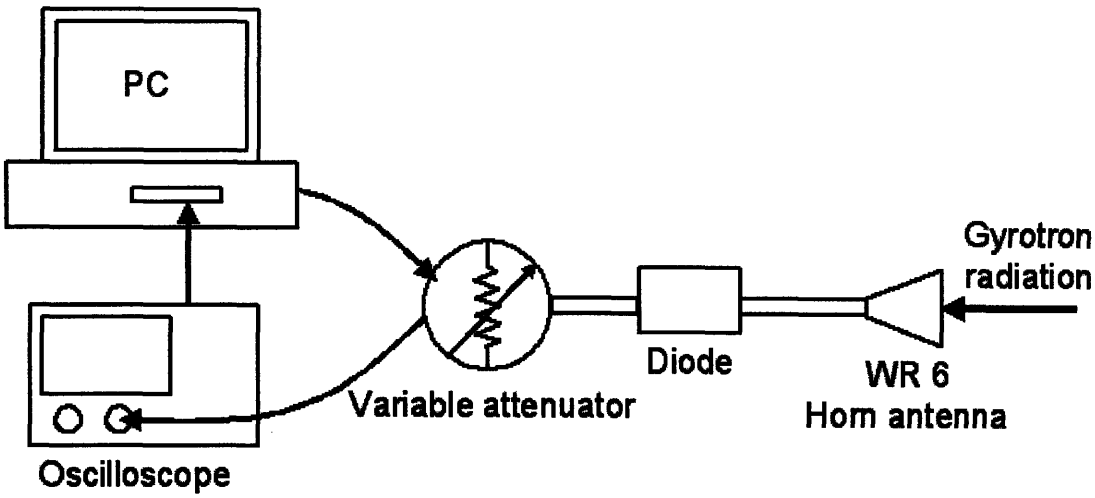

Figure 5-30: A schematic of the 3D auto scanner.

axial configuration experiment.

5.4.2 Experimental Results

Radiation patterns

The radiation pattern measurement is the most important diagnostic in the internal mode converter experiment. The gaussian beam waist is determined by this measurement. Liquid crystal paper provides a quick and sensible way to qualitatively verify gyrotron output beam radiation at the first stage of measurement. Liquid crystal paper reacts to relative temperature rises. Fig. 5-31 shows the result of a liquid crystal measurement. The liquid crystal paper is attached right in front of the gyrotron window operating at V_k=98 kV and I=41 A at B=4.39 T. The colors of liquid crystal change from black at the coldest temperature through red and green with increasing temperature and finally reach indigo at the warmest. In Fig. 5-31, the white circle overlaid on the liquid crystal paper represents the gyrotron window boundary whose diameter is 9.652 cm. From the liquid crystal measurement, we learn that the beam shape is fairly round in one peak, and offset from the window center by 2.2 cm. The liquid crystal paper measurement therefore is useful for aligning the output radia-

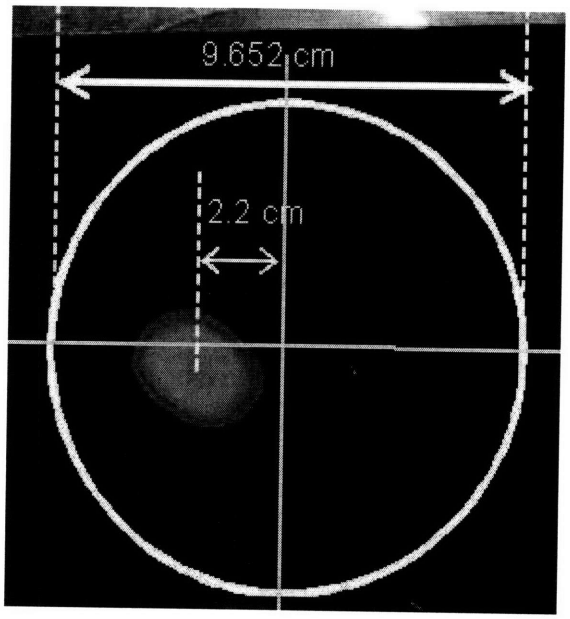

Figure 5-31: A beam pattern obtained by liquid crystal paper.

tion. Although the beam was designed to be centered on the window, the measured 2.2 cm offset is not a problem for these experiments since the output window was made intentionally much larger than the Gaussian beam size.

A more detailed measurement on the output radiation is necessary, however, to study the output radiation characteristics. The 3D motorized detector has been used. We measured the 2D radiation pattern at different planes far from the gyrotron window because the power of the output beam could easily exceed the power limit on the diode detector. By measuring the radiation pattern at different locations, we can extrapolate the Gaussian beam waist size at the window position. Fig. 5-32 shows the output beam pattern measured by the scanner located at 73.6 cm away from the window at an operating voltage of 84 kV and current of 36.3 A. The horizontal axis represents the axis parallel to the gyrotron and the vertical axis represents the perpendicular direction to the gyrotron axis at a fixed microwave output beam axis. The center of the graph is the beam center. The resolution of the scanner was set at 2.5 cm. The 2D beam scan measurement result yields a highly Gaussian-like beam as shown in Fig. 5-32.

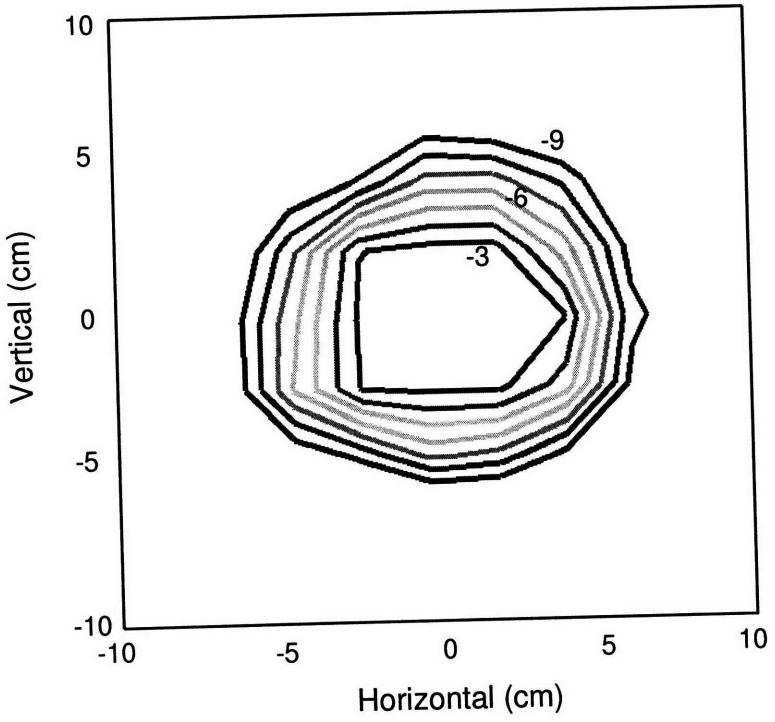

Figure 5-32: Plot of the measured power of the Gaussian-like output beam at 73.6 cm from the window location along the output beam axis. The contours represent the intensity of the beam in dB between 3 and 9 dB down from the peak. Horizontal: parallel to the gyrotron axis, Vertical: Perpendicular to the gyrotron axis.

In order to increase the resolution of the measurement, we scanned the beam in 1D in two orthogonal directions independently. Fig. 5-33 is the result of the 1D scans. The 1D scan measurement was also done at the same operating parameters as the 2D scan. The resolution of the 1D scan is 0.5 cm. The output beam pattern from the 1D measurement convinces us that the output beam of the gyrotron is a highly Gaussian beam as can be seen in Fig. 5-33.

Fig. 5-34 is the result of beam waist measurements at different locations from the window. The blue curve is the analytic result of the Gaussian beam expansion from Eq. 5.56, assuming that the beam waist at the window is 1.5 cm. Red circles and crosses are the measurement data. As shown in Fig. 5-34, the measured beam waist is in a good agreement with the analytic Gaussian beam expansion result.

Power measurement

The internal mode converter (IMC) experiment has been done by inserting the mode converter and changing the collector while maintaining all other parts (the electron gun, the beam tunnel, the gun magnet, the main magnet, and the cavity). This enables us to analyze the IMC experimental results directly and compare them to the axial configuration experimental results. We can estimate the IMC power loss by measuring the output power and comparing it with the axial configuration result. Fig. 5-35 is a typical oscilloscope trace for cathode voltage, collector current, RF diode signal and alpha trace. Fig. 5-36 shows the comparison of a plot of output power vs. magnetic field between the axial configuration and the IMC configuration. The maximum power in the IMC configuration is 1.5 MW at a cathode voltage of 96.6 kV and beam current of 42 A. Direct estimation by comparing the power result gives around (10±5) % internal mode converter loss. As inferred from cold test measurements by the University of Wisconsin [69], the percentage of power radiated from the launcher passing through window was 93 %. Therefore the present measurement of 90 % IMC efficiency is within experimental error of the cold test result. However considering the output beam offset shown in Fig. 5-31, the misalignment may partly explain the 10 % lower power in the IMC experiment.

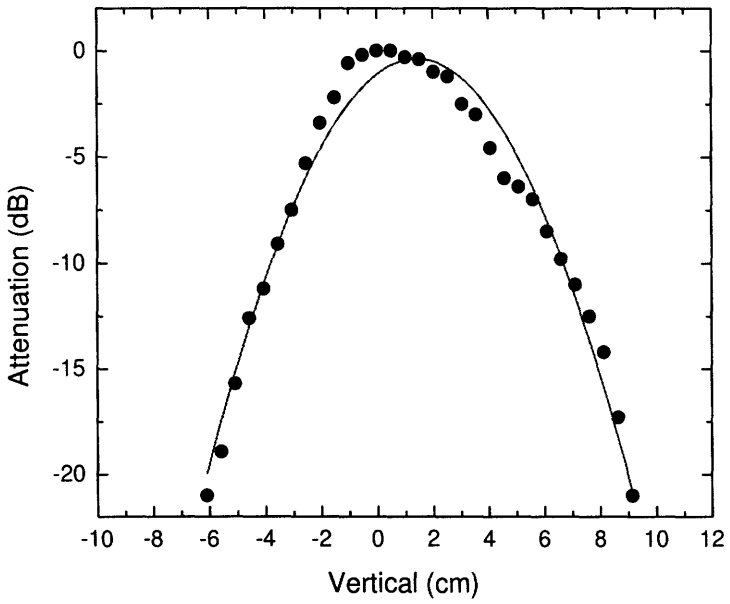

(a) Vertical scan

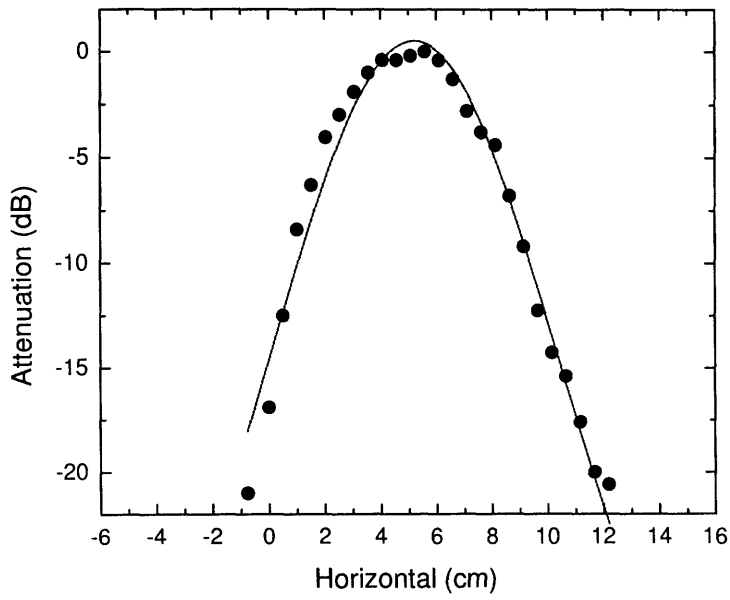

(b) Horizontal scan

Figure 5-33: A 1D beam scan

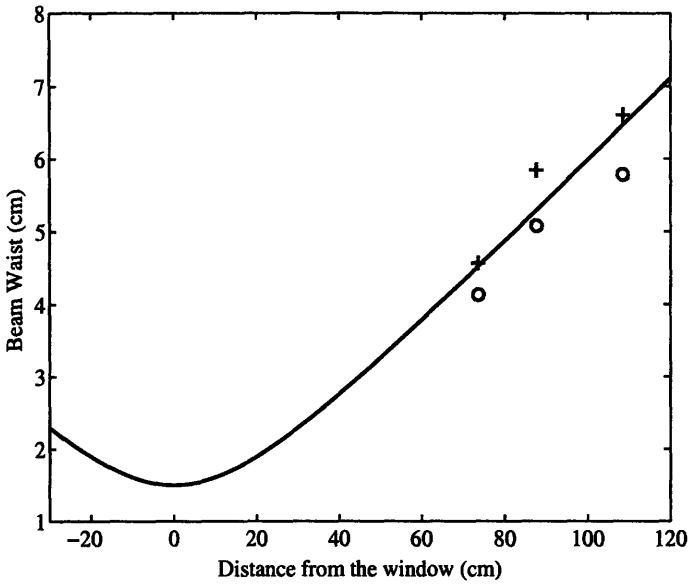

Figure 5-34: Output beam waist measurements at different locations from the window. Red crosses represent vertical beam waists and red circles represent horizontal beam waists. A blue curve is the fit to the Gaussian beam expansion.

Mode map

Fig. 5-37 is a plot of the mode map in the IMC configuration. A wide region of excitation for the $TE_{22,6}$ mode was observed. By changing the main magnetic field, other modes, such as the $TE_{21,6}$, the $TE_{20,6}$ and the $TE_{20,7}$, were excited. It is worthwhile to compare the mode map measurement from the IMC configuration to the axial configuration. Compared to Fig. 4-9, which is the mode map measurement in the axial configuration, the $TE_{22,6}$ mode region in the IMC configuration is extended to a wider excitation region in magnetic field. It can be interpreted that the edge region of the $TE_{22,6}$ mode (high main B field region) was affected by the satellite mode excitation due to window reflection of the satellite modes in the axial configuration. At a frequency of 110 GHz, we checked the reflection of the window using the VNA measurement and it was negligible. However, the start up scenario will be involved in the voltage ramp-up, during which the high frequency satellite mode will be excited first before the operating mode is excited. In this situation, the neighboring high

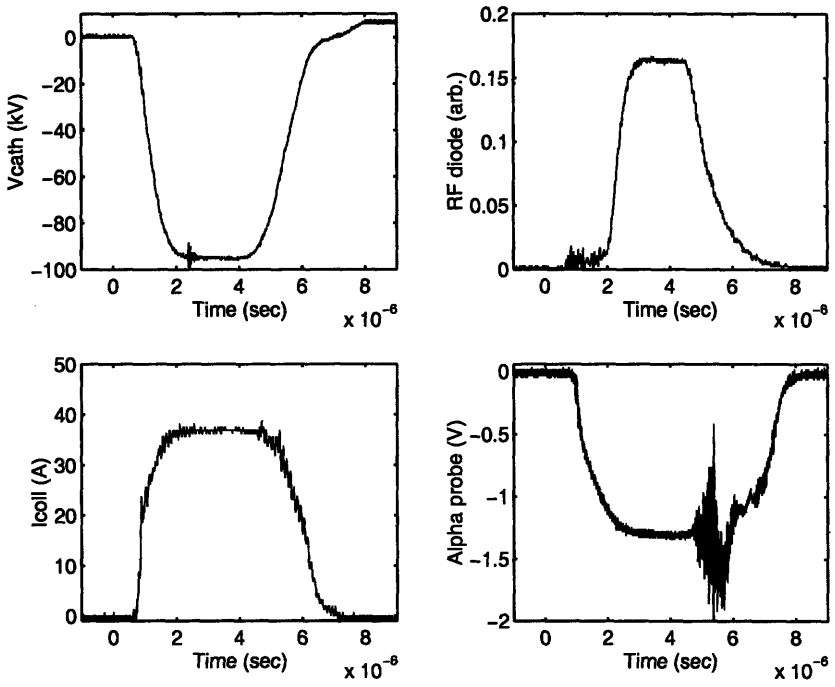

Figure 5-35: Oscilloscope traces for cathode voltage, collector current, RF signal and alpha probe signal.

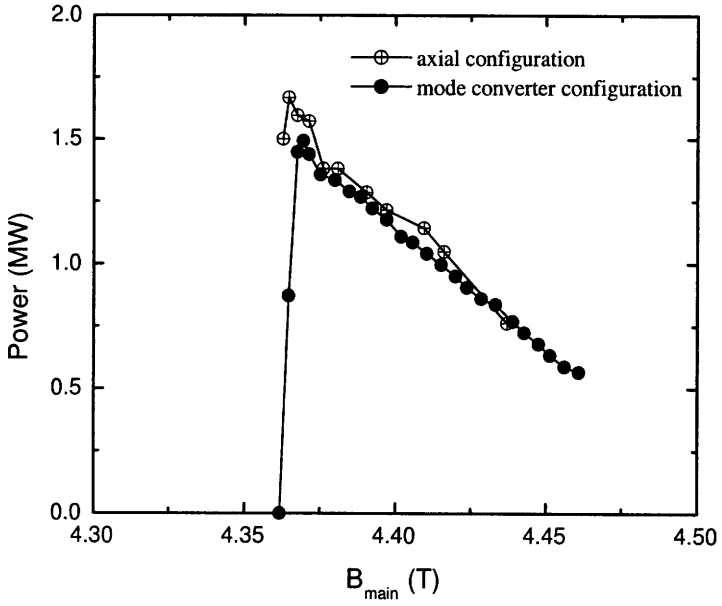

Figure 5-36: Power plot comparison between the axial configuration and the internal mode converter configuration as a function of main magnetic field.

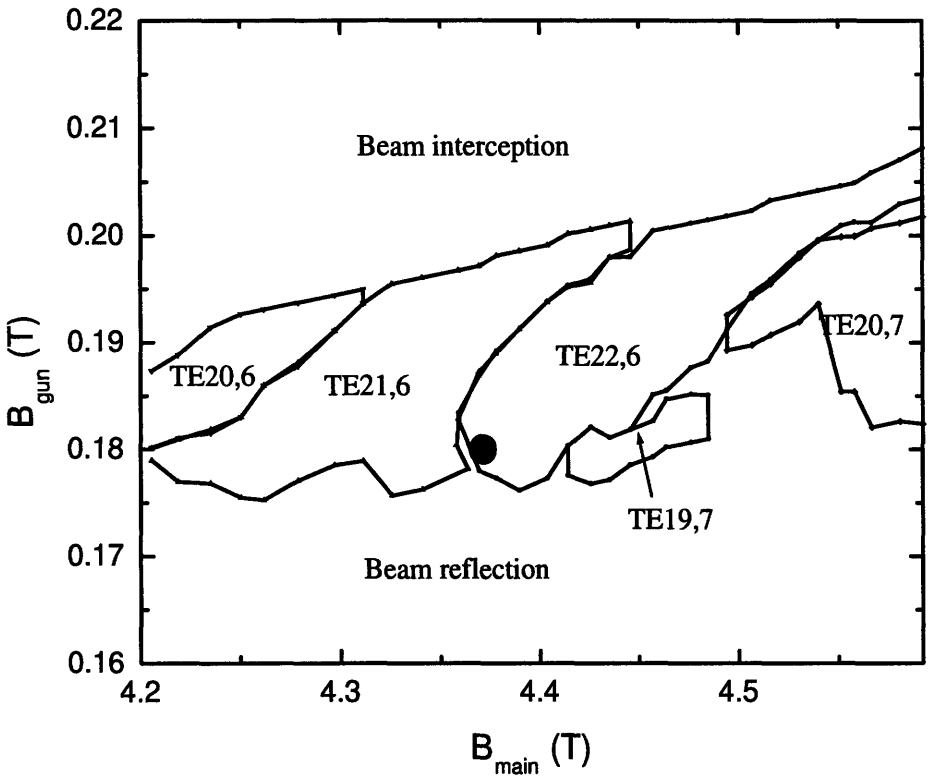

Figure 5-37: A mode map plot in the IMC configuration.

frequency mode such as the $TE_{20,7}$ mode or the $TE_{23,6}$ mode, which is at a different frequency than 110 GHz can be reflected from the window during the voltage ramp-up. At high main magnetic fields, window reflections will affect the mode competition between the operating mode and the high frequency satellite modes and result in increasing starting current of the operating mode. This explains why the excitation region for the $TE_{22,6}$ mode in the axial configuration has been reduced. Fig. 5-38 shows the comparison of the measured starting currents between the axial configuration and the IMC configuration. At high main magnetic fields, the starting current of the axial configuration is higher than that of the IMC configuration because of the excitation of the high frequency satellite modes, such as the $TE_{20,7}$ mode and the $TE_{23,6}$ mode.

The frequency pulling of the $TE_{22,6}$ mode was measured as a function of beam

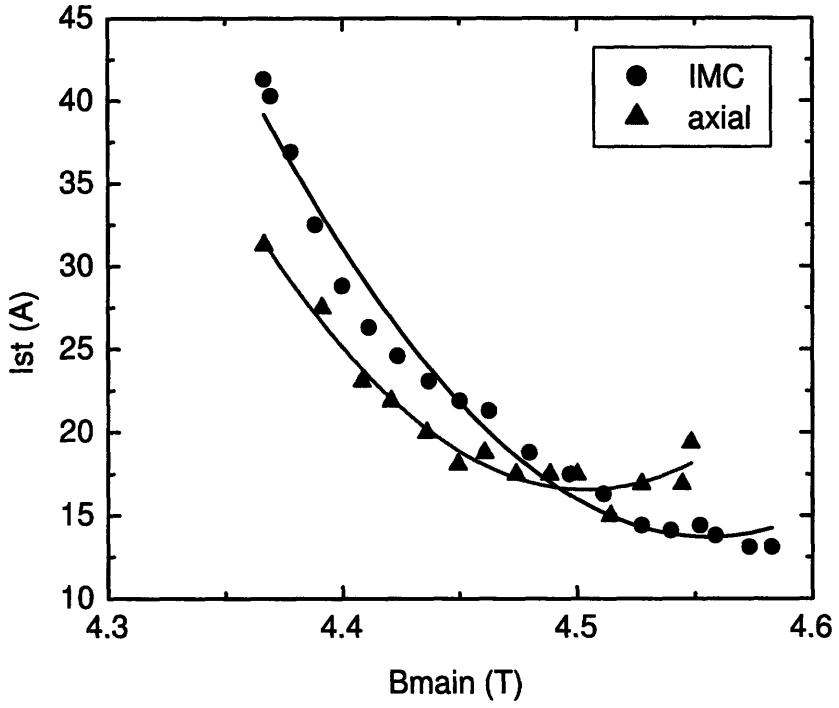

Figure 5-38: A measured starting current plot in the IMC configuration compared to the axial configuration. Circle: the IMC configuration, Triangle: the axial configuration

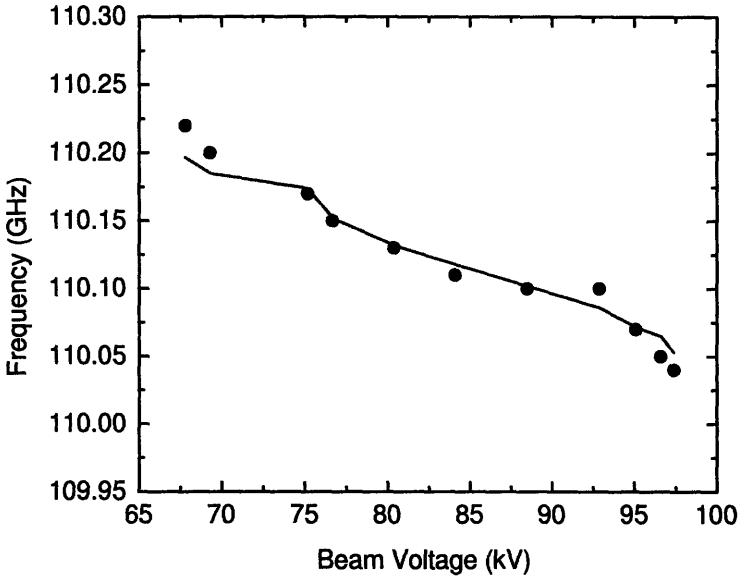

(a) Frequency pulling as a function of beam voltage, V_k

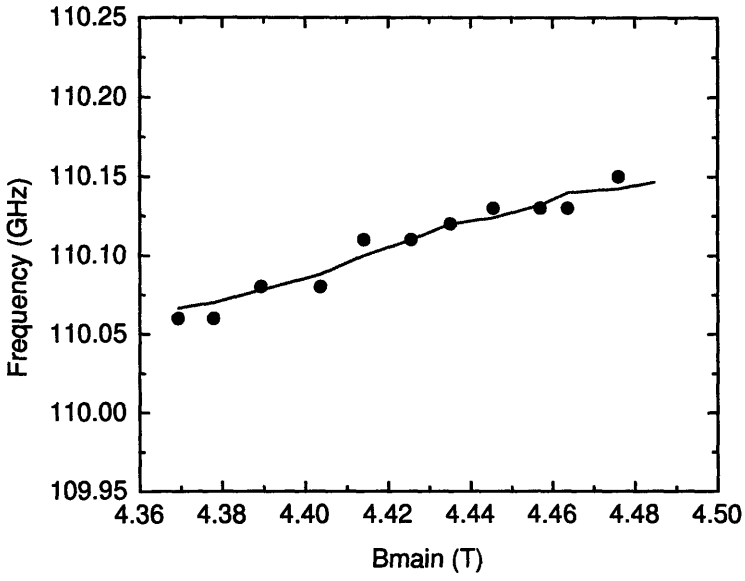

(b) Frequency pulling as a function of main B field

Figure 5-39: Frequency pulling plots

voltage and main magnetic field, and the results are shown in Fig. 5-39. A frequency variation of around 200 MHz over a beam voltage change of 30 kV was measured. A 100 MHz frequency pulling was measured for about a 0.12 T magnetic field variation. As the beam voltage increases, the frequency decreases, which is simply predictable from the cyclotron frequency equation. As the magnetic field increases, therefore, the frequency increases since magnetic field is directly proportional to the cyclotron frequency.

5.4.3 Discussion of Results

The internal mode converter is a key part in high power gyrotrons for converting a high order mode into a Gaussian mode. We have conducted experiments in the internal mode converter configuration, which consists of the launcher and the mirror system developed at MIT. The measured power can be directly compared to the axial configuration result since all parts except for the IMC and the collector remained the same in both configurations. From a direct comparison, the IMC efficiency was estimated to be 90 %. The 2D output beam shape was measured using the 3D motorized scanner and the output beam was a highly Gaussian-like shape, though the position of the output beam at the window was not on the center of the window. The mode map was measured and compared to the axial configuration result. A wide and stable region of operation of the $TE_{22,6}$ mode was observed.

Chapter 6

A Single-Stage Depressed Collector

6.1 Introduction

Depressed collectors allow a major efficiency enhancement in gyrotrons. Gyrotrons convert electron rotational energy into microwave energy. This intrinsically limits the gyrotron's overall efficiency because the parallel energy of electrons is not involved in the interaction mechanism. The idea of the depressed collector is to recover the unused parallel kinetic energy of the electrons by means of applying potentials in the collector with respect to the main body. In this way, the spent electron beam can be decelerated, not only enhancing the overall efficiency greatly but also reducing the power loading on the collector to facilitate long-pulse operation and reduce the possibility of collector failure due to metal fatigue. With the collector at the same potential as the body of the tube, the electrons after interaction with the cavity will dissipate their energy on the collector as heat. By reducing the voltage on the collector with respect to the body, the electrons are decelerated and the heat on the collector is also reduced. The depressed collector scheme is not uncommon in microwave tubes, however, the realization of the depressed collector in gyrotron experiments was recently done [70]. There is a lack of comprehensive study on depressed collectors in gyrotrons due to the difficulty of performing sophisticated experiments.

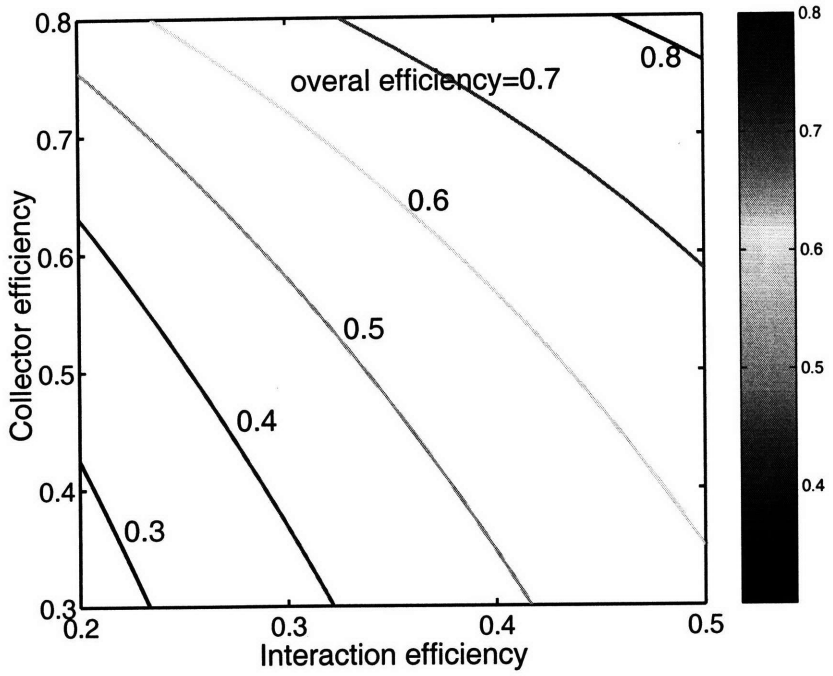

Figure 6-1: Efficiency relationship plot

The total efficiency relationship can be straightforwardly expressed by

$$\begin{aligned} \eta_{total} &= \frac{P_{RF}}{P_{beam} - P_{recover}} \\ &= \frac{\eta_{imc}\eta_{int}}{1 - \eta_{coll}(1 - \eta_{int})} \end{aligned} \tag{6.1}$$

where η_{int}, η_{imc}, and η_{coll} designate the interaction efficiency, the internal mode converter efficiency and the collector efficiency, respectively and P_{RF}, P_{beam} and $P_{recover}$ represent the output RF power, the beam power and the recovered power, respectively. Fig. 6-1 is the plot of the efficiency relationship. The overall efficiency is plotted as a function of interaction efficiency and collector efficiency. At a fixed interaction efficiency, an increase of 10 percentage points in collector efficiency leads to a gain of 5 percentage points in overall efficiency. Therefore the depressed collector can greatly increase the overall efficiency.

The concept of depressed collectors can be understood from the power supply

connection configuration shown in Fig. 6-2. Here, the body section contains a beam tunnel, a cavity and a mode converter which are all considered to be the anode. Fig. 6-2(a) shows a configuration without a depressed collector. It has a common power supply with a collector at ground potential. The beam current, I_{beam}, is equal to $I_{body} + I_{coll}$. The body current, I_{body}, is always much less than I_{coll}, usually less than 0.1 %. If the output RF power is P_{RF} the efficiency can be expressed as

$$\eta = \frac{P_{RF}}{V_c I_{beam}}.$$

The same ground potential schematic on the collector with separate power supplies is shown in Fig. 6-2(b). The total power supplied to the tube is the same as in Fig. 6-2(a) and the efficiency is still the same. However there are two power supplies. One supply is a regulated power supply for the body whose power is $V_c I_{body}$ and the other one is the collector power supply whose power is $V_c I_{coll}$. There is no energy recovery in either configuration. Now let's imagine that the voltage of the collector power supply decreases from V_c to V_{coll} while the regulated power supply remains the same. The current provided by this power supply is still I_{coll}. The output RF power is therefore the same as P_{RF}. Now the efficiency becomes

$$\eta = \frac{P_{RF}}{V_c I_{body} + V_{coll} I_{coll}}. \tag{6.2}$$

Eq. 6.2 gives the efficiency enhancement by reducing the voltage of the collector below the body, which results in slowing down the electrons after the body and before the collector. We should keep in mind that the output RF power is not changed at all in the depressed collector scheme. What makes the efficiency enhancement in depressed collectors is the decreased input power from the power supplies by having two separate power supplies.

For a better understanding, Fig. 6-3 shows possible circuits for a single-stage depressed collector. The beam voltage (cathode to anode voltage) is 96 kV, the collector current is set at 40 A, and the body current is 10 mA. Assuming the RF output power to be 1.5 MW and the collector voltage depression to be 26 kV, the

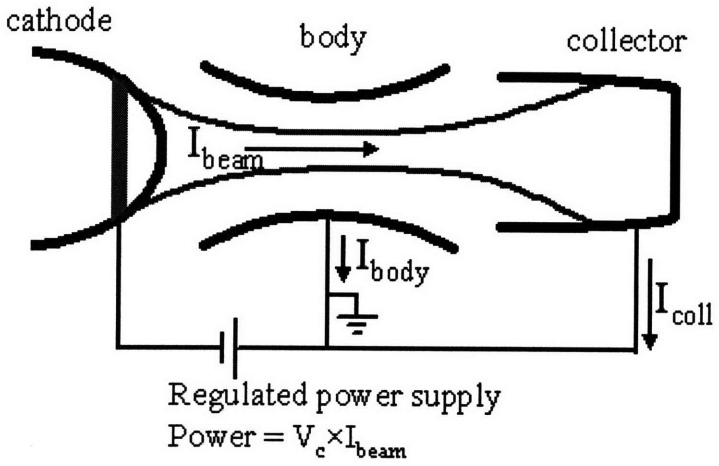

(a) Common power supply

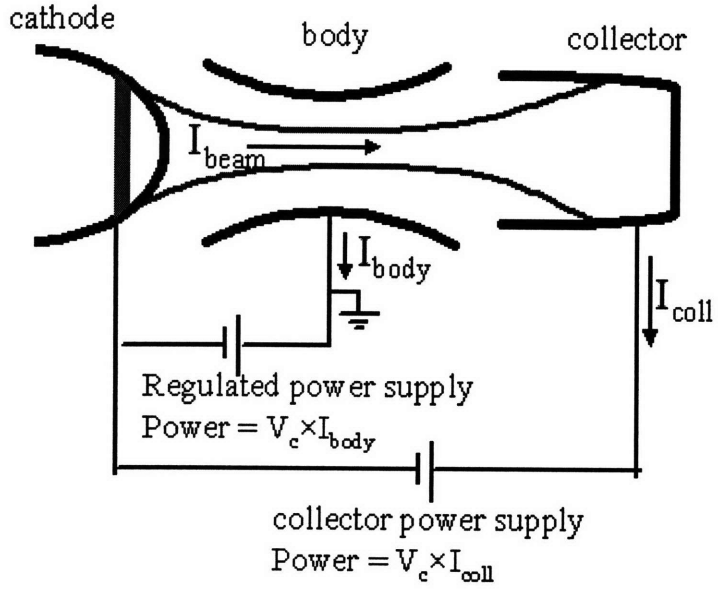

(b) Separate power supply

Figure 6-2: Power supply configuration for collectors at ground potential.

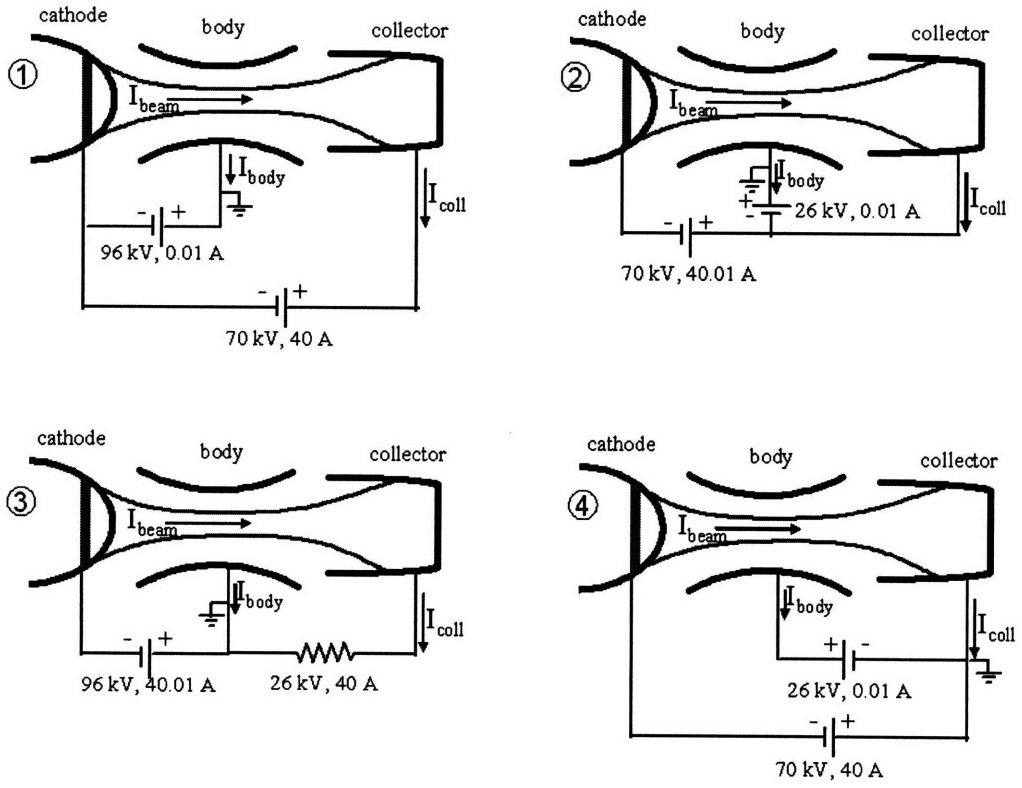

Figure 6-3: Circuit diagrams for a single-stage depressed collector

overall efficiency for all circuits (1-4) is

$$\eta = \frac{1.5\ MW}{70\ kV \times 40\ A} = 53.6\ \%. \tag{6.3}$$

This may be compared to the efficiency without a depressed collector, which is

$$\eta = \frac{1.5\ MW}{96\ kV \times 40\ A} = 39\ \%. \tag{6.4}$$

The single-stage depressed collector (Eq. 6.3) enhances the overall efficiency greatly. Circuit 1 in Fig. 6-3 has a regulated 960 W power supply and 2.8 MW collector power supply. The input power therefore is reduced from 3.84 MW to 2.8 MW by utilizing the depressed collector concept. Circuit 2 of Fig. 6-3 also has almost 2.8 MW input power. The body is grounded and the collector is depressed by 26 kV with respect to the body. Some commercial gyrotrons use this circuit. In circuit 3, the recovered energy by the depressed collector goes to a resistive load, which is acting like a battery. This configuration is very convenient for pulsed experiments. For the single-stage experiment, we used circuit 3 in Fig. 6-3. Circuit 4 in Fig. 6-3 is the same as circuit 1, except that the collector is grounded in circuit 4. Commercial gyrotrons often use this circuit because the collector is at ground potential, which is safer.

The efficiency of a depressed collector is strongly dependent on the depression voltage of the collector, which is indicated from Eq. 6.2. The collector can be depressed until the body current starts to appear, which indicates some of electrons are reflecting back to the tube. The maximum voltage that can be applied to a depressed collector is the minimum energy of the electron spent beam. This is more clearly shown in Fig. 6-4. The collector current is plotted as a function of depression voltage of the collector. V_{crit} represents the critical collector voltage above which some of the spent electron beam is reflected back to the tube, resulting in the appearance of body current. Therefore V_{crit} is the maximum depression voltage of the collector that corresponds to the minimum energy of the spent beam. The area of $V_{crit}I_{coll}$ is the power that is recovered by a single-stage depressed collector. The efficiency of a single-stage depressed collector highly relies on the energy distribution of the

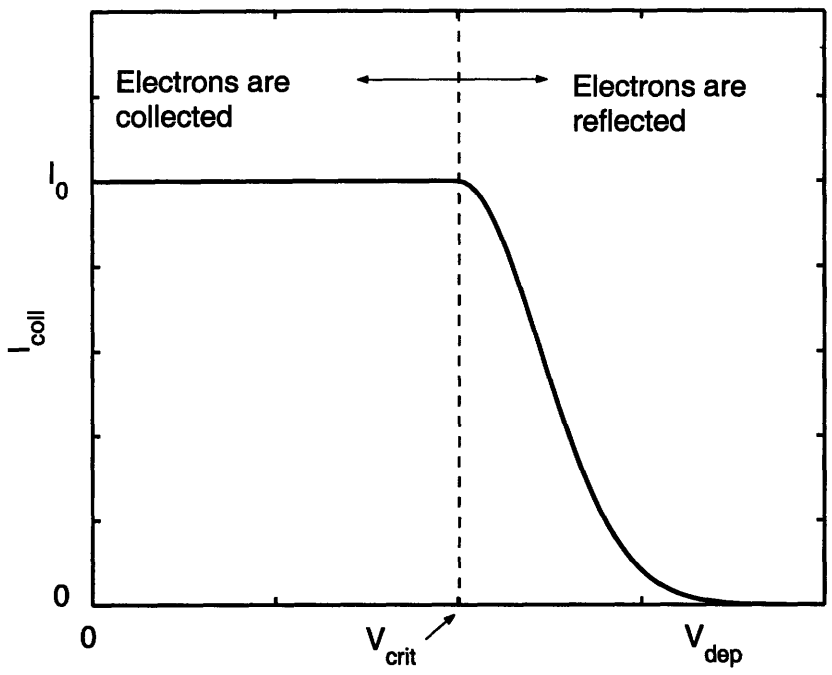

Figure 6-4: A collector current as a function of the magnitude of the collector voltage.

spent beam after interaction in the cavity. In a single-stage depressed collector, the depression voltage of the collector is passively determined already from the spent beam distribution. However, multi-stage depressed collectors can actively control the depression voltages at each stage by sorting the spent beam onto each collector plate. A multi-stage depressed collector will be discussed later.

6.2 Experimental Results

As mentioned in Section 6.1, circuit 3 demonstrated in Fig. 6-3 is the configuation used in this experiment.

Fig 6-5 shows a photo of the single-stage depressed collector. The collector is a copper cylinder with a diameter of 13.72 cm and length of 19.69 cm. A series of resistors was used to vary the depression voltage, as shown in Fig. 6-6. The depressed collector circuit consists of thirteen disc resistors, 26 Ω each, two carbon resistors,

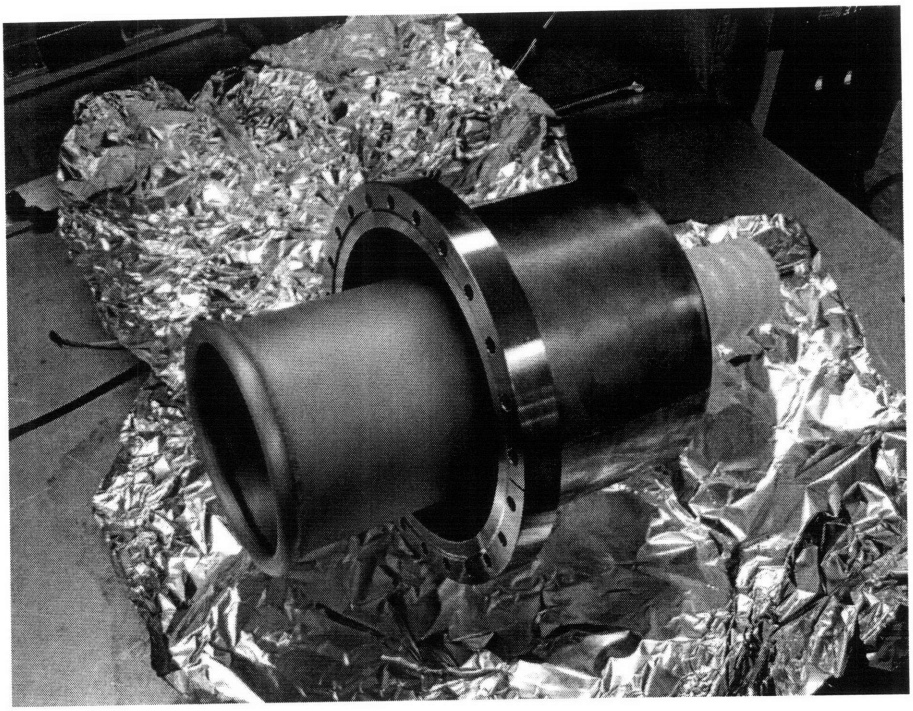

Figure 6-5: A photo of the single-stage depressed collector.

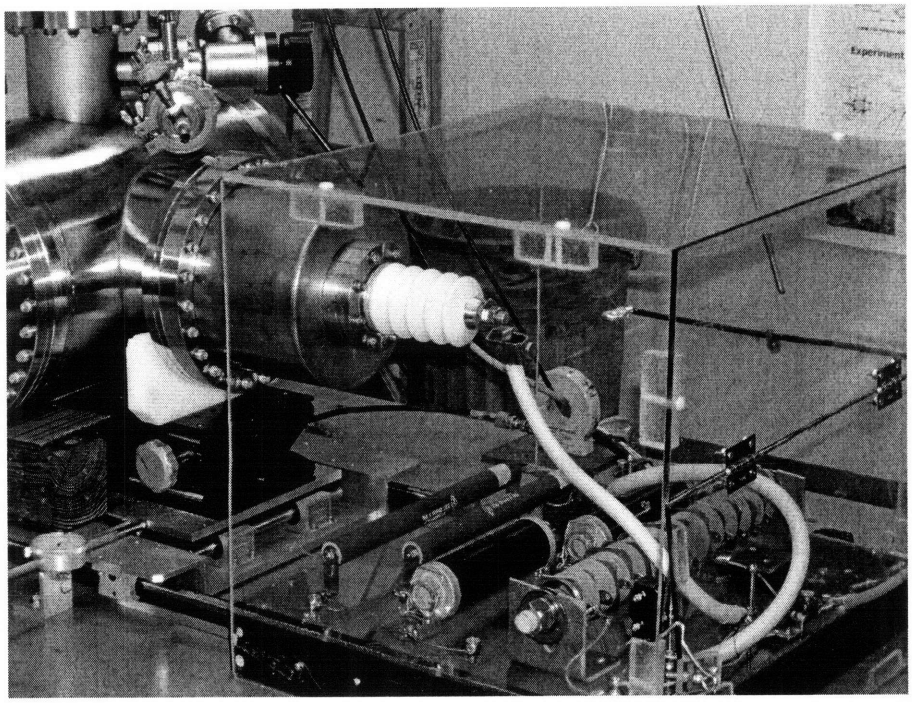

Figure 6-6: A photo of the single-stage depressed collector circuit setup.

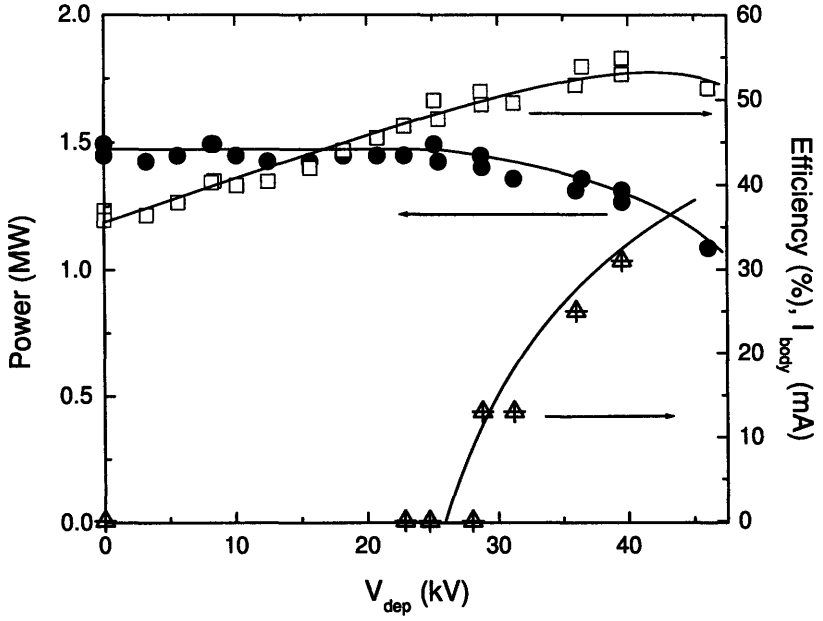

Figure 6-7: Power, efficiency and body current measurements as a function of depression voltage of the collector. Solid circles: output power, open squares: an efficiency plot and open triangles: a body current plot.

89 Ω each, and two 160 Ω carbon resistors, which allow for a maximum of around 35 kV voltage depression at collector current of 42 A. The ceramic feedthrough shown in Fig. 6-6 at the end of the collector is rated for 45 kV.

The experimental result is shown in Fig. 6-7. Power, efficiency and body current are plotted as a function of collector depression voltage. The output power is stable at 1.5 MW up to a depression voltage of 25 kV without the appearance of body current. The achieved efficiency at this depression voltage is 50 %. As the depression voltage exceeds 25 kV, the body current starts to appear and the power accordingly drops slightly. However, the efficiency continues to increase up to 55 % at an output power of 1.3 MW and depression voltage of 40 kV.

The applicable maximum depression voltages are measured as a function of beam

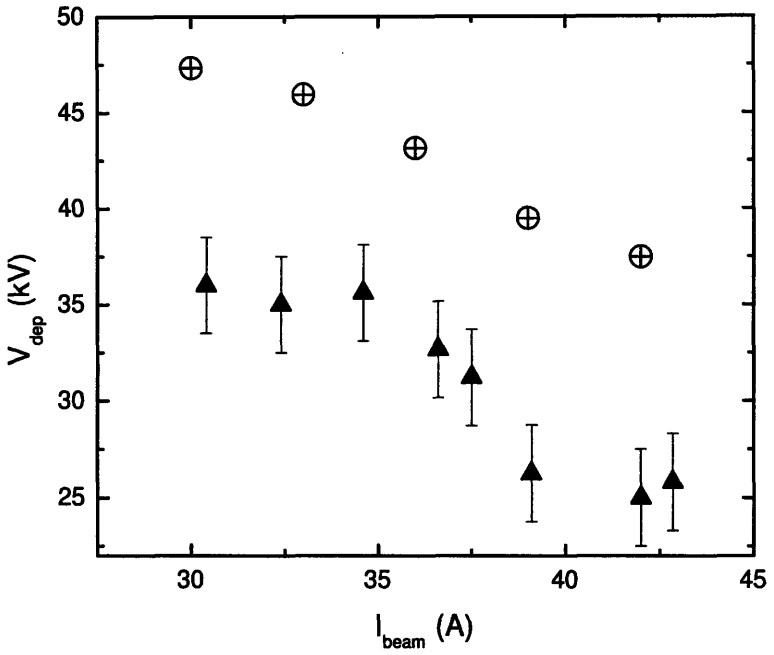

Figure 6-8: The voltage threshold of the collector depression as a function of beam current at a 96.6 kV beam voltage. Triangles with error bars represent experimental measurements and crossed-circles represent the simulation results.

current in Fig. 6-8 and compared to the MAGY simulation results. The applicable maximum depression voltages were determined by measuring the onset of body current. Experimentally, a 25 kV depression voltage was the limit at 42 A and 96.6 kV, whereas simulation predicts that depression up to 37.5 kV is possible.

6.3 Analysis

It is of importance to analyze the experimental results of the single-stage depressed collector shown in Fig. 6-7 and Fig. 6-8 to understand the underlying physics of the depressed collector gyrotron.

Based on the simulation results, a maximum voltage depression of 37.5 kV on the collector is predicted, which results in an overall efficiency of 60 %. Compared to the maximum depression voltage value of 25 kV in experiment, the overall efficiency would be greatly increased by 10 % efficiency points if the theoretical value of depression voltage could be applied. Therefore, understanding the discrepancy between the experiment and the theory is the key for efficiency enhancement.

It has been pointed out recently by some scientists that a significant interaction between the beam and wave can occur in the region after the cavity, an interaction designated as the "aftercavity" interaction (or cyclotron reabsorption) [71, 72]. Generally the interaction of an electron beam with a wave of a certain waveguide mode takes place in the region of a cavity where the oscillation frequency ω is close to the cutoff frequency ω_{cutoff} of the waveguide in the gyrotron. In the region after the cavity, the wave starts to become a traveling wave and the interaction stops. Therefore the efficiency does not depend on the longitudinal coordinate, z, any more after the electrons pass through the cavity. In most gyrotron simulations, the calculation for an interaction in a cavity stops where the cavity geometry ends due to simulation constraints. It is possible, however, that an interaction between the traveling wave and the spent electron beam after the cavity region could occur if the output transition has a small radial taper, as most high power gyrotrons do in an internal mode converter system in order to reduce mode conversion. The interaction that occurs

after the cavity can be a very serious problem for efficiency degradation because it will reduce the output power and will also result in a broadening of the energy distribution of the spent beam. The aftercavity interaction, therefore, strongly affects the overall efficiency of a single-stage depressed collector. Zapavelov et al. simulated a 170 GHz gyrotron operating in the $TE_{25,10}$ mode and estimated the reduction in efficiency due to the aftercavity interaction to be 8-10 percentage points [71].

The gyrotron design code, MAGY is used for analyzing our results. The energy distribution of the spent beam is critical in determining the threshold of depression voltage of the collector because the electrons with the minimum energy will be reflected if the applied depression voltage on the collector is greater than that minimum energy. The distribution is to be calculated considering the interaction in the cavity. The analytic estimation for the condition of synchronism can be calculated from the following equation [71],

$$\omega - n\Omega_c \approx k_z v_z \tag{6.5}$$

where ω is the wave frequency, n is the harmonic number, and Ω_c is the electron cyclotron frequency. The electronic efficiency can be expressed as

$$\eta_{elec} = \frac{\gamma_0 - \gamma_f}{\gamma_0 - 1} \tag{6.6}$$

where γ_0 is 1+V_k(keV)/511(keV) and γ_f is the final relativistic constant, $\gamma_f = (1 - \beta_f^2)^{-1/2}$. With a given initial α_0, β_{z0} and $\beta_{\perp 0}$ can be obtained. $\beta_{\perp f}$ is now calculated from β_f assuming β_{z0} is constant. Therefore after the interaction in the cavity between the electron beam and the wave, assuming no aftercavity interaction, the perpendicular and parallel velocities of the spent beam are expressed as follows in accordance with the adiabatic invariant,

$$\beta_\perp = \beta_{\perp f}\sqrt{\frac{B(z)}{B_{0,max}}}, \qquad \beta_z = \sqrt{\beta^2 - \beta_\perp^2}. \tag{6.7}$$

The cyclotron frequency, Ω_c is now expressed with a tapered magnetic field and

geometry,

$$\Omega_c = (\omega - \Delta\Omega_c)\left(\frac{\gamma_0}{\gamma_f}\right)\left(\frac{B(z)}{B_{0,max}}\right) \tag{6.8}$$

using $\Omega = \Omega_0\left(\frac{\gamma_0}{\gamma_f}\right)\left(\frac{B(z)}{B_{0,max}}\right)$ and $\Omega_0 = \Omega - \Delta\Omega_c$. Using Eq. 6.7 and Eq. 6.8, the cyclotron resonance condition, Eq. 6.5 is written as

$$1 - \left(1 - \frac{\Delta\Omega_c}{\omega}\right)\left(\frac{\gamma_0}{\gamma_f}\right)\left(\frac{B(z)}{B_{0,max}}\right) = \beta_z\left(1 - \left(\frac{r_c}{r(z)}\right)^2\right)^{1/2} \tag{6.9}$$

from equations of $k_\perp = \nu_{m,p}/r(z)$ and $k \simeq \nu_{m,p}/r_c$, where r_c is the cavity radius. Here $r(z)$ and $B(z)$ are the tapered geometry and tapered magnetic field after the cavity region. In our case, the location where the synchronism condition is satisfied can be calculated analytically using the above equation, Eq. 6.9. The accelerating beam voltage is 96 kV and therefore γ_0 is 1.1879. With an alpha of 1.3, $\beta_{\perp 0} = 0.4278$, $\beta_{z0} = 0.3291$. With the geometry of the V-2005 cavity and the launcher and the tapered magnetic field, the location where the synchronism condition is satisfied is $z \simeq 11$ cm.

Fig. 6-9 is the simulation result of the aftercavity interaction from MAGY. The geometry includes the V-2005 cavity and the launcher, which is slightly tapered. Mode conversion was checked at the launcher geometry by using the CASCADE code which calculates the coupled-mode equations of a given geometry [40]. There is no significant mode conversion after the cavity region so that the extracted power from the wave by the interaction with the beam directly affects the electron beam, and some electrons will be accelerated. The geometry and main magnetic field are plotted as a function of the longitudinal coordinate, z. The cavity ends at z=9.82 cm after which the launcher begins with a radius of 2.0955 cm. The length of the launcher is 15.4 cm with a taper angle of 0.3°. As shown in Fig. 6-9, the magnetic field tapers along z where the radius of the geometry is also tapered. The excited electric field amplitude of the $TE_{22,6}$ mode and the phase are plotted. After the interaction in the cavity, the wave starts to become a traveling wave, as indicated by the rapidly changing phase. The second plot of Fig. 6-9 is the output power as a function of z. The power starts

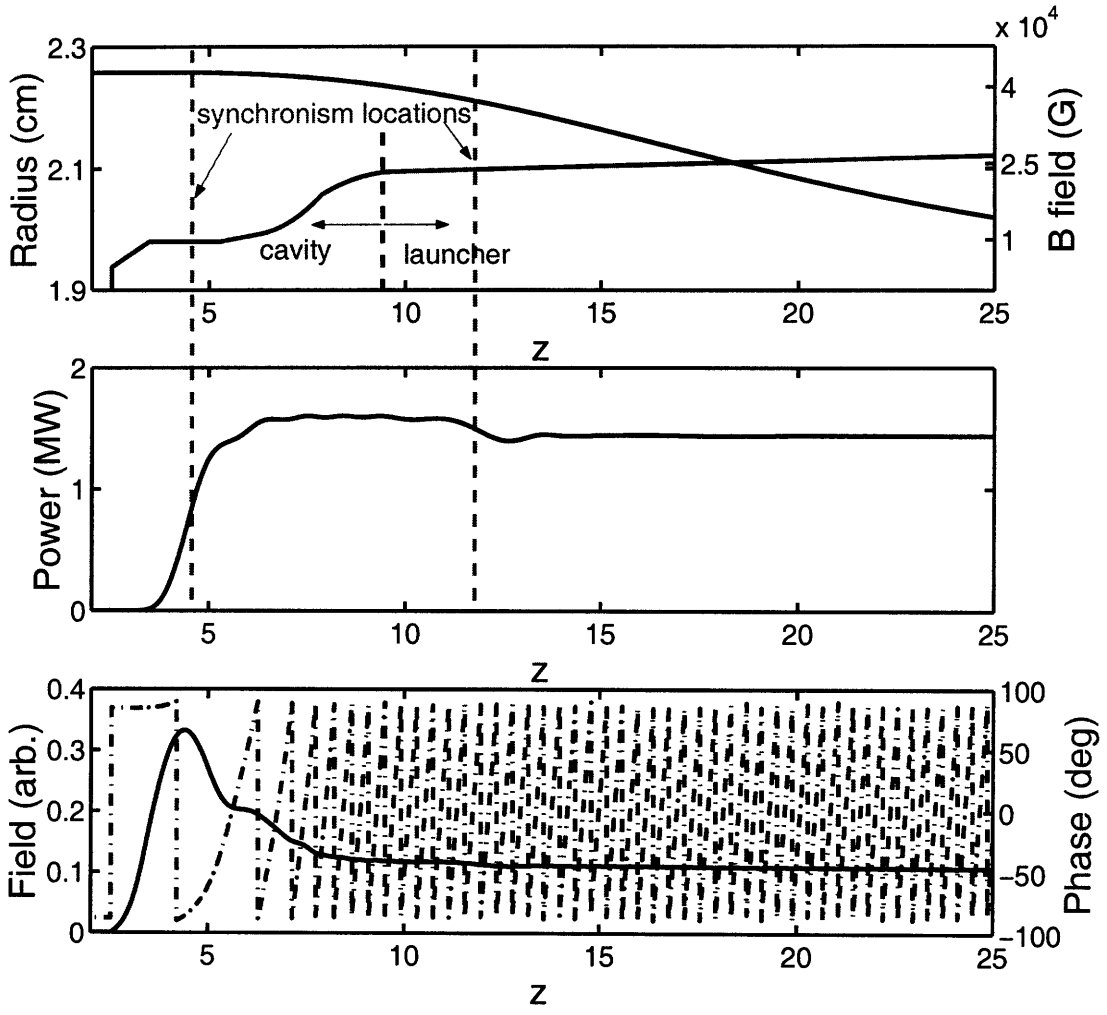

Figure 6-9: Geometry, main magnetic field, output power, and longitudinal field distribution of the $TE_{22,6}$ mode, and phase in the V-2005 cavity and the launcher, simulated by MAGY.

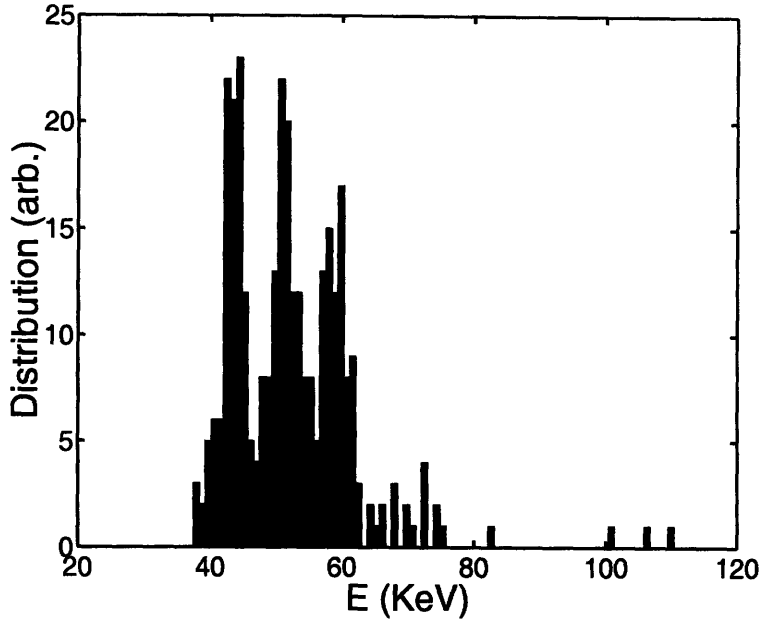

Figure 6-10: The simulated energy distribution of spent beam from MAGY at z=9.82 cm (the position of the cavity end).

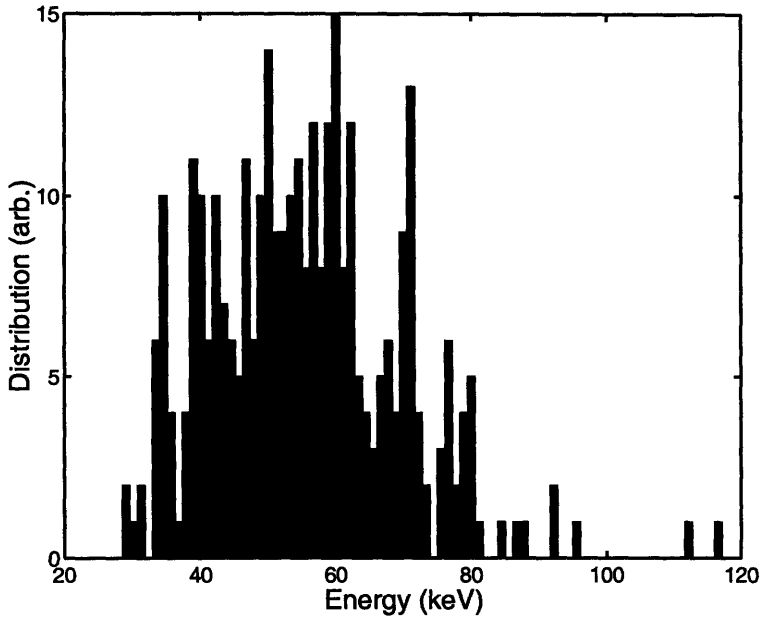

Figure 6-11: The simulated energy distribution of spent beam from MAGY at z=25.02 cm (the position of the launcher end).

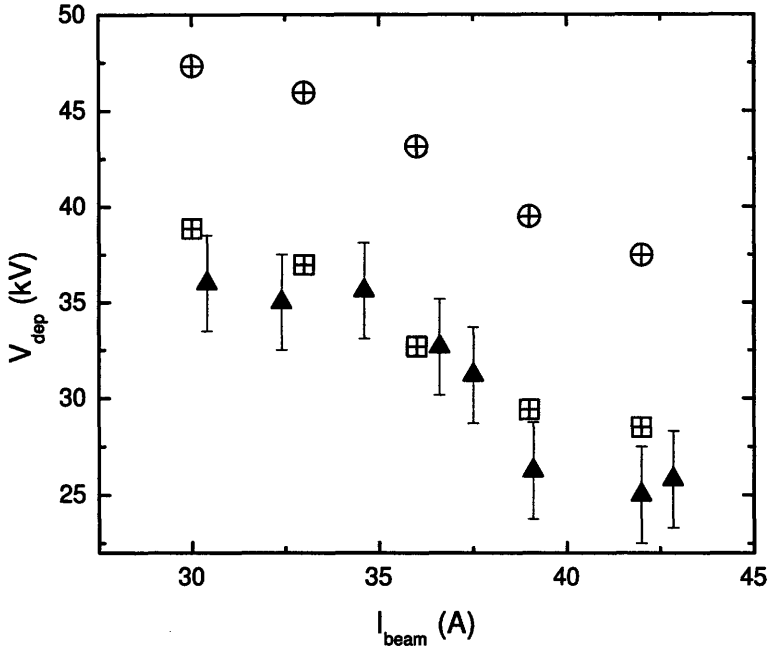

Figure 6-12: The voltage threshold of the collector depression as a function of beam current at 96.6 kV. The triangles with error bars represent experimental measurements and the crossed-circles and squares represent the simulated results without aftercavity interaction and the simulation results with aftercavity interaction, respectively.

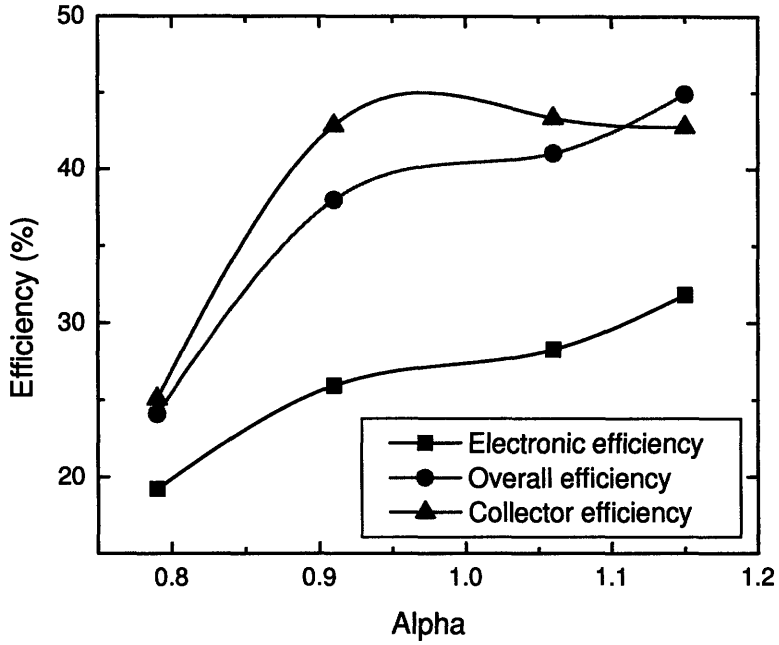

Figure 6-13: Experimental efficiency plot as a function of alpha values at a 96 kV cathode voltage and 40 A beam current.

to drop around $z \simeq$11-13 cm from 1.58 MW to 1.44 MW, corresponding to efficiencies of 39 % and 36 % respectively. The location of the efficiency falloff exactly matches the analytic calculation, which is z=11 cm. From the MAGY simulation results, the efficiency degradation is predicted at 3 cm from the beginning of the launcher.

The resultant energy distribution of the spent beam without including the aftercavity interaction, which means the simulation is stopped before the launcher begins, is simulated by MAGY and plotted in Fig. 6-10. A 7 % transverse velocity spread is included in the simulation. The voltage is 96 kV and the beam current is 42 A as in the experiments. The number of beamlets is 81. The output power is 1.58 MW at an alpha of 1.3. The minimum energy of the spent beam is 37.5 kV as shown in Fig. 6-10. When the aftercavity interaction is considered by including the tapered launcher, the energy distribution of the spent beam is in fact changed as shown in Fig. 6-11. It is broader than the distribution without the aftercavity interaction and the minimum energy of the spent beam is 28.5 kV whereas it is 37.5 kV in the case of not including the aftercavity interaction. The final results are plotted in Fig. 6-12 with and without consideration of the aftercavity interaction. The minimum energy of the spent beam estimated from the MAGY simulation with an allowance of the aftercavity interaction has an excellent agreement to the experimental result of 25 kV at 42 A beam current. As seen in Fig. 6-12, the simulation results including the aftercavity interaction, which are represented in cross-squares, show a perfect match with the experimental results at all beam current values, which indirectly indicates that the aftercavity interaction in fact does degrade the efficiency. Efficiencies are obtained as a function of alpha values in Fig. 6-13. The alpha values were varied by increasing the main and gun magnetic fields at a fixed beam voltage of 96 kV and beam current of 40 A. Due to the cathode emission problem, the collector current was not able to be increased more than 40 A which limited the maximum alpha value. A wide variation of alpha values were not achievable due to the intrinsic limitation of the diode gun and the V-2005 cavity, which was only designed for an alpha value of 1.4. The overall and electronic efficiencies drop as the alpha values are decreasing. However, the collector efficiency corresponds to a peak alpha value around 0.9 and

1.0 and begins to drop as the alpha increases. At an alpha value of 0.8, the collector efficiency significantly dropped.

6.4 Discussion of Results

A single-stage depressed collector has been successfully demonstrated. The efficiency plot shown in Fig. 6-7 as a function of the depression voltage of the collector shows the maximum efficiency is 50 % by depressing the collector by 25 kV. The efficiency of the single-stage depressed collector is 41 %. The discrepancy between the theory and the experiment in terms of the critical depression voltage that essentially is determined by the minimum energy of the spent beam is understood by the aftercavity interaction. From the study, it is found that a cavity tapered section and an internal mode converter have to be designed carefully in order to prevent the degradation of efficiency due to the aftercavity interaction. In fact, if the aftercavity interaction is avoided, more than 55 % overall efficiency is possibly obtainable. The aftercavity interaction between the traveling wave and the spent beam was observed in the MAGY simulation in our geometry. In order to eliminate the aftercavity interaction, either the magnetic field should have a wider flattop region or a combined redesign of the cavity and launcher should be considered. The ratio of the launcher entrance radius to the cavity radius (r_{output}/r_c) has to be greater than 1.2 (the ratio for the cavity and the launcher for our experiments was 1.06). Correspondingly, the launcher beginning radius has to be greater than 2.3 cm according to the MAGY simulation. The increase of the launcher radius is not trivial at all and results in a significant increase of the launcher total length. Therefore, shortening the launcher length with the increased launcher radius may be of great interest and may be a challenging future work.

6.5 Two-Stage Depressed Collector

The maximum efficiency of single-stage depressed collectors is limited due to the energy distribution of the spent beam. As discussed in Section 6.1, the minimum energy

of the spent beam determines the efficiency of the single-stage depressed collector. If the spent beam can be sorted as a function of energy so that most of the energy of the spent beam can be recovered, the efficiency will increase significantly. Multi-stage depressed collectors have been used for decades successfully in TWTs. TWTs are operated using a linear beam, which makes operation of multi-stage depressed collectors very easy by sorting the spent beam electrically [73]. In gyrotrons, the most challenging part in designing two-stage depressed collectors is to reduce the depressed collector size. It is inevitable to have a fairly large collector due to the presence of strong magnetic fields. Although the size can be a hurdle, efforts towards two-stage depressed collectors are worthwhile because the efficiency using a two-stage depressed collector will be greatly enhanced and the power loading on the collector is significantly reduced, making CW gyrotron operation more robust. Some recent results on the design of two-stage depressed collectors can be found in [74, 75, 76].

A key part in designing two-stage depressed collectors is to make the trajectory of the spent electron beam controllable by electric fields so that the spent electron beam can be sorted properly by applied depression voltages. Gyrating electrons in gyrotrons use roughly an alpha of 1.0-2.0 in normal operation. The intrinsically high perpendicular velocity impedes electrons from following the electrostatic fields. The perpendicular motion has to be converted to parallel motion to allow electrons to be guided by electrostatic fields.

There are two ways to decompress magnetic fields. One is simply to allow the magnetic field to decompress adiabatically. The other is a non-adiabatic decompression method.

6.5.1 Adiabatic decompression

Since magnetic fields are adiabatically decreasing towards the collector region the perpendicular motion of an electron is converted to parallel motion according to the following equation,

$$v_{\perp f} = v_{\perp i} \left(\frac{B_f}{B_i} \right)^{1/2} \tag{6.10}$$

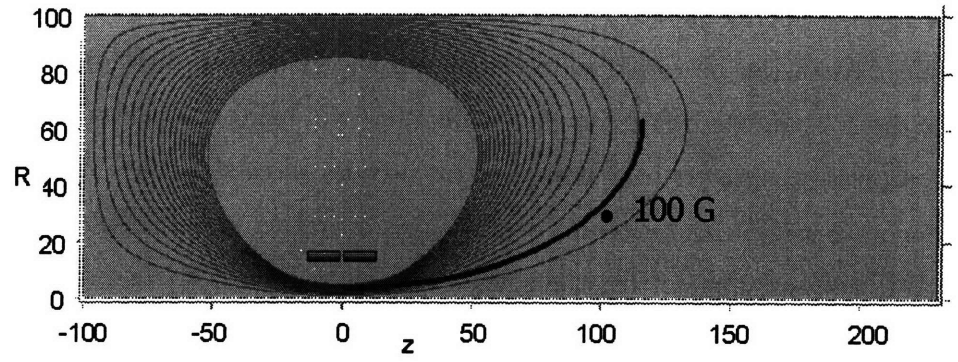

Figure 6-14: Magnetic field lines of the superconducting magnet. Pink lines represent magnetic fields. z=0 is the location of the cavity.

where $v_{\perp f}$ is the perpendicular velocity at the collector region where the magnetic field is B_f. $v_{\perp i}$ is the initial perpendicular velocity at the cavity where the magnetic field is B_i. For the 110 GHz, 1.5 MW gyrotron, the electron trajectory is simulated using the POISSON code with adiabatically decompressed magnetic fields from the superconducting magnet, as shown in Fig. 6-14.

The location of the 100 G magnetic field line is at z=100 cm, where z=0 is the cavity center. Therefore, if the simple adiabatic decompression is used, the two-stage depressed collector has a radius of 40 cm and a length greater than 60 cm.

6.5.2 Non-adiabatic decompression

As shown in the previous section, the size of the two-stage depressed collector is large if the adiabatic decompression of magnetic fields is utilized. In order to reduce the size of the geometry, a non-adiabatic magnetic field decompression is adopted. The magnetic field at the collector region changes abruptly so that the magnetic field suddenly drops to less than 100 G. In the 110 GHz, 1.5 MW gyrotron two-stage depressed collector design, a ferromagnetic piece is introduced for non-adiabatic decompression of the magnetic fields. The magnetic field line is altered suddenly by inserting the ferromagnetic piece, causing an abrupt drop in magnetic fields around the location of the iron piece. Fig. 6-15 is a plot of constant flux lines of the magnetic

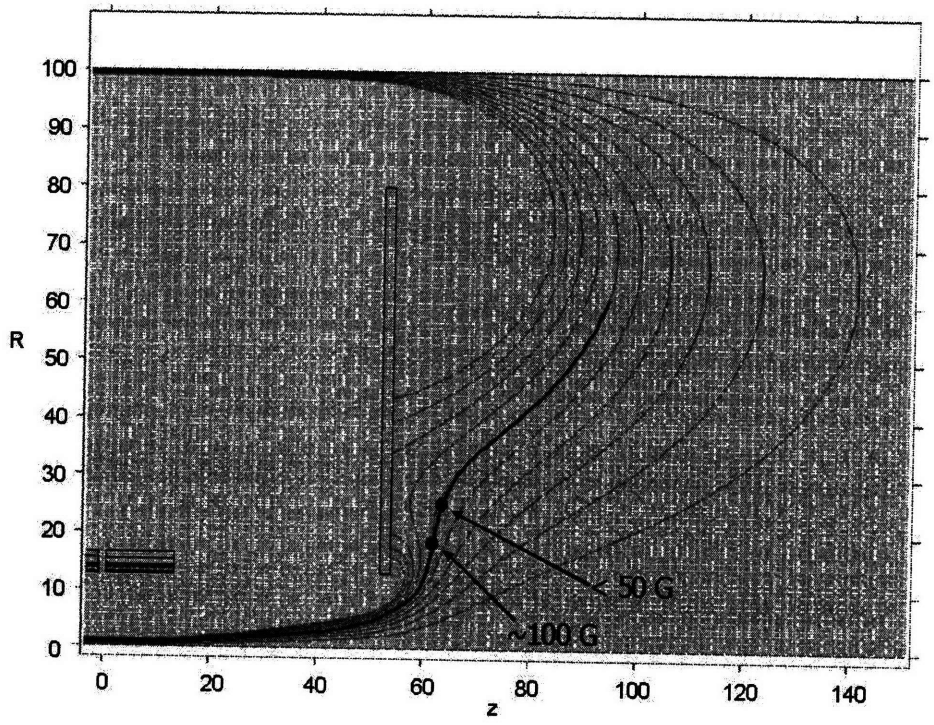

Figure 6-15: Magnetic field lines with an ferromagnetic iron piece. Pink lines represent magnetic fields. z=0 is the location of the cavity.

fields simulated using the POISSON code. As shown, the field abruptly drops from 100 G to 50 G around 60 cm from the cavity. The red line in the plot represents the trajectory of the electron beam.

The simulation of the two-stage depressed collector is done by the procedure shown in Fig. 6-16. The magnetic field lines are obtained using the POISSON code. The energy of the spent beam is simulated by the MAGY code with the V-2005 cavity. Finally, the electron trajectory from the cavity to the collector is simulated using the MICHELLE code by incorporating data of the determined magnetic field and the energy of the spent beam. The geometry of the two-stage depressed collector is optimized. The efficiency of the two-stage depressed collector is calculated by the MICHELLE code by applying depression voltages at the first collector plate and the

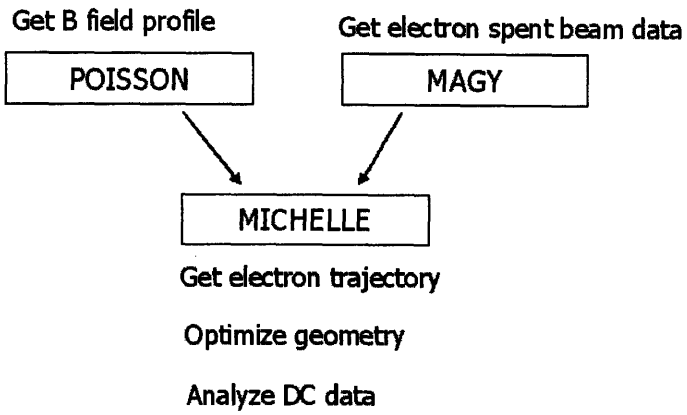

Figure 6-16: Flow chart for design of a two-stage depressed collector.

second collector plate. The reflected electrons are also monitored via calculation.

Fig. 6-17 shows the simulation result from the MICHELLE code. The geometry of the two-stage depressed collector is very compact. The radius of the collector is 30 cm and the length is 15 cm. The current is collected at collector plates. The collector current from the first collector plate is 3.1 A and from the second collector plate is 38 A. There is no reflected current. The collector efficiency from the geometry of Fig. 6-17 is 70 %, and the overall efficiency is 66 %. A significant efficiency enhancement is predicted from the simulation.

6.5.3 Conclusion

The design of a two-stage depressed collector has been investigated. Due to the strong presence of magnetic fields at the collector region, the size of the two-stage depressed collector is very large. In order to reduce the size of the collector, a non-adiabatic decompression of magnetic fields has been exploited by inserting a ferromagnetic iron piece near the collector region. The energy distribution of the spent beam was simulated in MAGY and implemented by the MICHELLE code for the simulation of the two-stage depressed collector. The geometry of the collector using the ferromagnetic iron piece is reduced greatly. The collector efficiency is predicted to be 70 % and the

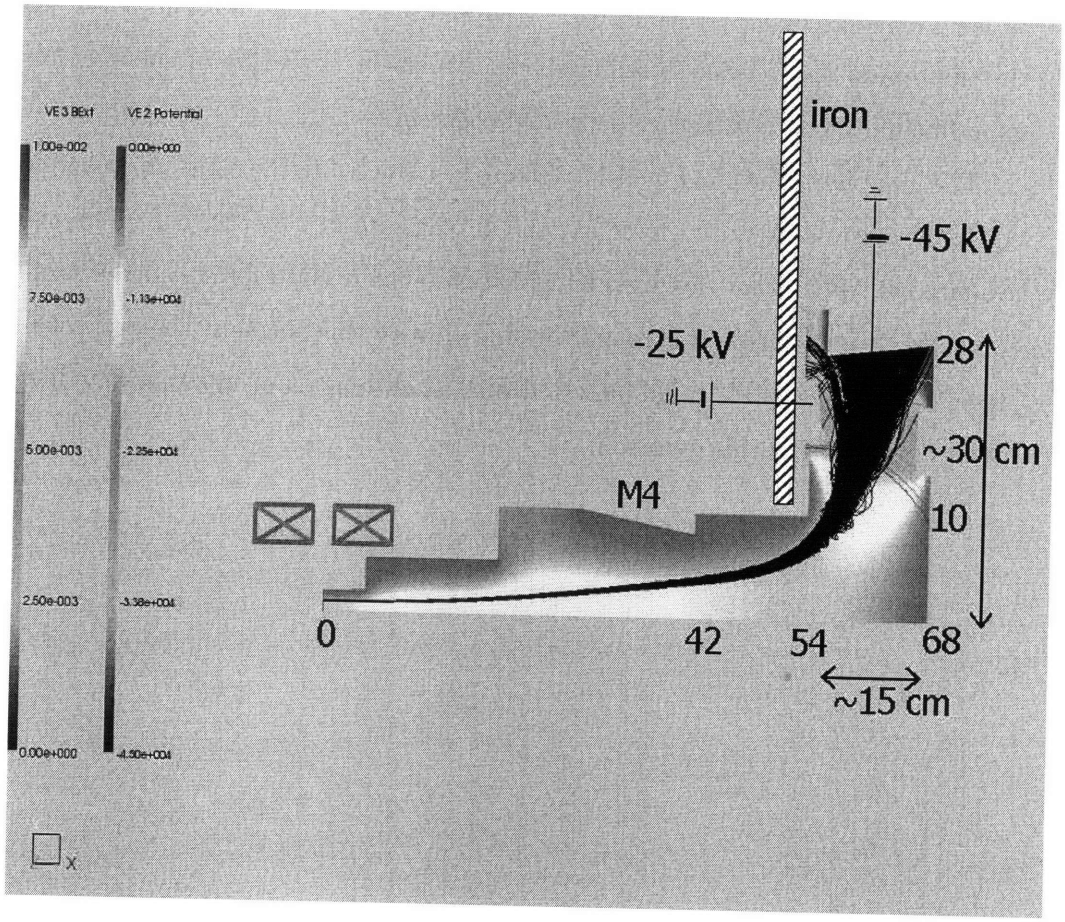

Figure 6-17: Simulation result from the MICHELLE code. Black lines are the trajectory of electron beams. The hatched square is the inserted iron piece. The first collector runs at 25 kV and the second collector is at 45 kV.

corresponding overall efficiency is 66 %.

From the result of the simulation, the overall efficiency from the two-stage depressed collector is promisingly enhanced. However the energy distribution of the spent beam after the interaction in the cavity strongly affects the overall efficiency of the two-stage depressed collector. Therefore an exact estimation of the energy distribution of spent beam is required. In conclusion, it will be of great interest to experimentally test a two-stage depressed collector.

The iron plate shown in Fig. 6-17 is strongly attracted to the main superconducting coil. There is a substantial force exerted on the superconducting coil. The magnet available at MIT is not designed to withstand such a large force and the proposed two-stage depressed collector cannot be studied with this magnet. The proposed two-stage depressed collector could be tested with a new magnet or in a specially designed industrial version of this gyrotron.

Chapter 7

Conclusion

The 1.5 MW, 110 GHz gyrotron experiments were successfully performed and reported in this thesis. The purpose for these studies was to enhance the overall efficiency of the gyrotron to over 50 %. A demountable experimental setup for a 1.5 MW, 110 GHz gyrotron at MIT enabled us to thoroughly study the gyrotron physics. There is a lack of experimental results in high power gyrotrons with a depressed collector, therefore the experimental results from the 1.5 MW, 110 GHz gyrotron at MIT will be of great interest for understanding the depressed collector performance.

The newly designed gyrotron cavity, V-2005, was tested in the axial configuration. The cavity was designed by MAGY, a gyrotron and gyro-klystron cavity design code developed by the University of Maryland and NRL. An output power of 1.67 MW was obtained and the corresponding efficiency was 42 % without a depressed collector. The previous cavity (V-2003), which is currently being used for CPI commercial gyrotrons, was re-tested in the same axial configuration. The difference between the V-2003 cavity and the V-2005 cavity is the output uptaper angle. The V-2005 cavity has a small uptaper angle of 0.7°, whereas the V-2003 cavity has an output taper angle of 1.2°. The Q factor for the V-2005 cavity therefore has decreased to 835, which is a fairly low Q, lower than the Q of 940 of the V-2003 cavity. The efficiency enhancement of the V-2005 cavity was a result of reduced mode competition between the $TE_{22,6}$ and $TE_{19,7}$ modes. From the start-up scenario analysis, the V-2005 cavity is much less susceptible to mode competition from the $TE_{19,7}$ mode than the V-2003

cavity. The mode map measurements of the cavities supported the start-up scenario analysis. The V-2005 cavity was solely excited in the $TE_{22,6}$ mode over a wide range of magnetic field whereas the V-2003 cavity has an overlapped region between the $TE_{22,6}$ mode and the $TE_{19,7}$ mode, indicating serious mode competition.

The internal mode converter was installed in the 1.5 MW, 110 GHz gyrotron. The internal mode converter consists of a launcher and 4 mirrors to transform the cavity mode, $TE_{22,6}$, into a Gaussian beam. The maximum output power was measured to be 1.5 MW with a good Gaussian profile measured by a motorized scanner. The power reduction in the internal mode converter configuration as compared to the axial configuration is due to the loss in the internal mode converter. The cold-test measurement of the internal mode converter efficiency by the University of Wisconsin was determined to be around 93 %, which is consistent with the measured 10 % reduction in output power. The mode map for the internal mode converter was generated in the experiment and a wide and stable excitation of the $TE_{22,6}$ mode was observed. The geometrical optics and quasi-optical approximations of the radiation from a helical cut launcher were analytically derived. The analytic solution was compared to the simulation results from Surf3D, which solves the electric field integral equation (EFIE). The phase and amplitude plots were generated at different cylindrical surfaces. The results between the analytic solutions and the numerical simulations match remarkably well. Internal mode converters have been designed in the past using the geometric optics approach, however, there was no theory that determined to what extent this approach can be used. The analytic theory that we have derived gives an insight to the geometrical optics theory and the quasi-optical approximation can represent rigorously high power gyrotron launchers (overmoded cavity gyrotrons). A new internal mode converter was designed along with a new, well-optimized launcher by J. Neilson at CCR. The new launcher and new mirror system are expected to reduce the power loss in the internal mode converter in future experiments.

A single-stage depressed collector was installed and tested successfully. A 50 % overall efficiency was measured at 1.5 MW output power with 25 kV collector depression voltage. The power was maintained to be constant up to the 25 kV collector

voltage, and it started to fall off when the body current began to appear. The depression voltage threshold, which was determined at the onset of body current, was measured as a function of beam current at a fixed beam voltage of 96 kV. The collector depression voltage threshold increased as the beam current decreased owing to the increased recoverable beam energy. The experimental results were compared to the numerical simulation results from MAGY by calculating the spent beam energy distribution. A substantial discrepancy between the experiment and the simulation was observed. The simulation predicted much higher threshold depression voltage than was allowable in the experiment. The discrepancy was explained by the aftercavity interaction (ACI), which has been theoretically studied recently. Usually after interacting with the electron beam inside the cavity, the wave becomes a traveling wave such that the interaction should no longer occur. However, a synchronous interaction between the spent beam and the traveling outgoing wave can occur if the radius of the after cavity region is small enough to meet the synchronism condition with the beam as the magnetic field falls off. For high power gyrotrons (highly overmoded cavities), the ACI can be serious because of the mild tapering of the radial geometry of the aftercavity region in order to prevent mode conversion. In our cavity and launcher geometry, the single-particle analytic solution predicts that there is an interaction between the spent beam and the wave at around 2-3 cm away from the launcher entrance. The numerical calculation from MAGY predicted almost exactly the same location as the analytic theory. More importantly, the additional synchronous resonance interaction makes the spent beam energy distribution wider. Therefore, the threshold depression voltage obtained at the end of the launcher is lower than at the end of the cavity. The spent beam energy distribution due to the ACI was obtained from a MAGY simulation and compared to the experimental data. The data was in excellent agreement, which indicates the ACI occurs in the gyrotron. This is the first experimental observation of the ACI in gyrotrons. We suggest two ways to avoid the ACI in the gyrotron. One way is increasing the magnetic flattop region towards the launcher. Unfortunately, the existing superconducting magnet has only 2.5 cm of flattop region, and in order to prevent the ACI the flattop region has to be greater

than 13 cm. The other way is to design the cavity and launcher such that the entrance radius of the launcher is increased to 2.3 cm. However, it is very challenging to design such a large radius launcher, and a new idea for shortening the launcher length may be required.

The design of a two-stage depressed collector was studied for the purpose of further efficiency enhancement. If an adiabatic decompression scheme is used, the collector size should be very large. In order to reduce the size of the collector, the non-adiabatic decompression could be employed. The insertion of a ferromagnetic iron piece at the collector region might be used for a reasonably sized two-stage depressed collector. The overall gyrotron efficiency calculated by utilizing the two-stage depressed collector is 66 % with a 70 % collector efficiency. To carry out such a research program would constitute a follow-up thesis.

Bibliography

[1] A. V. Gaponov, M. I. Petelin, and V. K. Yulpatov, "The induced radiation of excited classical oscillators and its use in high frequency electronics," *Radiophys. Quantum Electr.*, vol. 10, p. 794, 1967.

[2] J. L. Hirshfield and J. M. Wachtel, "Electron cyclotron maser," *Phys. Rev. Lett.*, vol. 12, pp. 533–536, 1964.

[3] J. L. Hirshfield, I. B. Bernstein, and J. M. Wachtel, "Cyclotron resonance interactions of microwaves with energetic electrons," *IEEE-QE*, vol. QE-1, pp. 237–245, 1965.

[4] V. A. Alikaev, V. A. Flyagin, V. I. Khizhnyak, A. G. Luchinin, G. S. Nusinovich, V. G. Usov, and S. N. Vlasov, "Gyrotrons for electron-cyclotron plasma heating in large tokamaks.," *Proc. Symp.: First Symposium on Heating in Toroidal Plasmas, Grenoble, France*, vol. 2, pp. 339–349, 1979.

[5] M. Thumm, X. Yang, G. Dammertz, G. Michel, J. Pretterebner, and D. Wagner, "A high-efficiency quasi-optical mode converter for a 140 GHz 1 MW CW gyrotron," *IEEE Trans. Electron Devices*, vol. 52, no. 5, pp. 818–824, 2005.

[6] R. Prater, "Heating and current drive by electron cyclotron waves," *Phys. Plasmas*, vol. 11, pp. 2349–2376, 2004.

[7] N. Hayashi, T. Ozeki, K. Hamamatsu, and T. Takizuka, "ECCD power necessary for the neoclassical tearing modes stabilization in ITER," *Nucl. Fusion*, vol. 44, pp. 477–487, 2004.

[8] R. W. Callis, W. P. Cary, S. Chu, J. L. Doane, R. A. Ellis, K. Felch, Y. A. Golerov, H. J. Grunloh, J. Hosea, K. Kajiwara, J. Lohr, T. C. Luce, J. J. Peavy, R. I. Pinsker, D. Ponce, R. Prater, M. Shapiro, R. J. Temkin, and J. F. Tooker, "Maturing ECRF technology for plasma control," *Nucl. Fusion*, vol. 43, pp. 1501–1504, 2003.

[9] C. C. Petty, R. J. LaHaye, T. C. Luce, D. A. Humphreys, A. W. Hyatt, J. Lohr, R. Prater, E. J. Strait, and M. R. Wade, "Heating and current drive by electron cyclotron waves," *Nucl. Fusion*, vol. 44, pp. 243–251, 2004.

[10] K. Felch, M. Blank, P. Borchard, P. Cahalan, S. Cauffman, K. Felch, and H. Jory *Proc. 3rd IEEE Int. Vacuum Electronics Conf., Piscataway, NJ.*, p. 332, 2002.

[11] B. Piosczyk, A. Arnold, G. Dammertz, R. Heidinger, S. Illy, J. Jin, K. Koppenburg, W. Leonhardt, G. Neffe, T. Rzesnicki, M. Schmid, M. Thumm, X. Yang, S. Alberti, R. Chavan, D. Fasel, T. Goodman, M. Henderson, J. P. Hogge, M. Q. Tran, I. Yovchev, V. Erckmann, H. P. Laqua, G. Michel, G. Gantenbein, W. Kasparek, G. Müller, K. Schwörer, D. Bariou, A. Beunas, E. Giguet, G. LeCloarec, F. Legrand, C. Liévin, and O. Dumbrajs *ITER IAEA Fusion Energy Conference, Vilamoura, Portugal*, 2004.

[12] K. Felch, Communications and Power Industries, California, and U.S.A. *private communication*, 2004.

[13] *4th IAEA Technical Meeting on ECRH Physics and Technology for ITER, Vienna*, 2007.

[14] R. Q. Twiss, "Radiation transfer and the possibility of negative absorption in radio astronomy," *Australian Journal of Physics*, vol. 11, pp. 564–579, 1958.

[15] J. Schneider, "Stimulated emission of radiation by relativistic electrons in a magnetic field," *Phys. Rev. Lett.*, vol. 2, pp. 504–505, 1959.

[16] A. V. Gaponov, "Interaction of irrectilinear electron beams with electromagnetic waves in transmission lines," *Izv. VUZov Radiofizika*, vol. 2, pp. 450–462, 1959.

[17] V. A. Flyagin, A. V. Gaponov, M. I. Petelin, and V. K. Yulpatov, "The gyrotron," *IEEE Trans. Microwave Theory and Tech.*, vol. 25, pp. 514–521, 1977.

[18] B. G. Danly and R. J. Temkin, "Generalized nonlinear harmonic gyrotron theory," *Phys. Fluids*, vol. 29, pp. 561–567, 1986.

[19] A. W. Fliflet, M. E. Read, K. R. Chu, and R. Seeley, "A self-consistent field theory for gyrotron oscillators: application to a low Q gyromonotron," *Int. J. Electron.*, vol. 53, pp. 505–521, 1982.

[20] G. S. Nusinovich, "Review of the theory of mode interaction in gyrodevices," *IEEE Trans. Plasma Sci.*, vol. 27, pp. 313–326, 1999.

[21] G. S. Nusinovich, *Introduction to the Physics of Gyrotrons.* The Johns Hopkins University Press, Baltimore, 2004.

[22] A. W. Fliflet, R. C. Lee, S. H. Gold, W. M. Manheimer, and E. Ott, "Time-dependent multimode simulation of gyrotron oscillator," *Phys. Rev. A*, vol. 43, pp. 6166–6176, 1991.

[23] D. R. Whaley, M. Q. Tran, S. Alberti, T. M. Tran, T. M. Antonsen, and C. Tran, "Startup methods for single-mode gyrotron operation," *Phys. Rev. Lett.*, vol. 75, p. 1304, 1995.

[24] W. C. Guss, M. A. Basten, K. E. Kreischer, R. J. Temkin, T. M. Antonsen, S. Y. Cai, G. Saraph, and B. Levush, "Sideband mode competition in a gyrotron oscillator," *Phys. Rev. Lett.*, vol. 69, pp. 3727–3730, 1992.

[25] M. Botton, T. M. Antonsen Jr., B. Levush, A. Vlasov, and K. Nguyen, "MAGY: A time dependent code for simulation of electron beam devices," *IEEE Trans. Plasma Sci.*, vol. 26, pp. 882–892, 1998.

[26] G. S. Nusinovich, M. Yeddulla, T. M. Antonsen, and A. N. Vlasov, "Start-up scenario in gyrotrons with a nonstationary microwave-field structure," *Phys. Rev. Lett.*, vol. 96, p. 125101, 2006.

[27] K. T. Nguyen, B. Levush, T. M. Antonsen, M. Botton, M. Blank, J. P. Calame, and B. G. Danly, "Modeling of gyroklystrons with MAGY," *IEEE Trans. Plasma Sci.*, vol. 28, pp. 867–886, 2000.

[28] A. N. Vlasov, T. M. Antonsen, D. P. Chermin, B. Levush, and E. L. Wright, "Simulation of microwave devices with external cavities using MAGY," *IEEE Trans. Plasma Sci.*, vol. 30, pp. 1277–1291, 2002.

[29] M. Blank, B. G. James, P. Borchard, P. Cahalan, T. S. Chu, H. Jory, B. G. Danly, B. Levush, J. P. Calame, K. T. Nguyen, and D. E. Pershing, "Development and demonstration of high-average power W-Band gyro-amplifiers for radar applications," *IEEE Trans. Plasma Sci.*, vol. 30, pp. 865–875, 2002.

[30] A. T. Drobot and K. Kim, "Space-charge effects on the equilibrium of guided electron flow with gyromonotron," *Int. J. Electron.*, vol. 51, p. 351, 1981.

[31] A. K. Ganguly and K. R. Chu, "Limiting current in gyrotron," *Int. J. Infrared Millimeter Waves*, vol. 5, p. 103, 1984.

[32] W. B. Hermannsfeldt, "EGUN." SLAC-226, November, 1979.

[33] C. R. K. Marrian and A. Shih, "The operation of coated tungsten-based dispenser cathodes in nonideal vacuum," *IEEE Trans. Electron Devices*, vol. 36, pp. 173–179, 1989.

[34] J. P. Anderson, *Experimental Study of a 1.5-MW, 110-GHz Gyrotron Oscillator.* PhD thesis, Massachusetts Institute of Technology, Elec. Engrg. and Comp. Sci. Dept., 2005.

[35] K. E. Kreischer, J. B. Schutkeker, B. G. Danly, W. J. Mulligan, and R. J. Temkin, "High efficiency operation of a 140 GHz pulsed gyrotron," *Int. J. Electron.*, vol. 57, pp. 835–850, 1984.

[36] W. C. Guss, T. L. Grimm, K. E. Kreischer, J. T. Polevoy, and R. J. Temkin, "Velocity ratio measurements of a gyrotron electron beam," *J. Appl. Phys.*, vol. 69, p. 3789, 1991.

[37] K. Felch, M. Blank, P. Borchard, T. S. Chu, J. Feinstein, H. R. Jory, J. A. Lorbeck, C. M. Loring, Y. M. Mizuhara, J. M. Neilson, R. Schumacher, and R. J. Temkin, "Long-pulse and CW tests of a 110 GHz gyrotron with an internal, quasi-optical converter," *IEEE Trans. Plasma Sci.*, vol. 24, p. 558, 1996.

[38] J. P. Anderson, M. A. Shapiro, R. J. Temkin, I. Mastovsky, and S. R. Cauffman, "Studies of the 1.5 MW 110 GHz gyrotron experiment," *IEEE Trans. Plasma Sci.*, vol. 32, p. 877, 2004.

[39] E. M. Choi, C. D. Marchewka, M. A. Shapiro, J. R. Sirigiri, I. Mastovsky, and R. J. Temkin, "Experimental results for a 1.5 MW, 110 GHz gyrotron oscillator with reduced mode competition," *Phys. Plasmas, 023103*, vol. 13, 2006.

[40] CASCADE. Cascade engine V1.60, Calabazas Creek Research, Inc., Saratoga, CA, 2001.

[41] G. S. Nusinovich, O. V. Sinitsyn, L. Velikovich, M. Yeddulla, T. M. Antonsen, A. N. Vlasov, S. R. Cauffman, and K. Felch, "Startup scenarios in high-power gyrotrons," *IEEE Trans. Plasma Sci.*, vol. 32, p. 841, 2004.

[42] M. Yeddulla, G. S. Nusinovich, and T. M. Antonsen, "Start current in an over-moded gyrotron," *Phys. Plasmas*, vol. 10, p. 4513, 2003.

[43] M. Thumm, X. Yang, A. Arnold, G. Dammertz, G. Michel, J. Pretterebner, and D. Wagner, "A high-efficiency quasi-optical mode converter for a 140 GHz 1 MW CW gyrotron," *IEEE Trans. Electron Devices*, vol. 52, no. 6, pp. 818–824, 2005.

[44] M. V. Kartikeyan, E. Borie, and M. K. A. Thumm, *Gyrotrons.* New York: Springer, 2004.

[45] S. N. Vlasov, L. I. Zagryadskaya, and M. I. Petelin, "Transformation of a whispering gallery mode, propagating in a circular waveguide, into a beam of waves," *Radio Eng. Electron. Phys.*, vol. 20, pp. 14–17, 1975.

[46] J. A. Lorbeck and R. J. Vernon, "Singly curved dual-reflector synthesis technique applied to a quasi-optical antenna for a gyrotron with a whispering-gallery mode output," *IEEE Trans. Antennas Propag.*, vol. 39, pp. 1733–1741, 1991.

[47] S. N. Vlasov and M. A. Shapiro, "Bievolvent mirror for transfer of caustic surfaces," *Sov. Tech. Phys. Lett.*, vol. 15, p. 374, 1989.

[48] S. N. Vlasov, M. A. Shapiro, and E. V. Sheinina, "Wave beam shaping on diffraction of a whispering gallery wave at a convex cylindrical surface," *Radiophys. Quantum Electr.*, vol. 31, p. 1070, 1988.

[49] G. G. Denisov, A. N. Kuftin, V. I. Malygin, N. P. Venediktov, D. V. Vinogradov, and V. E. Zapevalov, "110 GHz gyrotron with built-in high efficiency converter," *Int. J. Electron.*, vol. 72, p. 1079, 1992.

[50] M. Iima, M. Sato, Y. Amano, S. Kobayashi, M. Nakajima, M. Hashimoto, O. Wada, K. Sakamoto, M. Shiho, T. Nagashima, M. Thumm, A. Jacobs, and W. Kasparek, "Measurement of radiation field from an improved efficiency quasi-optical converter for whispering-gallery mode," *Conf. Digest, 14th Int. Conf. on Infrared and Millim. Waves, Wurzburg, Proc. SPIE 1240*, p. 405, 1989.

[51] M. K. Thumm and W. Kasparek, "Passive high-power microwave components," *IEEE Trans. Plasma Sci.*, vol. 30, pp. 755–786, 2002.

[52] J. M. Neilson and R. Bunger, "Surface integral equation analysis of quasi-optical launcher," *IEEE Trans. Plasma Sci.*, vol. 30, p. 794, 2002.

[53] M. K. Hornstein, V. S. Bajaj, R. G. Griffin, K. E. Kreischer, I. Mastovsky, M. A. Shapiro, J. R. Sirigiri, and R. J. Temkin, "Second harmonic operation at 460 GHz and broadband continuous frequency tuning of a gyrotron oscillator," *IEEE Trans. Electron Devices*, vol. 52, pp. 798–807, 2005.

[54] T. Idehara, I. Ogawa, S. Mitsudo, M. Pereyaslavets, N. Nishida, and K. Yoshida, "Development of frequency tunable medium power gyrotrons (gyrotron FU se-

ries) as submillimeter wave radiation sources," *IEEE Trans. Plasma Sci.*, vol. 27, pp. 340–354, 1999.

[55] H. Shirai and L. B. Felsen, "Rays and modes for plane wave coupling into a large open-ended circular waveguide," *Wave Motion*, vol. 9, pp. 461–482, 1987.

[56] K. Goto, T. Ishihara, and L. B. Felsen, "High-frequency whispering-gallery mode to beam conversions on a perfectly conducting concave-convex boundary," *IEEE Trans. Antennas Propag.*, vol. 50, pp. 1109–1119, 2002.

[57] V. M. Babich and V. S. Buldyrev, "Short-wavelength diffraction theory: Asymtotic methods," *Springer-Verlag*, 1991.

[58] S. Solimeno, B. Crosignani, and P.Di Porto, *Guiding, Diffraction, and Confinement of Optical Radiation.* Orlando, Florida: Academic Press, 1986.

[59] M. Blank, *High Efficienecy Quasi-Optical Mode Converters for Overmoded Gyrotrons.* PhD thesis, Massachusetts Institute of Technology, Elec. Engrg. and Comp. Sci. Dept., 1994.

[60] D. R. Denison, *Gyrotron Mode Converter Mirror Shaping Based on Phase Retrieval from Intensity Measurements.* PhD thesis, Massachusetts Institute of Technology, Elec. Engrg. and Comp. Sci. Dept., 1999.

[61] G. G. Denisov, A. N. Kuftin, V. I. Malygin, N. P. Venedikov, D. V. Vinogradov, and V. E. Zapevalov, "110 GHz gyrotron with built-in high efficiency converter," *Int. J. Electron.*, vol. 72, no. 5, pp. 1079–1091, 1992.

[62] P. F. Goldsmith, *Quasioptical Systems: Gaussian Beam Quasioptical Propagation and Applications.* Wiley Publisher, 1998.

[63] D. H. Martin and J. W. Bowen, "Long-wave optics," *IEEE Trans. Microwave Theoery Tech.*, vol. MTT-41, pp. 1676–1690, 1993.

[64] J. M. Neilson, "Optimal synthesis of quasi-optical launchers for high-power gyrotrons," *IEEE Trans. Plasma Sci.*, vol. 34, no. 3, pp. 635–641, 2006.

[65] J. A. Kong, *Electromagnetic Wave Theory.* New York: John Wiley and Sons, Inc., 1986.

[66] LOT Launcher Optimization Tool. Version 1.21, Calabazas Creek Research, Inc., Saratoga, CA, 2005.

[67] K. Felch, M. Blank, P. Borchard, T. S. Chu, J. Feinstein, H. R. Jory, J. A. Lorbeck, C. M. Loring, Y. M. Mizuhara, J. M. Neilson, R. Schumacher, and R. J. Temkin, "Long-pulse and CW tests of a 110 GHz gryotron with an internal, quasioptical mode converter," *IEEE Trans. Plasma Sci.*, vol. 24, pp. 558–569, 1996.

[68] P. M. Borchard, *Design of a data acquisitioning system for near and far field scans of the gyrotron.* Massachusetts Institute of Technology: Barchelor's project, 1993.

[69] R. Cao, M. P. Perkins, and R. Vernon, "Design of a high efficiency launcher and mirror system for use in a 110 GHz $TE_{22,6}$ mode gyrotron," *Infrared and Millimeter Waves 2004 and 12th International Conference on Terahertz Electronics 2004, IRMMW-THz 2004*, pp. 487–488, 2004.

[70] K. Sakamoto, M. Tsuneoka, A. Kasugai, T. Imai, T. Kariya, K. Hayashi, and Y. Mitsunaka, "Major improvement of gyrotron efficiency with beam energy recovery," *Phys. Rev. Lett.*, vol. 73, p. 3532, 1994.

[71] V. E. Zapevalov and M. A. Moiseev, "Influence of aftercavity interaction on gyrotron efficiency," *Radiophys. Quantum Electr.*, vol. 47, no. 7, pp. 520–527, 2004.

[72] N. A. Zavolsky, V. E. Zapevalov, and M. A. Moiseev, "Influence of the energy and velocity spread in the electron beam on the starting conditions and efficiency of a gyrotron," *Radiophys. Quantum Electr.*, vol. 49, no. 2, pp. 108–119, 2006.

[73] H. G. Kosmahl, "Modern multistage depressed collectors - A review," *Proceedings of IEEE*, vol. 70, no. 11, pp. 1325–1334, 1982.

[74] G. Ling, B. Piosczyk, and M. K. Thumm, "A new approach for a multistage depressed collector for gyrotrons," *IEEE Trans. Plasma Sci.*, vol. 28, no. 3, pp. 606–613, 2000.

[75] A. Singh, S. Rajapatirana, Y. Men, V. L. Granatstein, R. L. Ives, and A. J. Antolak, "Design of a multistage depressed collector system for 1-MW CW gyrotrons-part I: Trajectory control of primary and secondary electrons in a two-stage depressed collector," *IEEE Trans. Plasma Sci.*, vol. 27, no. 2, pp. 490–502, 1999.

[76] A. Singh, A. Valfells, M. J. Kolander, and V. L. Granatstein, "Improvements in depressed collector performance by modifications to electrode geometry vis-a-vis trajectories of backscattered electrons," *IEEE Trans. Plasma Sci.*, vol. 32, no. 3, pp. 1267–1276, 2004.